Copyright Warning & Restrictions

The copyright law of the United States (Title 17, United States Code) governs the making of photocopies or other reproductions of copyrighted material.

Under certain conditions specified in the law, libraries and archives are authorized to furnish a photocopy or other reproduction. One of these specified conditions is that the photocopy or reproduction is not to be "used for any purpose other than private study, scholarship, or research." If a, user makes a request for, or later uses, a photocopy or reproduction for purposes in excess of "fair use" that user may be liable for copyright infringement,

This institution reserves the right to refuse to accept a copying order if, in its judgment, fulfillment of the order would involve violation of copyright law.

Please Note: The author retains the copyright while the New Jersey Institute of Technology reserves the right to distribute this thesis or dissertation

Printing note: If you do not wish to print this page, then select "Pages from: first page # to: last page #" on the print dialog screen

NJIT
New Jersey's Science &
Technology University

The Van Houten library has removed some of the personal information and all signatures from the approval page and biographical sketches of theses and dissertations in order to protect the identity of NJIT graduates and faculty.

ABSTRACT

HOLLOW CATHODE SPUTTERING SYSTEM
– INSTALLATION, OPERATION AND THEORETICAL BACKGROUND –

by
Sebastian Falk

The objective of this work was to assemble, install and operate a hollow cathode sputtering system (HCSS). Therefore a complex vacuum system was built to create the right sputtering environment. The purpose of the HCSS is to develop advanced thin conducting oxides (TCOs) as well as high resistivity transparent (HRT) layers which are used for thin film photovoltaic technology, particularly cadmium telluride based and copper indium gallium selenide based solar cells.

A theoretical background of the thin film technology and a comparison of different deposition methods in regards to the sputtering process is provided. Thereby, an in-depth investigation of zinc oxide (ZnO), tin oxide (SnO_2), and cadmium stannate (Cd_2SnO_4) is presented. Furthermore, the operating characteristics of a hollow cathode are described. A detailed analysis of the different system components, as well as their functions, is thoroughly elucidated. Moreover, important system parameters required for the correct operation of the HCSS are identified.

HOLLOW CATHODE SPUTTERING SYSTEM
– INSTALLATION, OPERATION AND THEORETICAL BACKGROUND –

by
Sebastian Falk

A Thesis
Submitted to the Faculty of
New Jersey Institute of Technology
in Partial Fulfillment of the Requirements for the Degree of
Master of Science in Electrical Engineering.

Department of Electrical and Computer Engineering

May 2015

Copyright © 2015 by Sebastian Falk

ALL RIGHTS RESERVED

.

APPROVAL PAGE

Hollow Cathode Sputtering System
– Installation, Operation and Theoretical Background –

Sebastian Falk

Dr. Mengchu Zhou, Academic Advisor Date
Distinguished Professor of Electrical and Computer Engineering, NJIT

Dr. Alan E. Delahoy, Thesis Advisor Date
Research Professor of Phyics, NJIT

Dr. Marek Sosnowski, Committee Member Date
Professor of Electrical and Computer Engineering, NJIT

Dr. Ken Chin, Committee Member Date
Professor of Physics, NJIT

Dr. Durgamadhab Misra, Committee Member Date
Professor of Electrical and Computer Engineering, NJIT

BIOGRAPHICAL SKETCH

Author: Sebastian Falk

Degree: Master of Science

Date: May 2015

Undergraduate and Graduate Education:

- Master of Science in Electrical Engineering,
  New Jersey Institute of Technology, Newark, New Jersey, USA, 2015

- Bachelor of Science in Electrical Engineering,
  Beuth University of Applied Science, Berlin, Germany, 2013

Major: Electrical Engineering

Program: Power and Energy Systems

This work is dedicated to my parents, who always supported me in every way and constantly encouraged me to never stop exploring.

ACKNOWLEDGMENT

First, I thank my thesis advisor Professor Alan Delahoy for his support and expert guidance throughout the last two semesters. He gave me the unique opportunity to work on cutting edge technology at the CNBM New Energy Materials Research Center at NJIT.

Further, I thank Professor Mengchu Zhou for his academic guidance.

Besides Professor Delahoy, Professor Ken Chin played an important role during my work in the CNMB research center. I thank him for very helpful and inspiring talks about a wide range of topics regarding solar cell physics during the weekly lab meetings.

In addition, I express my gratitude to Professor Marek Sosnowski for his help with practical challenges with the vacuum system and the advices on what I should focus in my thesis.

I also thank Professor Durgamadhab Misra for his technical and scientific guidance and support.

A very special thanks is for Dr. Zhimeng Cheng and Ben Porter who both helped me very much during the assembly process of the Hollow Cathode Sputtering System. Without them it would have been impossible at some point.

TABLE OF CONTENTS

Chapter	Page
1 INTRODUCTION…….....……..…….	1
2 DEPOSITION METHODS …….……...	5
2.1 Chemical Vapor Deposition ……....	5
2.2 Physical Vapor Deposition ……..…	8
2.2.1 Evaporation ……...……	8
2.2.2 Sputtering ……..	10
2.3 Comparison of Deposition Methods ……..	12
3 HOLLOW CATHODE SPUTTERING ……	14
3.1 The Physical Nature of Sputtering ……..……...…	14
3.1.1 Interactions of Ions with Surfaces …….	14
3.1.2 Sputter Target Kinetics …….	16
3.1.3 Thin Film Formation …….	19
3.2 DC Sputtering ……...……...	24
3.2.1 The General DC Sputter Process ……..	24
3.2.2 DC Glow Discharge ……..	28
3.2.3 Practical Aspects of Sputtering Systems ……...	31
3.3 Hollow Cathode Sputtering …….	34
4 THIN CONDUCTING OXIDES ……...	38
4.1 Transparent Conductors……...…	38
4.2 Transparent Conducting Oxides for Photovoltaics ..…….…..	40

TABLE OF CONTENTS
(Continued)

Chapter	Page
4.3 Classification and Important Types …….	41
4.3.1 Zinc Oxide …….…….……..……	44
4.3.2 Tin Oxide ……...……..……..…....	50
4.2.3 Cadmium Stannate …….……...……..….....	55
5 HOLLOW CATHODE SPUTTERING SYSTEM …...……..….....	60
5.1 System Overview ……..…..	60
5.2 The Vacuum Chamber ..……..	65
5.2.1 Outer Connections ……...…….…….	65
5.2.2 Inner Setup …….…….…….	67
5.3 GXS Vacuum Line ……..……	69
5.3.1 The Main Pump System ...……...……..	70
5.3.2 Control Gate Valve ……...……	76
5.3.3 Operation Sequence of the GXS Vacuum Line ……	78
5.4 The nEXT Vacuun Line ……..	80
5.4.1 Turbomolecular Pump ……...	80
5.4.2 Backing Line …….	86
5.4.3 Vacuum Gate Valve …….....	89
5.4.4 Operation Sequence of the nEXT Line …….	90
5.5 The Load Lock Vacuum Line …….	92
5.5.1 Load Lock …….	92

TABLE OF CONTENTS
(Continued)

Chapter **Page**

5.5.2 Linear Rack and Pinion ……. 93

5.5.4 Operation Sequence of the Load Lock Line ……. 98

5.6 The Sputtering Power Supply ……...……... 99

5.7 Venting System ……... 103

5.8 Gas Flow Control Panel …….. 105

5.8.1 Control Panel …… 105

5.8.2 Gas Supply …… 106

5.8.3 Operation …….. 107

5.9 Temperature Monitor Interface ……... 111

6 EXPERIMENTAL DATA ……. 113

6.1 Initial Start of the Pump System ……. 113

6.2 Leak Characteristics …… 115

6.2 Gas Flow Experiments ……..…….. 118

7 CONCLUSION …….. 122

APPENDIX A ADDITIONAL OPERATION INFORMATION …….. 124

A.1 DPi8 Configuration Flow Chart …..……...… 124

A.2 PM5 Configuration …….....…….….. 125

A.3 PID menu structure ……. 126

A.4 Manu structure of TIC …… 127

A.5 Main menus of RPDG …… 128

TABLE OF CONTENTS
(Continued)

Chapter **Page**

A.6 CG User Interface Map …….. 129

APPENDIX B PROPERTIES OF TRANSPARENT CONDUCTING OXIDES …..... 130

B.1 List of important properties of typical TCOs ..……...… 130

APPENDIX C PRESSURE CONVERSION TABLES ……. 131

C.1 Pressure Conversion Table ……. 131

C.2 Leak Rate Conversion Table …….. 131

REFERENCES ……... 132

LIST OF TABLES

Table		Page
2.1	Different Sputter Configurations …..……..…….	11
2.2	Comparison of Various Deposition Methods ……	13
3.1	Sputter Yield for Ar and Ar Threshold for Various Metals …..…….	18
3.2	Typical cathode dimensions and operating parameters …….	36
4.1	Examples for Binary, Ternary, and Quaternary TCOs …….	42
4.2	TCOs Typically Used in PV Applications ....…….……...	43
4.3	Sputtering Parameters Utilizing a Zinc Target …….…	48
4.4	Comparison of Sputter Techniques for Deposition of ZnO:Al Thin Films .....…..	49
4.5	Doped ZnO Samples Deposited by HCS and by RF Magnetron Sputtering …….	50
4.6	Process Parameters for Depositing Sb:SnO_2 ……...……..	52
4.7	Process Parameters for Sputtering of Tin Targets ……...…….	53
5.1	Gate Valves Used in the HCSS ……..	60
5.2	HCSS Components and their Function ……..	61
5.3	Orifices on the Vacuum Chamber and their Use ……...	66
5.4	Performance Characteristics of the GXS Dry Pump System …….	71
5.5	Menu Structure of the PID …….	76
5.6	Reading and Control Pressure for the CM …….	77
5.7	CVGC Setpoints and Corresponding Valve Positions ……...	78
5.8	Performance Parameter of the nEXT 300D ……...	81
5.9	TIC Setup Options …….	84

LIST OF TABLES
(Continued)

Table **Page**

5.10 Positions of the Gas Ballast Control Valve …… 88

5.11 SmarMotor Status LEDs and their Meaning …….. 95

5.12 SmartMotor Parameters, their Ranges and Conversion ……. 97

5.13 RPDG Front Panel Buttons and their Function ……. 102

5.14 Full Scale Flow Rates of the MFCs ……... 108

5.15 Commands of VOR …… 108

6.1 Ultimate Pressure and Evacuation Times of the Vacuum Pumps …….. 113

6.2 Quantitative Characterization of a High Vacuum …….. 116

6.3 Lower and Upper Pressure Limits for Different Ar Flow Rates …… 120

6.4 Lower and Upper Flow Rate Limits for Different Pressures ……. 121

B.1 List of Important Properties of Typical TCOs ……... 130

C.1 Pressure Conversion Table …… 131

C.2 Leak Rate Conversion Table …….. 131

LIST OF FIGURES

Figure		Page
1.1	Evolution of Global PV Cumulative Installed capacity 2000 to 2013 …..……...	3
1.2	Research Cell Efficiencies …….	4
2.1	Typical CVD System ..……...…...……..……..	7
2.2	Schematic Chart of the Thermal Evaporation Process ….....……	8
2.3	Schematic chart of electron beam evaporation ……..	9
2.4	Schematic Diagram of a Reactive Magnetron Sputtering System ……..……...	12
3.1	Interactions of Ions with Surfaces ……..	15
3.2	The Variation of Sputter Yield as a Function of Ion Energy, for Ar on Cu ……..	17
3.3	Sputter Yield Depending on the Ion Energy for Different Inert Gases …….	19
3.4	Steps of Thin Film Growth ……..……...……...	20
3.5	The Three Modes of Thin Film Growth ……...……	22
3.6	Effects of Energetic Bombardment on a Growing Thin Film ……	23
3.7	Qualitative Plot of the Sputter Rate Against the Partial Pressure of the Reactive Gas …….	23
3.8	Typical Hysteresis Form of the Oxygen Partial Pressure against the Oxygen Flow Rate of the Sputter Process ……...	24
3.9	Basic Structure of a DC Sputtering System ……...	25
3.10	Typical I-V Curves at Different Argon Pressures (in Torr) ….……..	26
3.11	V-I Curve at Different Argon Pressures ……	27
3.12	Sputter Yield Depending on the Pressure of Ar for a Ni Target ……	27
3.13	Qualitative Characteristics of a DC Glow Discharge ……	29

LIST OF FIGURES
(Continued)

Figure **Page**

3.14 I-V Curve of a Typical Low Pressure Glow Discharge ……. 30

3.15 Distribution of the Potential in a DC Glow Discharge …….. 31

3.16 Schematic of a Sputtering System ……. 32

3.17 Some Possible Ground Shield Arrangements …… 33

3.18 Penetration of Plasma into the Cathode Cavity (left), a Gas Flow Cylindrical Hollow Cathode (right) …….. 35

3.19 Schematic of the Interior of a Vacuum Chamber for HCS …… 37

3.20 Basic Hollow Cathode Design for Linear Sputtering Source …… 37

4.1 Principle Types of Solar Cells that Utilize TCOs …….. 41

4.2 Wurtzite Crystal Structure of ZnO ……. 44

4.3 Calculated Band Structure of ZnO ……. 45

4.4 Effect of Oxygen Concentration and Substrate Temperature on Conductivity and Transparency of ZnO Films……. 46

4.5 Growth Rate ZnO Depending of Substrate Temperature and Oxygen Concentration ……..……... 49

4.6 Crystal Structure of Tin Oxide ……... 50

4.7 Band Structure Calculation for SnO2 (left), and Sb Doped SnO2 (right) ……. 51

4.8 Phase Content of SnO_x Films Versus Oxygen Concentration ……... 53

4.9 Resistivity, Carrier Concentration, and Carrier Mobility of SnO2 Thin Films as a Function of Oxygen Pressure …….. 54

4.10 V-I Characteristic for Sputtering of SnO2 ……. 54

4.11 Cubic Spinel Structure of Cd2SnO4 …….. 56

LIST OF FIGURES
(Continued)

Figure **Page**

4.12 Sputtering Rate and Resistivity as a Function of the Ar O_2 Mixture ……..... 58

4.13 The Deposition Rate of CTO and ITO as a Function of Substrate Temperature ... 58

5.1 Piping Diagram of the HCSS ……. 62

5.2 Photographs of the HCSS …….. 63

5.3 Vacuum Flange Systems Used in the HCSS ……. 65

5.4 Schematic Front View of the Interior Components ……... 67

5.5 Water Flow Control Panel for Cathode and Heat Shield ……... 68

5.6 3D Sketch of the Cathode and Substrate Arrangement ……. 69

5.7 Photograph of the GXS Line ……. 70

5.8 Performance Curve of the GXS ……. 71

5.9 GXS Water Flow Control Panel …… 72

5.10 GXS Back View ……. 73

5.11 Pump Terminal Display (PDT) …….. 74

5.12 GXS Front Panel Controls ……. 75

5.13 CGV Controller …….. 77

5.14 nEXT Vacuum Line ……... 80

5.15 nEXT Performance Curve …….. 81

5.16 Controller Status Information …… 82

5.17 TIC Front View …….. 83

5.18 TIC Back View …….. 83

LIST OF FIGURES
(Continued)

Figure	Page
5.19 XDS 10 Dry Pump …….	87
5.20 Performance Characteristic of the XDS 10 ……	88
5.21 Convection Gauge ……..	89
5.22 TPGV Control Panel ……..	89
5.23 Load Lock Vacuum Line ……...	92
5.24 Load Lock Used for the HCSS ……..	93
5.25 LRP Setup ……..	94
5.26 SmartMotor Cable Assembly …….	94
5.26 RPDG Connection Diagram ……..	92
5.27 LRP Software SMI …….	96
5.28 SMI SmartMotor Playground ……	97
5.29 RPDG Connection Diagram ……..	100
5.30 Detailed Cable Assembly for the DC Output of the RPDG ……..	100
5.31 RPDG Front View (Control Panel) ……	101
5.32 Display of the RPDG: (a) Pulse Mode On, (b) Pulse Mode Off ……	101
5.33 Venting Control Panel ……	104
5.34 Gas Flow Control Panel …….	105
5.35 Gas Regulator and Flexible Hose (Attached to the Gas Cylinder) ……	106
5.36 Operating Principle of the MFC GF40 ……..	107
5.37 Gas Flow Control Operating System …….	109

LIST OF FIGURES
(Continued)

Figure **Page**

5.38 View at the Software Brooks SMART Interface ……... 110

5.39 Interface of the Brooks MultiFlo Configurator Software …….. 111

5.40 Temperature Monitor Interface …….. 112

6.1 Evacuation Curve of the GXS and nEXT …….. 114

6.2 Chamber Leak Characteristic ……. 115

6.3 Load Lock Leak Characteristic …….. 116

6.4 Chamber Pressure Increase when Inserting Nitrogen …… 117

6.5 Chamber Pressure Depending on the Ar Flow Rate With CGC Fully Open ……. 119

6.6 Chamber Pressure (CM) Depending on the Ar Flow Rate for Different CGV Positions ……... 119

A.1 DPi8 Configuration Flow Chart ……. 124

A.2 PM5 Configuration (Setup Sequence) ……... 125

A.3 PTD Menu Structure …….. 126

A.4 Menu Structure of the TIC ……. 127

A.5 Main Menus of the RPDG …… 128

A.6 CG User Interface Map …….. 129

CHAPTER 1

INTRODUCTION

In times of scarcity of resources and climatic change, renewable energies gain an eminent importance in ensuring a future reliable and sustainable energy supply. Thereby, photovoltaic (PV) systems play a prominent role. The Figure 1.1 pinpoints the fact that solar energy systems are not only implemented the energy grids world-wide, moreover, the installed PV power is growing constantly.

The vast majority of todays installed PV systems are based on crystalline silicon solar cells. Since silicon is the second most abundant element on the earth, alternative solar cell structures are produced and implemented in a PV system. The most competing solar cell types for silicon based solar cells are founded on thin film technology. Among them are cadmium telluride (CdTe) and copper-indium-gallium-selenide (CIGS) based solar cells. The chart in Figure 1.2 gives an overview of the development of the research cell efficiencies of the different solar cell types.

Thin film solar cells use a 1 to 2 µm thick semiconductor as the absorption layer. To complete the electric circuit the solar cell needs a front contact, the transparent conducting oxide. This so called window layer is an essential element for thin film solar cells.

The China National Building Material Company (CNBM) New Energy Research Center focuses on CdTe solar cell technology. The current efficiency record for a research cell is 21.5 %, reached by First Solar. The CNBM New Energy Research Center achieved 14.1 %. One way to improve the efficiency of the cell is to produce advanced TCOs. There

is a huge variety of methods used to deposit a thin film. Sputtering represents an outstanding candidate. It is a widely used physical vapor deposition technique, since it combines conceptual simplicity, versatility, and relatively high deposition rates. An additional feature of the sputtering process is the existence of energetic particles that bombard the growing film and provide means for the selective control of the film properties. Herein, a hollow cathode sputtering system (HCSS) is a tremendously promising way to deposit TCOs with a high transparency and low resistivity more efficiently. Thus, this work has the objective to assemble and operate completely new designed and custom-made HCSS. Included is a thoroughly theoretical elaboration of the hollow cathode sputtering system. An overview of all the deposition methods is given in Chapter 2. Chapter 3 and 4 focus on the thin film theory and on the sputtering technology, respectively. In chapter 4 the built hollow cathode system is explained in detail. Thereby, a profound insight into all the components and their functionality is offered. Furthermore, an in depth discussion about the operation of the HCSS in included in Chapter 5. In the last chapter, first experiments which were conducted after the assembly of the vacuum part of the system are described and evaluated.

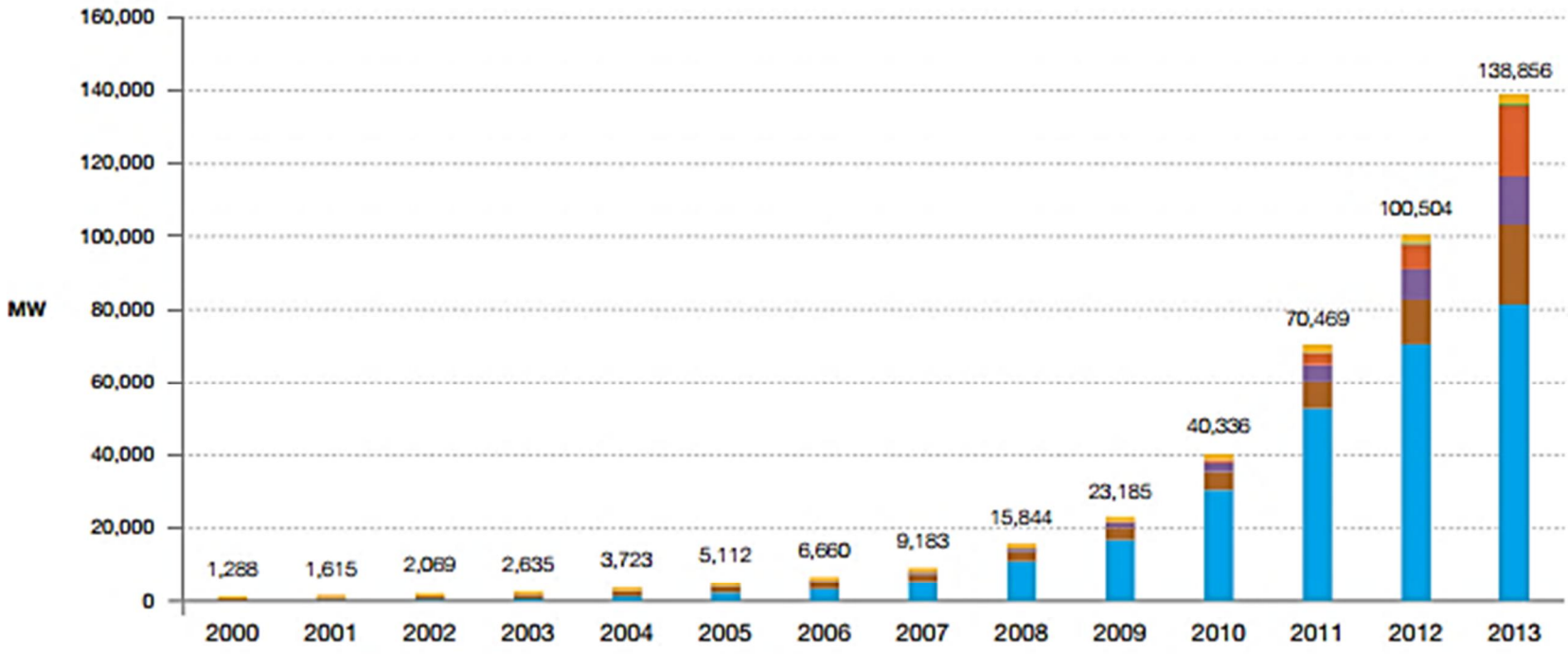

	2000	2001	2002	2003	2004	2005	2006	2007	2008	2009	2010	2011	2012	2013
RoW	751	807	887	964	993	1,003	1,108	1,150	1,226	1,306	1,590	2,098	2,098	2,098
MEA	n/a	n/a	n/a	n/a	1	1	1	2	3	25	80	205	570	953
China	19	24	42	52	62	70	80	100	140	300	800	3,300	6,800	18,600
Americas	21	24	54	102	163	246	355	522	828	1,328	2,410	4,590	8,365	13,727
APAC	368	496	686	916	1,198	1,502	1,827	2,098	2,628	3,373	4,951	7,513	12,159	21,992
Europe	129	265	399	601	1,306	2,291	3,289	5,312	11,020	16,854	30,505	52,764	70,513	81,488
Total	**1,288**	**1,615**	**2,069**	**2,635**	**3,723**	**5,112**	**6,660**	**9,183**	**15,844**	**23,185**	**40,336**	**70,469**	**100,504**	**138,856**

Figure 1.1 Evolution of Global PV Cumulative Installed Capacity 2000 to 2013 [1].

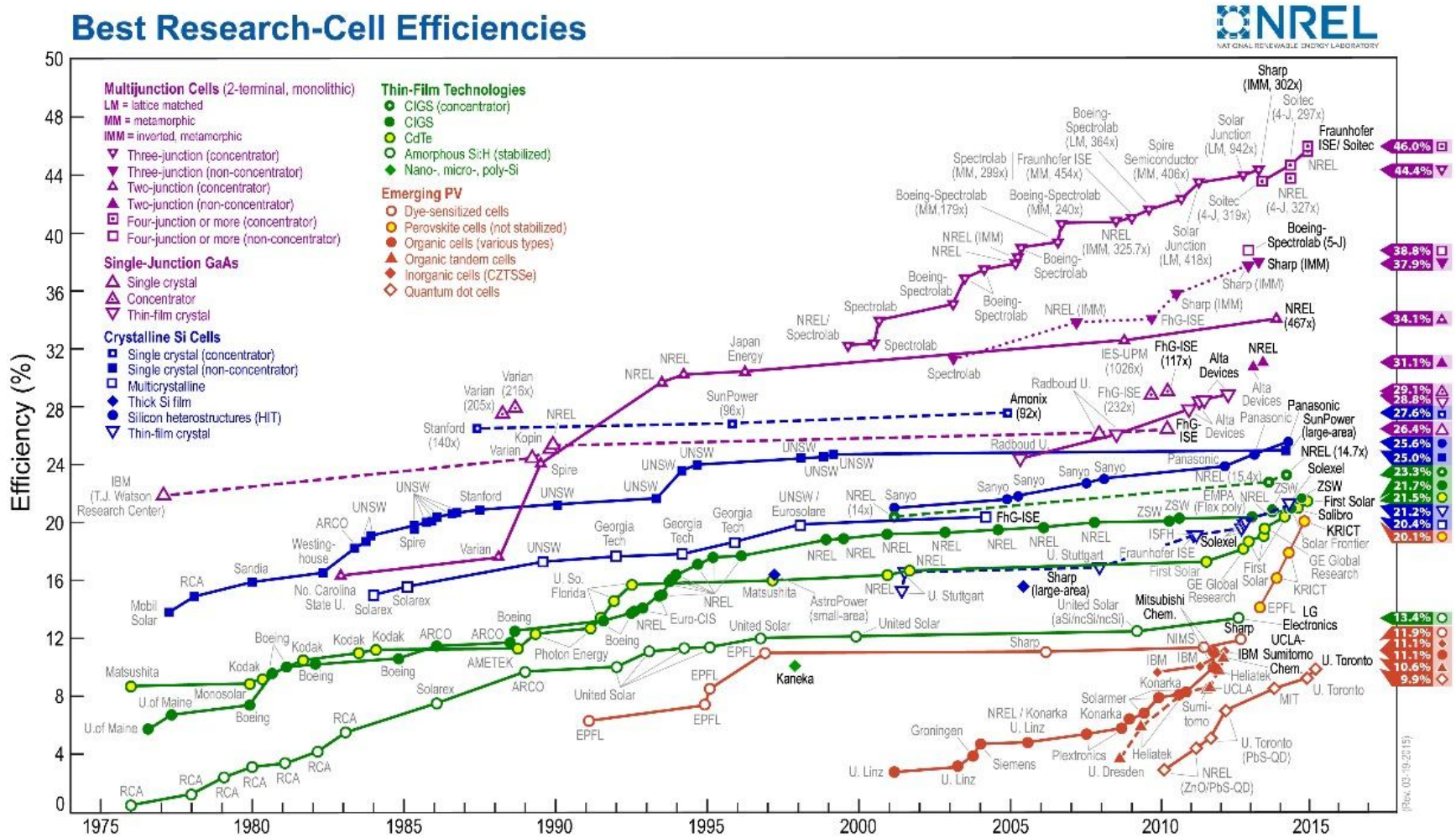

Figure 1.2 Research Cell Efficiencies [2].

CHAPTER 2

DEPOSITION METHODS

There is an immense variety of deposition methods for thin films. In general, the methods are differentiated between chemical vapor deposition and physical vapor deposition. In the following subchapters the different deposition methods are introduced. At the end of Chapter 2, a comparison of all the deposition methods reveals the benefits of the hollow cathode sputtering process and hence, underlines the main motivation for building a HCSS.

2.1 Chemical Vapor Deposition

Chemical vapor deposition (CVD) is a process whereby a solid material is deposited from a vapor (the precursor) by a chemical reaction occurring on or in the vicinity of a normally heated substrate surface. It is a widely used method in semiconductor technology for the preparation of thin monocrystalline films of high purity. The thin films are often deposited on a substrate of the same material (e.g. Si upon Si). This process is called homeoepitaxy. The process when depositing on a different material is called heteroepitaxy [3]. The solid material is obtained as a coating, powder, or as single crystals. The decomposition of the precursor can be triggered by high temperature, plasma, or light [4]. By varying the experimental conditions—substrate material, substrate temperature, composition of the reaction gas mixture, total pressure gas flows, etc.—materials with different properties can be grown [5].

In typical CVD, the substrate is exposed to one or more instable precursors, which react and/or decompose on the substrate surface to produce the desired deposit. Frequently,

volatile by-products are also produced, which are removed by gas flow through the reaction chamber.

In general, CVD involves a reaction of one or more gaseous reacting species on a solid surface, which is called the substrate. Metallic oxides, e.g. CdO, are grown by the vaporization of suitable organometallic compounds. A vapor containing the condensate material is transported to a substrate surface, where it is decomposed. This happens usually by a heterogeneous process. The nature of the decomposition process varies according to the composition of the volatile transporting species. To avoid formation of powdery deposits, which may result in haziness in the film, the decomposition reaction occurs only at or near the substrate surface and not in the gaseous phase [6].

The typical chemical reactions applied in CVD are [3]:

(i) Pyrolysis (also spray pyrolysis), e.g. decomposition at high temperatures

(ii) Photolysis, e.g. decomposition caused by ultraviolet or infrared light

(iii) Reduction of chlorides, e.g. $SiCl_4$ or $SiHCl_3$

The pressure range of a CVD process can vary between a few Torr to above atmospheric pressure [4]. A general categorization of CVD methods is based on the activation method, the type of precursor, and the working pressure. Thus, CVD methods are divided into

(i) Atmospheric pressure CVD (APCVD)

(ii) Low pressure CVD (LPCVD)

(iii) Plasma enhanced CVD (PECVD)

(iv) Photo CVD

(v) Metalorganic CVD (MOCVD)

The first two are the most widely applied methods in solar cell applications. APCVD does not require a vacuum. It gives a high deposition rate and hence, offers great cost benefits [4]. This method is widely used in the flat glass industry and especially for fluorine doped tin oxide film deposition. Zinc oxide films are also deposited by APCVD. However, low pressure CVD has become an important process to deposit boron doped ZnO films for a-Si and s-Si/μc-Si solar cell applications [4]. A feature of this process is that only low substrate temperatures in the area of 140-160 °C are required [4]. This makes it possible to additionally deposit textured ZnO as a rear contact after the junction of the solar cell is formed [4]. The operating pressure for LPCVD ranges from about 0.4 Torr to several Torr. A typical CVD system is shown in Figure 2.1.

The vapors of a volatile compound are carried by a gas, e.g. O_2, N_2, or Ar, from a hot bubbler through a heated line to a reaction chamber where oxygen or water is introduced. In this growth chamber the vapors decompose and the homogenous oxide films form at the preheated substrate surface. The quality of the thin films strongly depends on the process parameters substrate temperature, gas flow rate, and system geometry [6].

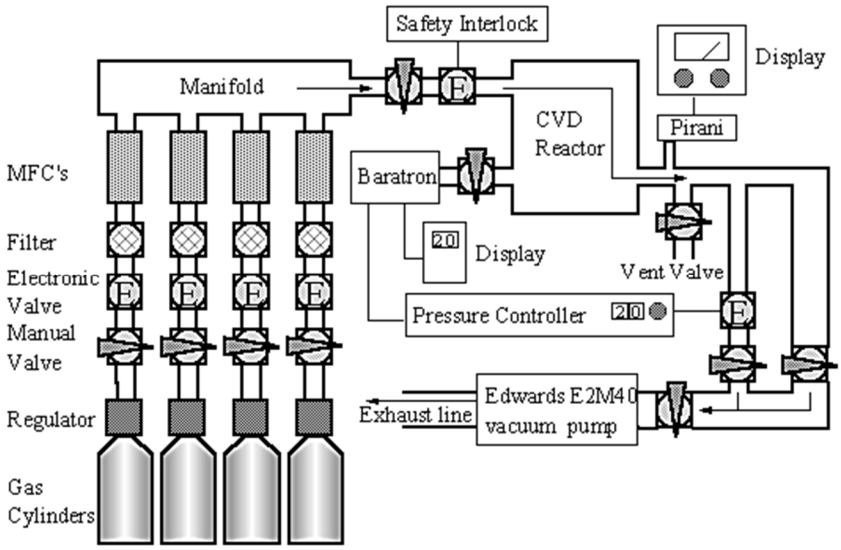

Figure 2.1 Typical CVD System [7].

The main advantages of using a CVD process are simplicity, reproducibility, and the relatively easy adoption to large-scale production line. In addition, the costs of production are comparably low due to the usage of low cost equipment. With chemical vapor deposition thin films of high purity, stoichiometry, and structural perfection can be obtained.

2.2 Physical Vapor Deposition

As indicated before, physical vapor deposition consists of two main areas: evaporation and sputtering. In the following two sections both basic physical vapor deposition methods are introduced.

2.2.1 Evaporation

Although vacuum evaporation is one of most widely used techniques for the growth of semiconducting thin films, it has not been extensively applied in the growth of transparent conducting oxides [6]. There are two ways to evaporate the charge material: thermal and electron beam evaporation. A schematic chart of the thermal evaporation process is shown below.

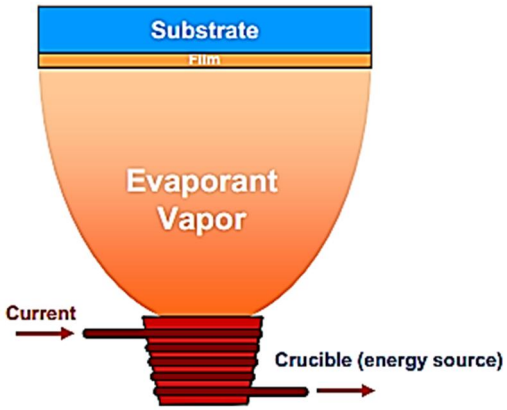

Figure 2.2 Schematic Chart of the Thermal Evaporation Process [8].

The source material to be deposited is loaded into a container called crucible. Around the crucible is a heat source. If a high temperature is reached, the source material evaporates. The evaporant vapor transports to and impinges on the surface of the substrate. Furthermore, the evaporant condenses on and is adsorbed by the surface.

The electron beam evaporation utilizes electron to vaporize the source material.This process is illustrated in figure Figure 2.3.

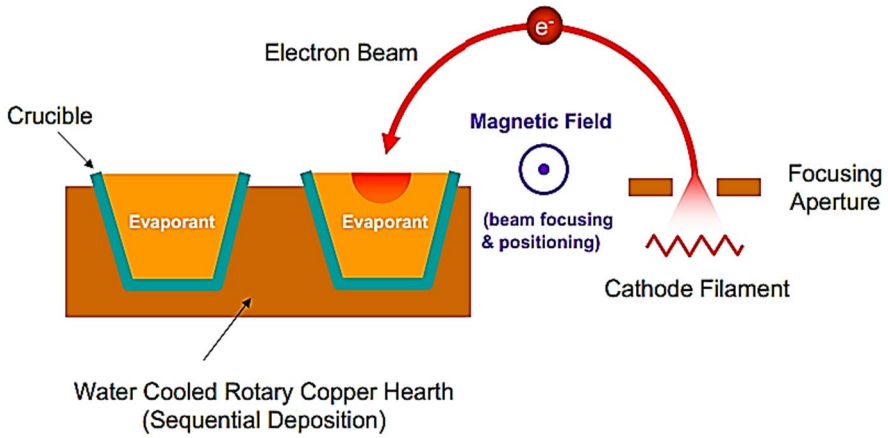

Figure 2.3 Schematic Chart of Electron Beam Evaporation [8].

The advantage of e-beam evaporation is the fact that there is a very low container contamination.

Generally, the transparent conducting oxides can be evaporated in three ways [6]:

(i) By directly evaporating of metal oxides, e.g. SnO_2, In_2O_3, or Cd_2SnO_4

(ii) By reactive evaporation of the metal in the presence of oxygen

(iii) By post-oxidation of metal films.

Important process parameters are, similar to all the aforementioned deposition methods, the substrate temperature, source-to-substrate distance, oxygen partial pressure, and the evaporation rate [6].

2.2.2 Sputtering

Sputtering is one of the most versatile methods used for the deposition of transparent conducting oxides when high quality films are required. This section provides general information about the different sputtering methods. Chapter 3 offers a detailed analysis of the sputtering process in regards to the hollow cathode sputtering.

Compared with other deposition techniques, the sputtering process produces films with higher purity and better controllable composition. Moreover, it provides films with greater adhesive strength and homogeneity, and permits better control of the film thickness. The process involves the creation of a gas plasma (a glow discharge) which is usually an inert gas, e.g. argon. The plasma is created by an applied voltage between the cathode and the anode. The cathode is used as a target holder and the anode is used as a substrate holder. The source material is subjected to intense ion bombardment. By momentum transfer, particles are ejected from the surface of the cathode and they diffuse away from it, depositing a thin film onto a substrate [6].

Considering the power source/excitation types, three main sputtering modes can be distinguished:

(i) DC sputtering: DC power between the cathode and anode

(ii) Radio frequency (RF) sputtering: high frequency generator connected between the electrodes

(iii) Magnetron sputtering: magnetically enhanced gas discharge

All three ways can be run in non-reactive and reactive mode. Magnetron sputtering systems make use of the fact that a magnetic field configured parallel to the target surface can constrain secondary electron motion to the vicinity of the target. The magnets are arranged in such a way that one pole is positioned at the central axis of the target and the

second pole is formed by a ring of magnets around the outer edge of the target. Trapping the electrons in this way substantially increases the probability of an ionizing electron-atom collision occurring [9]. Magnetron sputtering is very suitable and cost-effective for large-scale TCO production. This process is used to manufacture ITO for the flat-panel display industry and ZnO:Al for a-Si and CIGS modules. It is generally conducted using multiple-chamber in-line coaters with either horizontal or vertical substrate transport. An example of a reactive magnetron sputtering system is shown in Figure 2.4. Magnetron sputtering is an excessively used and commercially available PVD method.

Different sputtering configurations exist according to the type of cathode, sputtering power supply, and target material. An overview of the sputtering configurations is elucidated in Table 2.1.

Table 2.1 Different Sputter Configurations [4]

Type of cathode	Excitation and target type		
	RF	DC	MF
Planar magnetron	C	M, C	M, C
Cylindrical magnetron		M, C	M, C
Hollow cathode		M	M
Dual planar		M, C	M, C
Dual cylindrical		M, C	M, C

M: metallic target, C: ceramic target

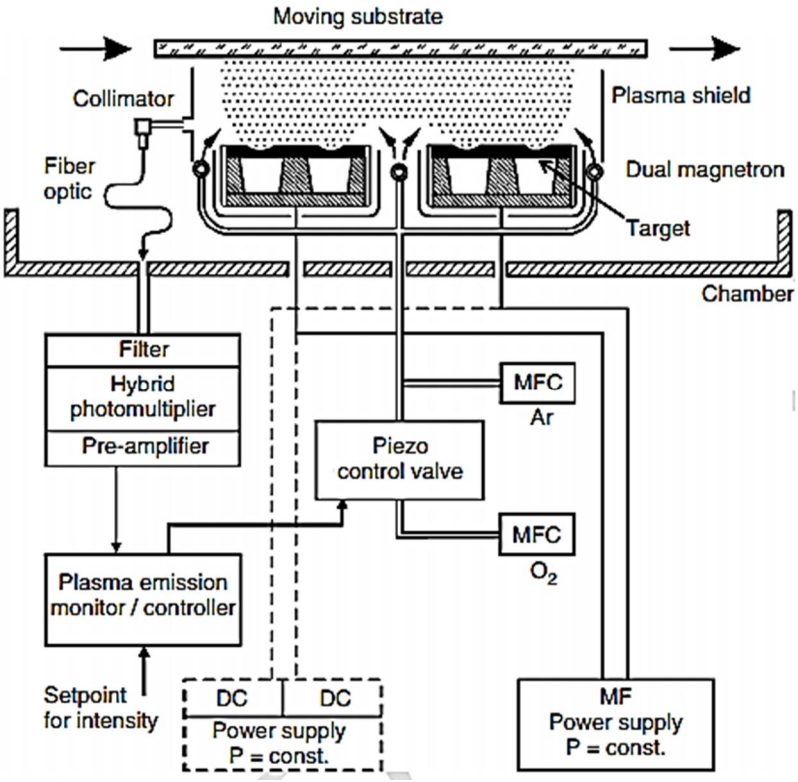

Figure 2.4 Schematic Diagram of a Reactive Magnetron Sputtering System [4].

2.3 Comparison of Deposition Methods

As it was expounded in the previous sections, various deposition techniques such as CVD, spray pyrolysis, sputtering, evaporation, etc., can be employed for the growth of transparent conducting oxides. The properties of the resulting films depend significantly on the deposition parameters of each method. For the growth of reproducible high quality films, CVD and sputtering are the most suitable deposition methods. Even though sputtering is more complex and expensive, it offers a good deposition rate and a very good control of the film composition and thickness. A general comparison of the different deposition techniques is depicted in Table 2.2.

Table 2.2 Comparison of Various Deposition Methods [6]

Deposition method	Substrate temperature	Growth rate	Film uniformity	Reproducibility	Cost	Conductivity	Transmission
CVD	High	High	High	High	Moderate	Moderate-excellent	Moderate-excellent
Spray	High	High	Poor	Moderate	Low	Moderate-excellent	Moderate-excellent
Sputtering	Low	Moderate	Excellent	Excellent	High	Excellent	Excellent
Ion plating	Room	Low	Excellent	Excellent	High	Excellent	Excellent
Evaporation	High	High	Moderate	Moderate	Moderate	Moderate-excellent	Moderate

CHAPTER 3

HOLLOW CATHODE SPUTTERING

3.1 The Physical Nature of Sputtering

3.1.1 Interactions of Ions with Surfaces

When atoms or ions have energies above a threshold of 20 - 50 eV and strike a surface, material from that surface is ejected [10]. This is the physical nature of sputtering. It is much easier to accelerate ions in a controlled manner rather than to provide beams of energetic neutrals. Hence, sputtering is almost always accomplished using ions [11].

When an ion approaches the surface of a solid, different phenomena can occur [12]:

(i) The ion may be reflected and is probably being neutralized in the process. This reflection can be used to characterize the chemical and structural makeup of materials, which is an analytical technique known as Ion Scattering Spectroscopy (ISS).

(ii) Secondary Electron Emission: The impact of the ion may cause the target to eject an electron.

(iii) Ion Implantation: The ion may become buried in the target. This technique is excessively used in integrated circuit technology for selectively doping silicon wafers with precisely controlled amounts and depth profiles of specific impurities.

(iv) Structural Rearrangements: The ion impact may also cause structural rearrangements in the target material. This can vary from simple vacancies (missing atoms) and interstitials (atoms out of position), to lattice defects such as change of stoichiometry in alloy or compound targets. Furthermore, it can be consequence of change in electric charge levels and distributions. All of the aforementioned is collectively referred to as radiation damage which is a subject of great importance (relation to nuclear energy). Radiation damage can often be removed by annealing

(heat treatment), but is not always unwanted. In that case it is identified as altered surface layers.

(v) Sputtering: The ion impact may set up series of collisions between atoms of the target, often leading to the ejection of one these atoms.

These different phenomena are illustrated in Figure 3.1.

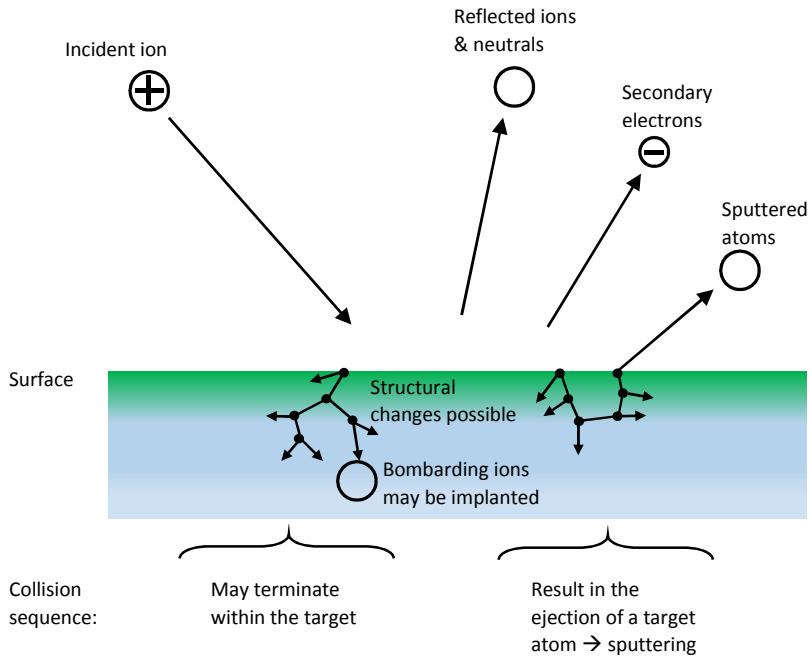

Figure 3.1 Interactions of Ions with Surfaces (Adapted from [12]).

The following paragraph is taking a closer look at the sputter mechanism.

In the energy range most relevant to sputter deposition, the interaction between the impinging ion and the target atoms, and the subsequent interactions amongst the latter, can be treated as a series of binary collisions. Thereby the incident particle could be either an ion or a neutral atom. Usually, ions are used because they can easily be accelerated by an electric field. But ions are likely to be neutralized by the Auger emission of an electron from the target as the ion approaches. Hence, the impacting particles are mostly neutral [12].

The series of collisions in the target, generated by the primary collision at the surface, is known as a collision cascade. It will be a matter of luck whether this cascade leads to the sputter ejection of an atom from the surface or whether the energy of the cascade heads off into the interior of the target. The first case will require at least two collisions. In the second case energy is dissipated from the primary impact to lattice vibrations, e.g. heat. Therefore, sputter ejection is rather inefficient, with typically 1% of the incident energy reappearing as the energy of the sputtered atoms.

3.1.2 Sputter Target Kinetics

Due to the fact that the interactions in a sputtering target are sufficiently short range, only interactions between intermediate neighbors have to be considered. A binary collision is characterized by the energy transfer function which is shown in the following equation.

$$\frac{E_t}{E_i} = \frac{4m_i m_t}{(m_i + m_t)^2} \tag{3.1}$$

Where m_i and m_t are the masses, and E_i and E_t the energies of the colliding atoms. The sputter process is the result of a series of such collisions [12].

A useful parameter to characterize the sputter process at the target is the sputtering yield S. The sputter yield S is defined as the number of target atoms (or molecules) ejected per incident atom. The sputter yield depends on the energy and angle of incidence of the ion, the mass of the ion and target atoms, and the binding energy of the surface atoms. The sputtered atoms land on the substrate with an average of about 5 eV of kinetic energy. This quantity can be influenced by the process gas pressure in the vacuum vessel and the target-substrate distance [4].

If sputtering is considered as the overall process of transferring energy from the incident ion to the sputtered atoms, the sputtered atoms can only come from the surface layers of the target. Henceforth, the sputter process is not just a question of transferring energy to the target atoms, it also includes the energy transfer to the surface layers.

The sputter yield S is proportional to the energy deposited in a thin layer near the surface which is determined by the nuclear stopping power s(E) [12]:

$$s(E) = \frac{3\alpha}{4\pi^2}\frac{4m_i m_t}{(m_i + m_t)^2}\frac{E}{U_o} \tag{3.2}$$

U_o is the surface binding energy of the material being sputtered (target), and α is monotonic increasing function of m_t/m_i.

This expression for S (see equation (3.2)) predicts that the yield will increase linearly with E. In practice this seems to be satisfied up to a 1 keV, above which S becomes relatively constant. At very high energies, S decreases as ion implantation becomes dominant (see Figure 3.2).

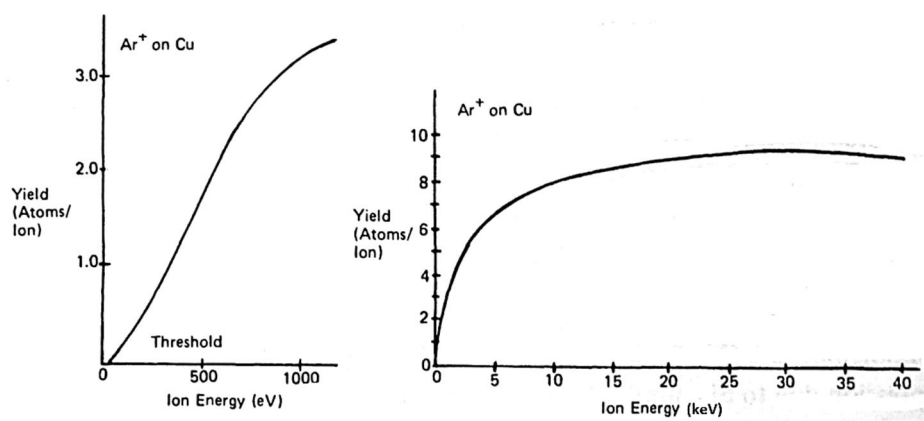

Figure 3.2 The Variation of Sputter Yield as a Function of Ion Energy, for Ar on Cu [12].

Hence, for a nuclear stopping power S above 1 keV there is an adjusted equation which describes the sputter process more precisely. The modified interaction yield can be determined with [12]:

$$S = 3.56\alpha \frac{Z_i Z_t}{{Z_i}^{2/3} + {Z_t}^{2/3}} \frac{m_i}{(m_i + m_t)} \frac{s_n(E)}{U_o} \tag{3.3}$$

Where $s_n(E)$ is a reduced stopping power and is a function of the reduced energy based on the actual energy, masses and atomic numbers Z_i and Z_t of the involved atoms.

Table 3.1 illustrates the sputter yield as well as the threshold energy using Argon as a process gas for some elements [13].

Table 3.1 Sputter Yield for Ar and Ar Threshold for Various Metals [13]

Element	Sputter Yield for Ar at 500 eV [atoms/ion]	Ar Threshold Energy [eV]
Al	1.05	13
Au	2.40	20
C	0.12	-
Ni	1.45	21
Si	0.50	-
Ta	0.57	26

In Figure 3.3 the sputter shields of different inert gases are plotted versus the ion energy for silicon.

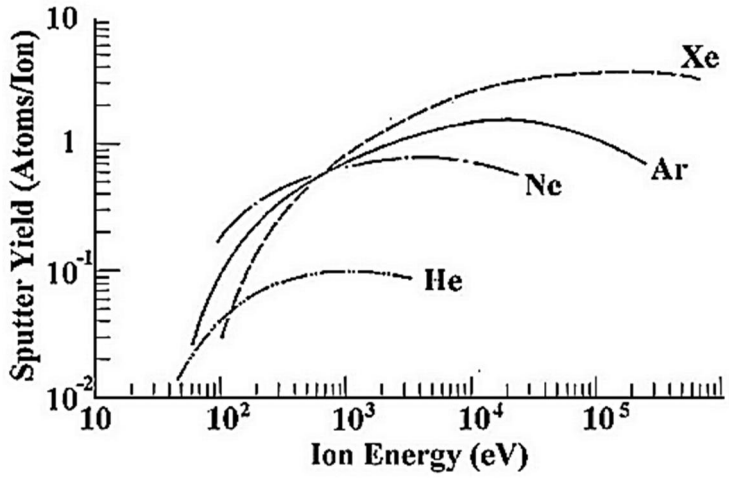

Figure 3.3 Sputter Yield Depending on the Ion Energy for Different Inert Gases [14].

According to Figure 3.3 and to Equation (3.2) the heaviest inert gas should suit the best for the sputter process. Radon is the heaviest, but it also radioactive. Xenon and krypton follow. Even though, argon is almost always used in sputter processes. The reason for that lies in the good availability and the low price of argon. Moreover, the sputter yield is only a factor of about two smaller than the one of xenon. Often a high purity argon gas is applied [12].

3.1.3 Thin Film Formation

In sputtering, the target material arrives at the substrate in an atomic or molecular form. The atom diffuses around the substrate with a motion determined by its binding energy to the substrate. Moreover, the particle motion is influenced by the nature of the substrate and the substrate temperature. The steps of the general process of thin film growth are depicted in Figure 3.4.

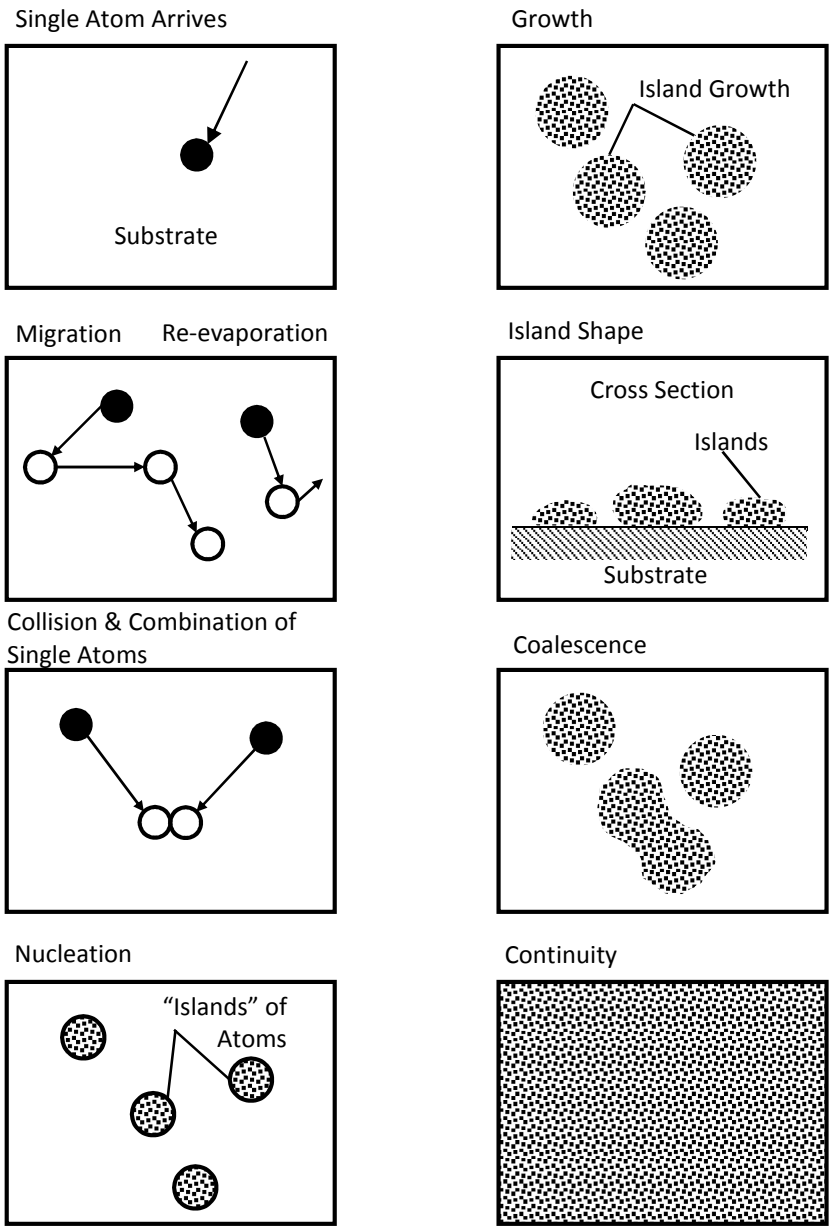

Figure 3.4 Steps of Thin Film Growth (Adapted from [15]).

At first, single atoms sputtered from the target are adsorbed at the substrate surface. These atoms move along the substrate surface, they diffuse, until they rest at a stationary position. After a particular time the sputtered atom will either evaporate from the surface of the substrate or will join with another diffusing single atom to form a doublet. A doublet is less mobile but more stable than the single atom [12]. The crucial factor of the atomic

pair (doublet) formation is the single atom density and thus, the arrival or deposition rate [12]. Over time, more and more atoms come to the doublet to form triplets, quadruplets and so on. This process is called nucleation. The nucleation stage of the thin film growth process leads to the formation of quasi-stable islands. These islands comprise tens of hundreds of atoms and usually have densities of about 10^{10} cm^{-2}. In the next growth stage the islands gain in size. Eventually, the island becomes big enough to tough adjacent islands. This process is known as agglomeration or coalescence. The agglomeration lingers until the thin film reaches its final growth stage: the continuity. This final stage occurs in some cases not before the film is several Å in average thick.

On a polycrystalline substrate the orientation of each of the island is random and therefore different. Hence, the thin film is polycrystalline in nature. On a single crystal substrate the island orientations may be determined by the substrate structure. Consequently, growth and coalescence lead to a single crystal thin film. This phenomenon is called epitaxy [12].

In thermodynamic equilibrium the atoms rest at the position where their potential energy is minimized. This is defined by the energy term Δγ [16]:

$$\Delta\gamma = \gamma_d + \gamma_i - \gamma_s$$

γ_d Surface free energy of the deposit

γ_i Surface free energy of the interface

γ_s Surface free energy of the substrate

There are three basic modes of thin film growth which can be distinguished due to the balance between the surface free energy of the deposit, of the interface and of the substrate (see Figure 3.5):

$$\begin{aligned} &\text{(i)} \quad \Delta\gamma > 0 \Rightarrow \gamma_d + \gamma_i > \gamma_s \\ &\text{(ii)} \quad \Delta\gamma = 0 \Rightarrow \gamma_d + \gamma_i = \gamma_s \\ &\text{(iii)} \quad \Delta\gamma < 0 \Rightarrow \gamma_d + \gamma_i < \gamma_s \end{aligned}$$

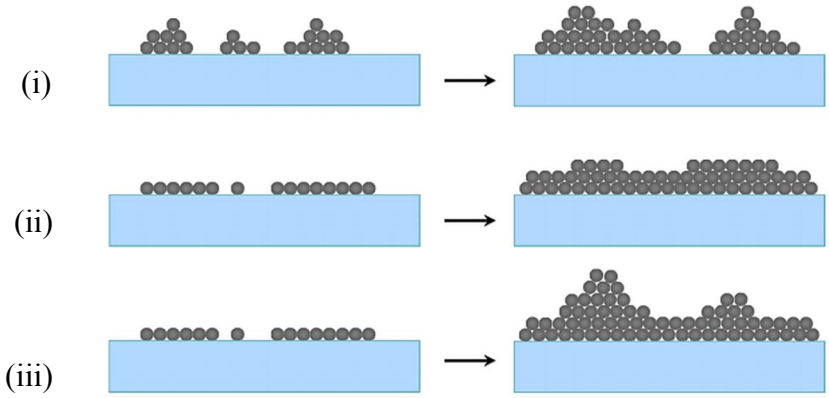

Figure 3.5 The Three Modes of Thin Film Growth [16].

In the case (i) the deposit is more strongly bound to itself than to the substrate. This is referred to the island growth process (also known as Volmer-Weber growth). Conversely, the so called layer growth occurs in (ii) which is also known as Frank-Van der Merwe growth). The nuclei only grow in two dimensions. Thus, a layer by layer formation happens here. Case (iii) is a combination of the two aforementioned growth modes known as Stranski-Kranstanov growth [16].

During the sputter deposition the growing film is bombarded by energetic particles of the plasma (electrons or negative ions). In Figure 3.6 are the effects of energetic bombardment on a growing thin film illustrated. At moderate energies, bombarding ions cause a smoothing and densification of the growing film due to backscattering and

resputtering. Impinging ions can also be implanted. The result are displacements and lattice defects.

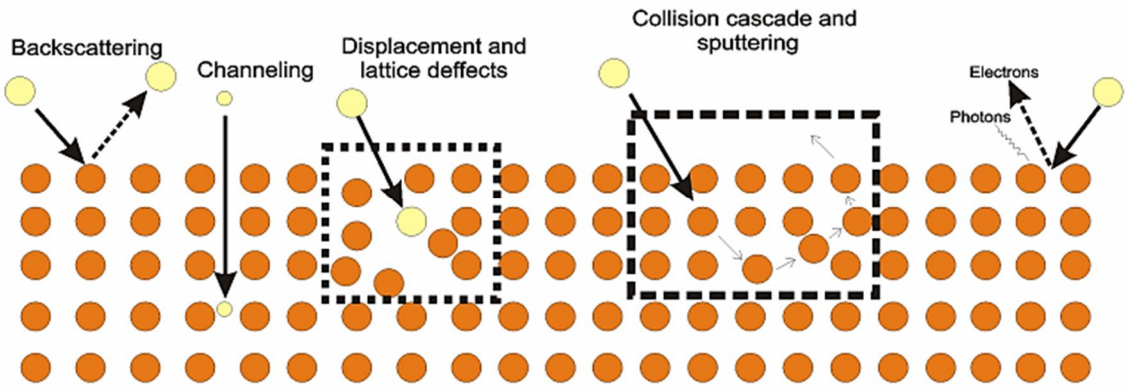

Figure 3.6 Effects of Energetic Bombardment on a Growing Thin Film [17].

Considering the reactive mode, the film formation strongly depends on the oxygen content in the vacuum chamber. At low partial pressure, metal is sputtered from the target and the oxidation reaction occurs only on the substrate (see Figure 3.7). Oxidation of the target surface ensues at higher partial pressures. In that case the sputtering rate decreases rapidly [6].

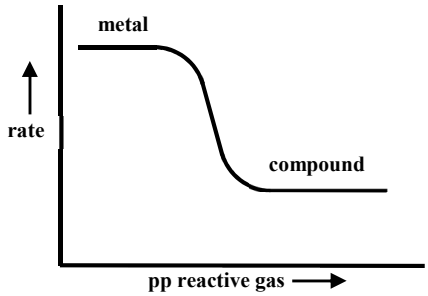

Figure 3.7 Qualitative Plot of the Sputter Rate Against the Partial Pressure of the Reactive Gas (Adapted from [6]).

Observing the general form of the response of the partial pressure of oxygen to the oxygen flow rate, the hysteresis effect becomes evident (see Figure 3.8). As oxygen flow is initially increase most of the gas is consumed by the sputtered film. By reaching point B

the formation of an oxide starts on the target surface. Hence, a rapid transition happens (point D). If the oxygen flow rate is reduced to point C the metallic face of the target is exposed and pumping by the metallic film prevails. Metallic rich films are produced when operating on the lower curve (A to B). This requires annealing in the presence of oxygen to become transparent. For attaining an oxidized film, the operation on the upper curve (D to C) is necessary. This film becomes conducting on annealing in a reducing atmosphere. The straight line in Figure 3.8 indicates the position before plasma ignition [6].

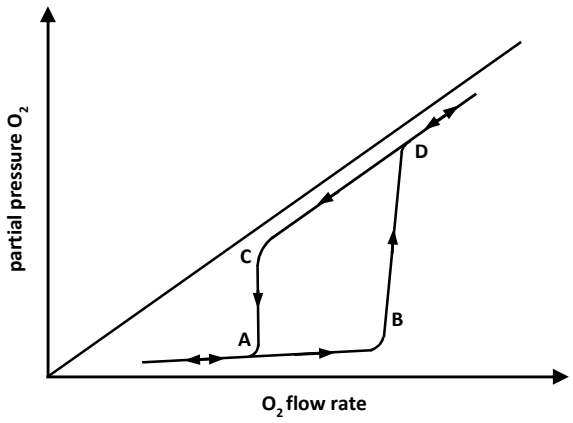

Figure 3.8 Typical Hysteresis Form of the Oxygen Partial Pressure against the Oxygen Flow Rate of the Sputter Process (Adapted from [6]).

3.2 DC Sputtering

3.2.1 The General DC Sputter Process

In DC sputter processes the target is almost always a solid. However, powders or liquids are sometimes used. In a typical sputter system the target forms the cathode which has a high negative DC voltage applied to it. The substrate, where the thin film is deposited, is placed on an electrically grounded anode. These electrodes are housed in an evacuated chamber. Argon is introduced into the chamber as the process gas. The purpose of the

applied electric field is to accelerate electrons which collide with argon atoms. Some of the argon atoms are broken up into argon ions and more electrons which produce the glow discharge (plasma discharge). The produced charged particles are accelerated by the electric field. Electrons tend towards the anode and ions towards the cathode. Thus, a current I flows [12]. A schematic of a DC sputtering system is revealed in Figure 3.9.

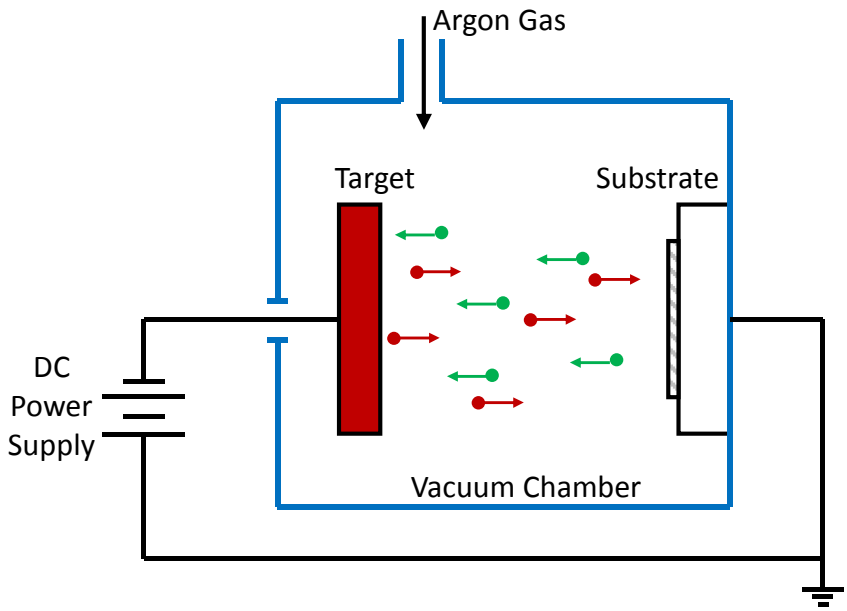

Figure 3.9 Basic Structure of a DC Sputtering System.

The voltage V which is required to drive the current I through the system is a function of the system pressure. The sputter rate is strongly dependent on the ion flux at the target which is proportional to the current. Consequently, the sputter rate is linearly dependent on the current. Furthermore, the sputter rate is connected to the sputter yield S and hence, reliant on the ion energy. Henceforth, the sputter rate is also dependent on the system voltage which determines the sheath voltage at the target. As a result, the sputter system pressure as well as the I-V characteristic are eminently important for the overall

sputter process. A vacuum system enables to control the operating pressure inside the sputtering system. Limitations of the operating pressure are imposed by two factors:

(i) The glow discharge, and

(ii) The film deposition.

The lower pressure limit is set by the glow discharge. The glow discharge is sustained by electrons which make ionizing collisions in the process gas. If the gas density decreases, the number of ionizing collisions is reduced as well. As a direct consequence, the discharge current (assuming constant voltage) is also decreasing. This characteristic is demonstrated for different pressures in the Figure 3.10, based on a nickel cathode.

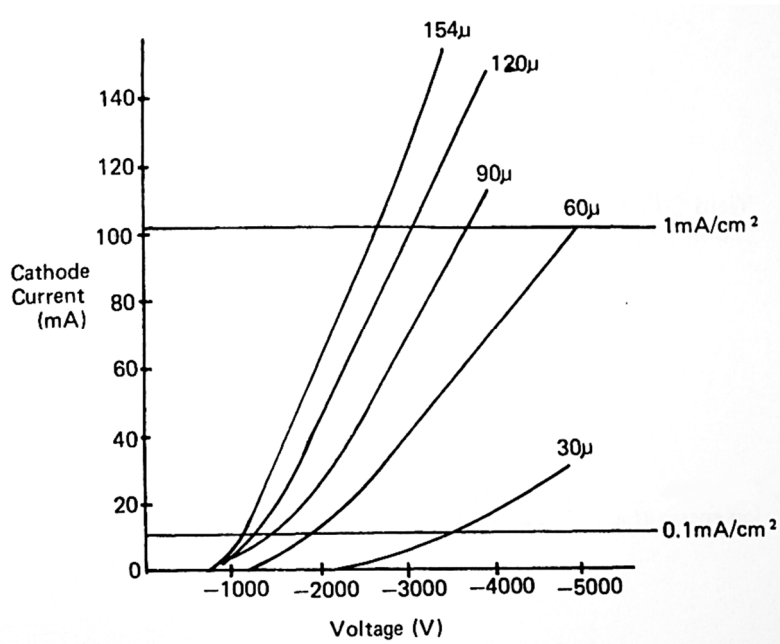

Figure 3.10 Typical I-V Curves at Different Argon Pressures (in mTorr) [12].

The pressure range of the process gas argon ranges from 30 to 154 mTorr. Below about 30 mTorr the current, and consequently the ion flux at the target, and the deposition rate in the dc discharge become small. The horizontal lines at 0.1 and 1 mA/cm^2 indicate the operating range for this specific cathode (nickel targets). A similar curve is depicted in

Figure 3.11. In this figure, different flow rates of the process gas argon are incorporated. Hereby, Cu targets were used in the sputtering process.

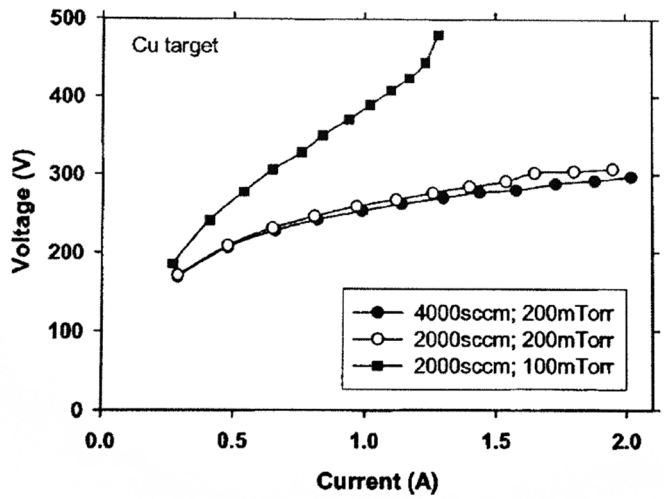

Figure 3.11 V-I Curve at Different Pressures and Ar Flow Rates [18].

The upper pressure limit is defined by the collisions of the sputtered atoms from the target with the atoms of the process gas. If the system pressure rises these unwanted collisions increase as well. The result is a diminution of the sputter rate because sputtered atoms are backscattered in the gas phase and re-deposited on the target [12]. Figure 3.12 illustrates this aspect. It can be observed that the apparent sputter yield decreases with an increase of the system pressure.

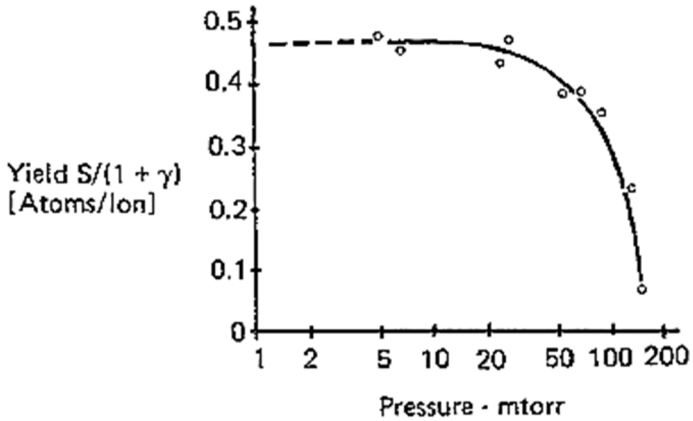

Figure 3.12 Sputter Yield Depending on the Pressure of Ar for a Ni Target [12].

An overall operating pressure of about 10 mTorr to 10 Torr is usual for dc sputter deposition [10]. To maintain the discharge, a voltage of typically a few hundred volts is required [10].

3.2.2 DC Glow Discharge

This section briefly examines the DC glow discharge in order to foster an understanding what happens in the chamber during the deposition process.

In Figure 3.13 is a typical DC glow discharge revealed. Most of the space between the two electrodes is filled by a bright glow, known as the negative glow. The negative glow is the result of excitation and subsequent recombination processes. Close to the cathode is a comparatively dark region which is called the dark space. The dark space is correlated to the sheath formed in front of the cathode. The longest part of the discharge is filled by the positive column. This is the region which most nearly resembles a plasma. Most of the classic probe studies have been made on positive columns [4]. In between the positive column and the negative glow, the so called Faraday dark space is located.

The physical characteristics of these regions depend on the parameters of the discharge, e.g. [19]:

(i) Geometry of the discharge tube,

(ii) Pressure of the working gas,

(iii) Type of gas,

(iv) Cathode material,

(v) Applied potential, and

(vi) The current flowing in the discharge.

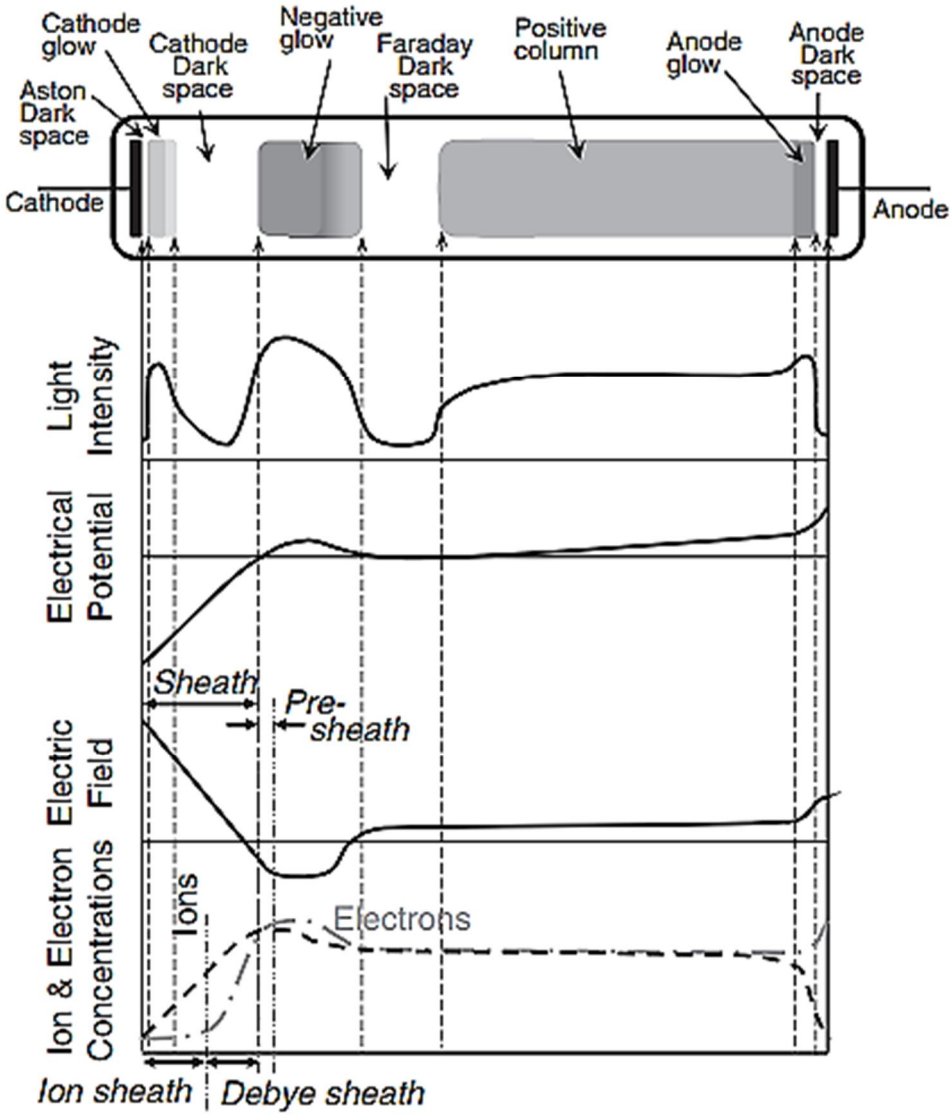

Figure 3.13 Qualitative Characteristics of a DC Glow Discharge [62].

According to the current–voltage (I–V) relation of the discharge, the glow discharge can be divided into three main regions: subnormal, normal, and abnormal discharges (see Figure 3.14). In the normal region, the potential difference across the tube becomes almost independent of the current flowing through it. The value of the normal potential is little more than the minimum breakdown voltage on Paschen's curve for the same gas and electrode. The current appears to flow from a small area of the cathode, which is covered

by the glow. This area increases as the current increases, while the current density is constant [20].

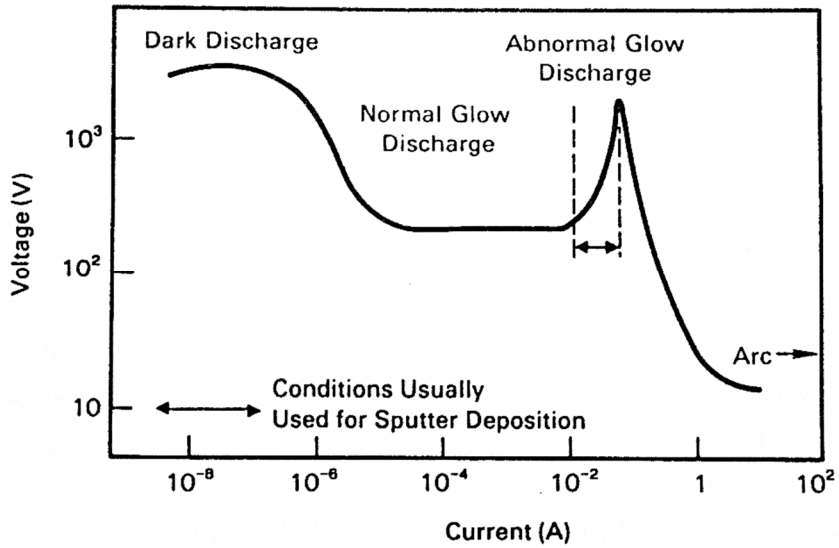

Figure 3.14 I-V Curve of a Typical Low Pressure Glow Discharge [21].

If the two electrodes are brought closer together, the cathode dark space and the negative glow are unaffected while the positive column shrinks. Eventually, only the negative glow and the dark spaces are left. This is the usual case in a glow discharge process. It is characterized by the fact that the inter-electrode separation is only a few times the cathode dark space thickness [12].

The electric potential distribution in a DC glow discharge is portrayed in Figure 3.15. The area between anode and cathode has the highest positive potential. It can be observed that sheaths are formed in the vicinity of the two electrodes. The highest voltage drop occurs at the cathode.

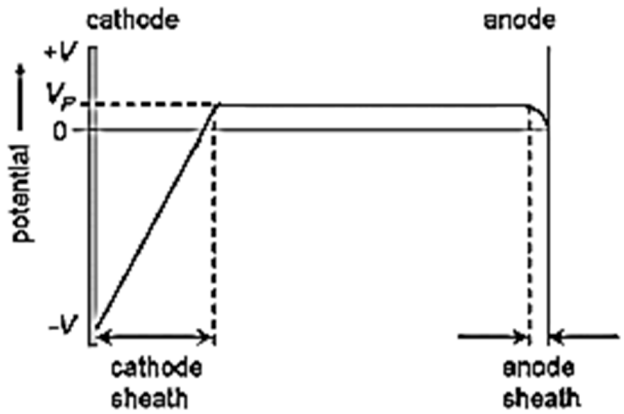

Figure 3.15 Distribution of the Potential in a DC Glow Discharge [22].

Overall, the DC glow discharge comprises of a self-consistent combination of a cathode surface, cathode dark space region, with an associated large electric field, and the negative glow region. Ions, which were originated in the dark space and the negative glow, are accelerated by the cathode electric field into the cathode surface. There the ions cause secondary electron emission and sputtering. These secondary electrons are accelerated back across the dark space and cause ionization. The hollow cathode discharge relies on those secondary electrons [23].

3.2.3 Practical Aspects of Sputtering Systems

The previous section dealt with process conditions of a sputter system. The following segment takes a closer look at practical components. Some of these components are revealed in the schematic chart in Figure 3.16.

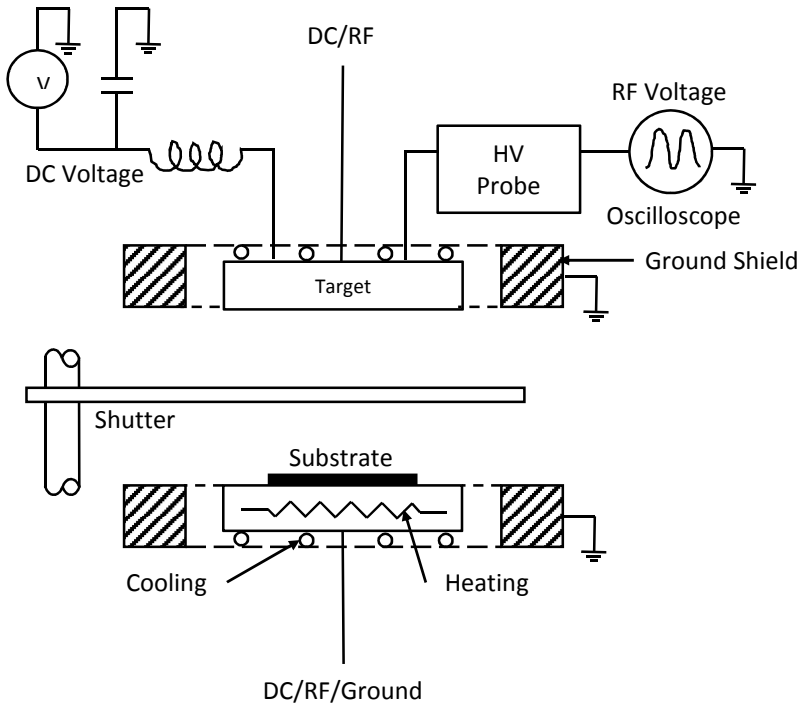

Figure 3.16 Schematic of a Sputtering System (Adapted from [12]).

One major component is the ground shield, also known as the dark space shield. The purpose of the ground shield is to restrict ion bombardment and sputtering to the target only. Without a ground shield the target backing plate, mounting clips, and mechanical supports would be sputtered and hence, would cause a severe contamination of the thin film. The space between the ground shield and the target must be less than the thickness of the dark space to prevent ion bombardment of the protected regions [12]. Particularly with DC discharges, sharp points or patches of dirt are the reason for local discharges or arcs. Thus, sharp points and dirt has to be eliminated. Some examples of ground shield implementations are illustrated in Figure 3.17.

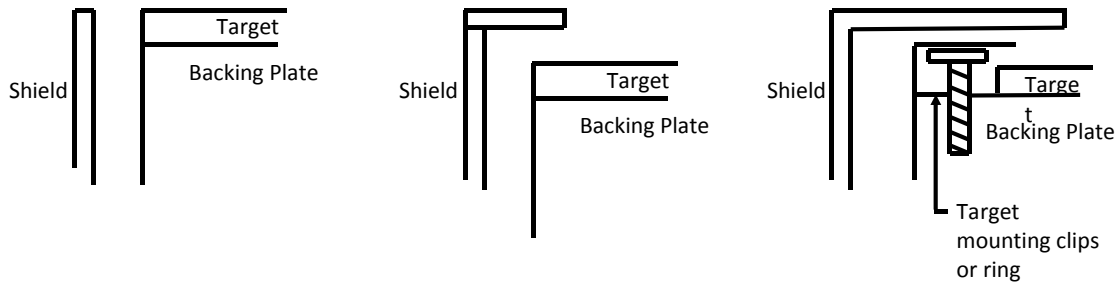

Figure 3.17 Some Possible Ground Shield Arrangements (Adapted from [12]).

Another important component which is shown in Figure 3.16 is the shutter. The shutter is there for the cleaning process of the target which happens through sputtering of the first atomic layers of the target. In case the system is open to air - for the purposes of loading or unloading the chamber – the target is liable to become contaminated by atmospheric pollution, by handling, or by chemical combination with the atmosphere to form an oxide or other compounds [12]. That is why the target needs to be cleaned by interposing the shutter during the initial sputter period. Otherwise, the substrate would be contaminated. In high vacuum applications ($p < 10^{-5}$ torr) shutters have to block everything in the line of the sight of the source [12].

In addition to ground shield and shutter, the target cooling plays a critical role in the operation of a sputtering system. Cooling of the target is necessary because the heating can become excessive. The temperature of the target can reach up to 400 °C which leads to damage of the bonding between the target and the backing electrode [12]. That is why cooling of the target is usually applied. But such a cooling system is complex and difficult to implement, especially in regards to the avoidance of water leaks in the chamber.

Next to the cooling system of the target, the temperature of the substrate surface is also an important and difficult parameter to control. The temperature on the substrate is a

central factor for the formation stages of a thin film and its final structure. Heating the target can be achieved by circulating a hot liquid or by electric heating (resistance, or halogen heaters). But there is an inherent problem in substrate temperature control. The point of interest is the actual substrate temperature. This is almost impossible because of inevitable thermal barriers. Hence, empirical methods are used to estimate the real substrate temperature. The temperature measurement are conducted by thermocouples which end is attached to the substrate holder or the bulk.

3.3 Hollow Cathode Sputtering

Hollow cathodes were first used as thermionic emitters to produce electron beams. The large area of the hollow cathode emitter prolonged the life of the delicate emitting surface at a given beam current [10]. Hollow cathode sputtering, particularly in the reactive mode, is exceptionally suitable for deposition of functional, compound thin films. The important features of this deposition method are that it offers a stable discharge, high sputtering rate in the metallic mode (poison-free target), and consequently a stable process [24].

The principle functionality of a hollow cathode is based on a cylindrical cavity. If a cylindrical cavity is drilled in a solid cathode material and a glow discharge is struck, the negative glow, surrounding the cathode, will penetrate into the cavity. Thereby, the cavity diameter D is twice the dark space length d_0. The dark space length is empirically related to the pressure p and the current density j by the relation

$$d_0 = \frac{C_1}{p} + \frac{C_2}{\sqrt{j}} \tag{3.4}$$

where C_1 and C_2 are constants. Usually, the current density is two to three times the magnitude compared to a planar cathode. The reason for that is the pendulum effect.

Fast secondary electrons emitted from the cathode are reflected back and forth by the electric field in the dark spaces of the opposing cathode surfaces. This effect is depicted in Figure 3.18.

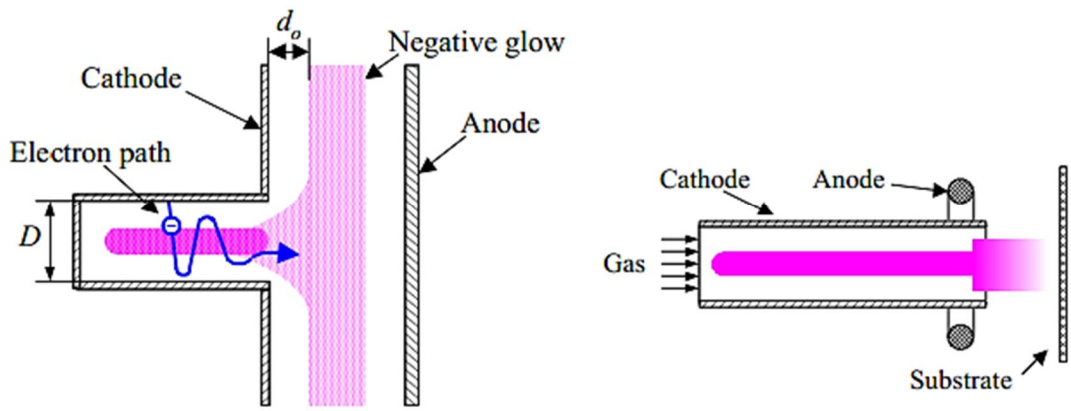

Figure 3.18 Penetration of Plasma into the Cathode Cavity (Left), a Gas Flow Cylindrical Hollow Cathode (Right) [25].

Compared to a planar cathode or a magnetron cathode the plasma density of a hollow cathode is much higher. In the often applied reactive mode a sufficiently high flow rate of the process gas argon through the cavity of the cathode prevents back-streaming of the reactive gas into the cavity. Thus, target poisoning is eliminated. Target poisoning, which occurs with conventional reactive magnetron sputtering, leads to drastic reduction of the deposition rate and to arcing at the insulating regions of the target surface. The target can occur in stable metallic or oxidized states when using oxygen as reactive gas. Between those two sates are transitions. This forms the hysteresis curve as a function of oxygen flow. Most processes require that the target exist in an intermediate (and normally inaccessible) oxidation state that requires active feedback to maintain.

An example of a hollow cathode sputtering system with a linear hollow cathode source is illustrated in Figure 3.19. In that system, built by Energy Photovoltaics Inc., a mid-frequency pulsed power supply is deployed. The figure reveals the characteristic

setting inside a vacuum chamber used for hollow cathode sputtering. Typical cathode dimensions and operating parameters are shown in Table 3.2.

Table 3.2 Typical Cathode Dimensions and Operating Parameters [10]

Dimension/parameter	Value
Cathode length (internal)	9.91 cm
Cathode depth	4.06 cm
Slot width	1.27 cm
Cathode surface area	90.8 cm^2
Sputtering power	50 – 1400 W
Frequency	50 – 100 kHz
Power density	0.55 – 15.4 W cm^{-2}
Gas flow	2000 – 6000 sccm
Gas velocity (peak)	256 – 770 m s^{-1}
Chamber pressure	100 – 500 mTorr
Pressure in the cathode (average)	300 – 750 mTorr

As seen in Figure 3.20, the main body of a hollow cathode is made of copper. The coolant (often chilled water) flows through the copper body. Inside of the rectangular cathode are the target plates located. The target plates are removable and mounted onto the copper body via screws. Sometimes the target plates are welded onto the copper body. The process gas flows directly through the rectangular orifice of the cathode.

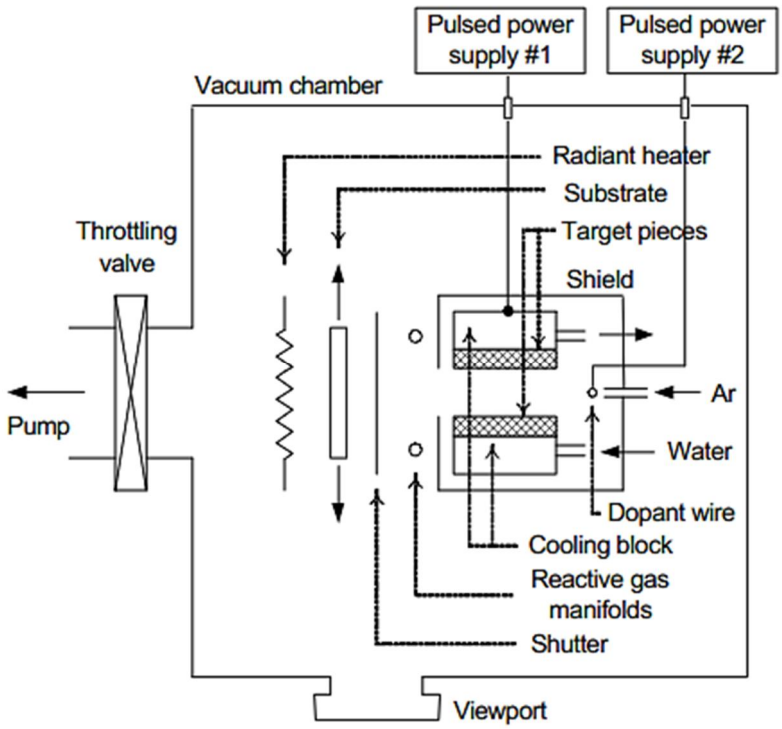

Figure 3.19 Schematic of the Interior of a Vacuum Chamber for HCS [25].

A basic linear hollow cathode design is exemplified Figure 3.20.

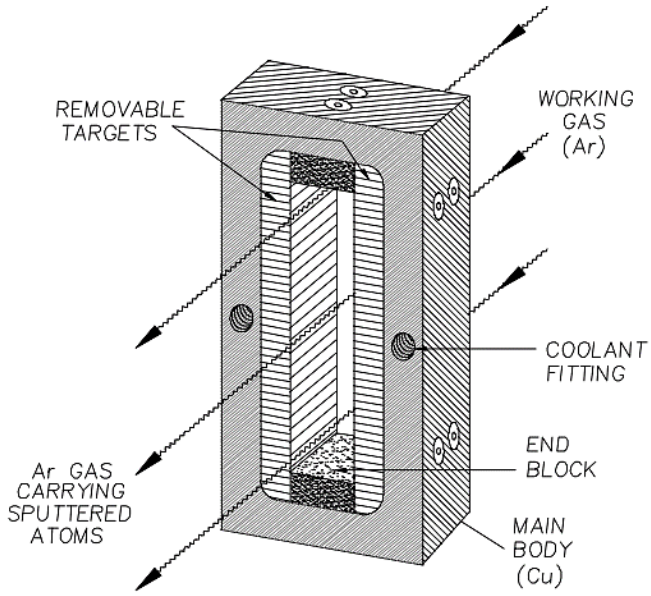

Figure 3.20 Basic Hollow Cathode Design for Linear Sputtering Source [25].

CHAPTER 4

THIN CONDUCTING OXIDES

4.1 Transparent Conductors

Transparent conductors are materials, which concurrently have the properties of optical transmission as well as electric conductivity. These properties are often realized through the use of a heavily doped, wide-bandgap semiconductor which is in most cases a metal oxide [26]. Other materials, like metal films (e.g. Ag), doped organic polymers, or metal nitrides (e.g. TiN) are also occasionally used as transparent conductors. For photovoltaic (PV) applications, oxides of transparent conductors are used. These so called transparent conducting oxides (TCOs) are in most cases based on the following oxides:

(i) Tin oxide,

(ii) Indium oxide,

(iii) Zinc oxide, or

(iv) Cadmium oxide.

Combinations of these materials, e.g. $ZnO\text{-}SnO_2$, have also been prepared and investigated [4]. In order to make further advancements in TCOs, ternary oxides are an effective alternative [27]. Ternary compounds such as indium tin oxide (ITO) and cadmium stannate (Cd_2SnO_4) have been implemented as a TCO in solar cells [4]. All the aforementioned materials are largely transparent in the visible portion of the spectrum of light. The reason for that lies in the fact that the photon energy E_{ph} (1.8 – 3.0 eV) is less than the bandgap E_g of the material (typically 3.2 – 3.8 eV) [4]. Hence, the photon cannot be absorbed. In general, oxides are highly insulating. However, the TCO is rendered conductive by free carriers resulting from the introduction of suitable impurity atoms, from

deviations of stoichiometry, or occasionally from other impurities. The commonly used TCOs are n-type, meaning that the free carriers are electrons. The resulting high free carrier concentration leads to a third property of a TCO: high infrared reflectivity.

Because a TCO must necessarily represent a compromise between electrical conductivity and optical transmittance, a careful balance between these properties is required. The reduction of resistivity involves either an increase in the carrier concentration or in the mobility. Increasing the former also leads to an increase in the visible absorption. The optical properties are improved by the achievement of a high carrier mobility [28].

The most excessively deployed TCO material is fluorine-doped tin oxide (SnO_2:F) which is used as a heat reflecting coating on architectural glass and as transparent electrode for thin film amorphous silicon (a-Si) as well as cadmium telluride (CdTe) based solar cells. Furthermore, tin-doped indium oxide (ITO), which is often implemented as a TCO, is used in flat-panel displays (FPD), high-definition TVs, touch screens, and certain types of solar cells based on crystalline Si wafers, a-Si, or copper indium gallium diselenide (CIGS). Zinc oxide (ZnO) is also more and more used in thin film silicon and CIGS PV technologies. For several of the above mentioned applications the transparent conducting oxide is deposited onto a flexible polymer sheet or a flexible coated metal foil.

Above all, there is a high demand for TCOs in a wide range of industrial applications. Consequently, enormous benefits stand to be gained from the development of lower cost and higher performance TCOs tailored to particular applications, especially solar cells.

4.2 Transparent Conducting Oxides for Photovoltaics

In the spectrum of photovoltaic applications most types of thin film solar cells require a TCO as the current-collecting electrode on the sun-facing side of the cell. The reason for that lies in the fact that the lateral conductivity of doped thin film semiconductors, which are sufficiently thin to possess high optical transmission, is too high for carrier collection over significant distances. Thin conducting oxides, however, are excellent candidates for a transparent front contact [29]. The TCO film permits the transmission of solar radiation directly to the active region with very little or no attenuation [6]. Moreover, the TCO film can perform simultaneously as a low resistance contact to the junction and as an antireflection coating for the active region of the solar cell [6]. Thin conducting films for PV applications should exhibit a resistivity of the order of 10^{-3} Ω cm or less and an average transmittance above 80 % in the visible range [30]. Therefore, TCO semiconductors should have a carrier concentration of the order of 10^{20} cm^{-3} or higher and a band-gap energy above approximately 3 eV [30].

The principal types of solar cells that use TCOs are schematically shown in Figure 4.1. Both amorphous-Si (a-Si) and CdTe superstrate thin film photovoltaic technologies typically use fluorine doped tin oxide SnO_2:F as the TCO. Next generation a-Si/nanocrystalline-Si (nc-Si) cells tend to use zinc oxide ZnO doped with either Aluminum (ZnO:Al) or Bohr (ZnO:B).[4]. The dye-sensitized TiO_2 type cells also use SnO_2:F, while organic cells have been fabricated on most major types of TCOs. Substrate-based technologies, e.g. a-Si on a polymer or steel foil, or CIGS on glass or metal foil, may use either ZnO:Al or ITO as the sun-facing TCO. [4]

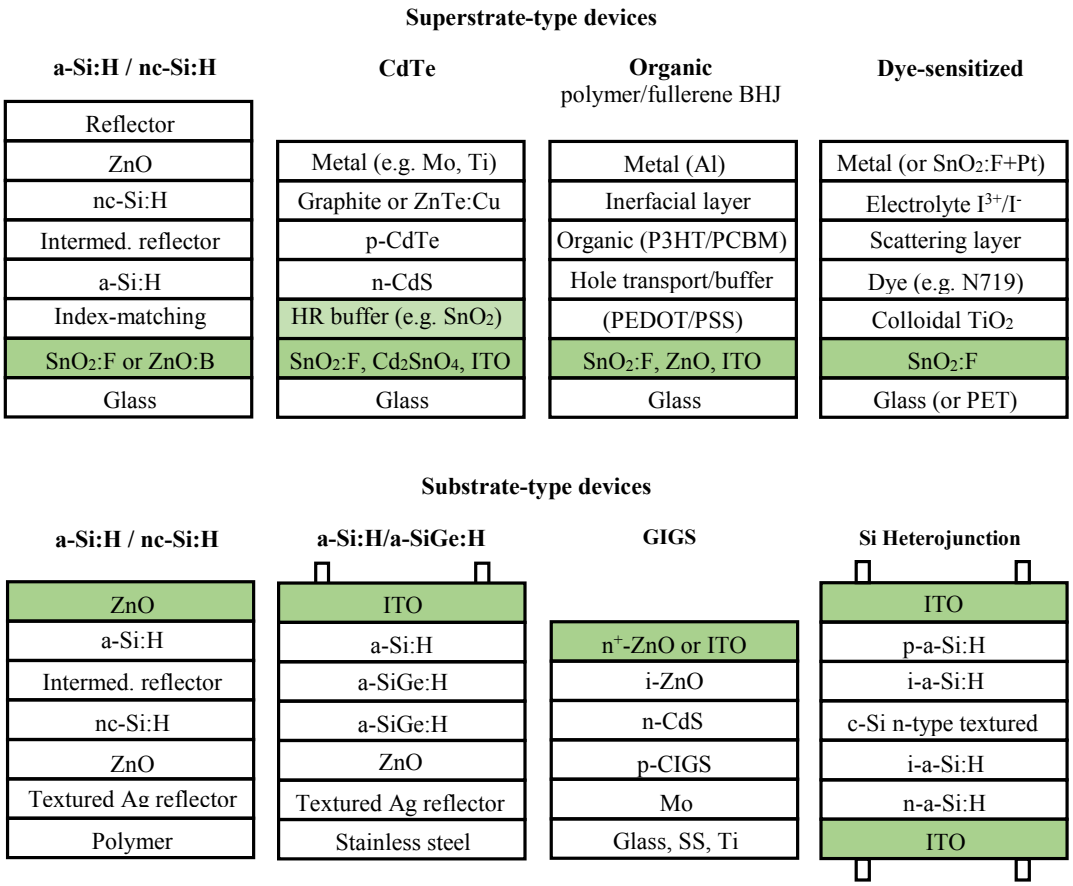

Figure 4.1 Principle Types of Solar Cells that Utilize TCOs (Adapted from [4]).

4.3 Classification and Important Types

Transparent conducting oxides can be made from material compounds which are binary or ternary compounds, as well as multicomponent oxides. The ternaries and quaternaries are formed through combinations of binary compounds. The TCO films used in commercial PV applications are made from binary compounds because these appear easier to control than ternary or multicomponent materials. One advantage is the relative ease of controlling the chemical composition in film deposition [30]. The relevant cations can be clustered as divalent (Cd^{2+} and Zn^{2+}), trivalent (Ga^{3+} and In^{3+}), and tetravalent (Sn^{4+}). Examples of these different types of TCOs are shown in Table 4.1.

Table 4.1 Examples for Binary, Ternary, and Quaternary TCOs [4]

Type of TCO	Example Compound
Binary	In_2O_3, SnO_2, CdO, TiO_2
Ternary (combination of binaries)	Cd_2SnO_4, $CdSnO_3$, Zn_2SnO_4, $CdIn_2O_4$, $Zn_2In_2O_5$, $MgIn_2O_4$, $In_4Sn_3O_{12}$
Quaternary (combination of ternaries)	$Zn_2In_2O_5$ – $MgIn_2O_4$, $ZnIn_2O_5$ – $In_4Sn_3O_{12}$, $GaInO_3$ – $In_4Sn_3O_{12}$, In_2O_3 – Ga_2O_3 - ZnO

An overview of the most important n-type TCOs is given in Table 4.12. This table also displays the deposition method and the doping elements used for these thin films, the resistivity range for doped films, and the bandgap of the undoped film. The bandgap of the doped film is generally higher, e.g. the bandgaps of doped CdO and ZnO are 3.1 and 3.7 eV, respectively, compared with 2.4 and 3.3 eV for the undoped film. Despite its very low resistivity, CdO is not utilized because of toxicity concerns. Cadmium Stannate (Cd_2SnO_4) can be prepared with low resistivity (1.3×10^{-4} Ω cm) by room temperate sputtering in O_2 of an oxide target followed by annealing at 580-700 °C to form a single spinal structure. The resistivity of zinc stannate (Zn_2SnO_4), regardless of whether it is polycrystalline or amorphous, is much higher because of a low carrier concentration [4]. To achieve TCO films with a low resistivity of the order of 10^{-5} Ω cm impurity doped binary compounds, e.g. Al doped ZnO, have to be utilized [30].

Table 4.2 TCOs Typically Used in PV Applications [4]

TCO	Common deposition method	Doping element	Resistivity range 10^{-4} [Ω cm]	Bandgap (undoped) [eV]
SnO_2	APCVD, spray pyrolysis	F, Sb, Cl	3 – 8	3.6
ZnO	Sputtering, PLD, LPCVD, APCVD	Al, Ga, B, In, F	1 – 8	3.3
In_2O_2	Sputtering, PLD	Sn, Mo, Ti, Nb, F	1 – 3	3.7
CdO	MOCVD	Sn, Mo, Ti, Nb, Zr	0.5 – 20	2.4
TiO_2	Sputtering, PLD	In, Sb	9 – 106	3.2
B-Ga_2O_3	Sputtering	Nb, N	200*–106	4.9
Cd_2SnO_4	Sputtering, sol-gel, spray pyrolysis	Si, Sn	1.2 – 10	3.1
Zn_2SnO_4	RF sputtering	self-doped	100 – 500	3.4
a-Zn_2SnO_4	RF sputtering	self-doped	30 – 60	---
a-$ZnSnO_3$	RF sputtering	self-doped	40 – 100	---
$Zn_2In_2O_5$	DC or RF sputtering	self-doped	2.9	2.9
a-IZO	DC sputtering	self-doped	3.0 – 5.0	3.1

* Achieved for bulk material, not thin film

Most high-quality TCO films (e.g. SnO_2:F, ZnO:Al, and high-temperature ITO) are polycrystalline. Besides polycrystalline structured TCOs, several amorphous TCO films have been prepared (see bottom of Table 4.1). Thus, ITO deposited at low temperatures, low temperature Zn_2SnO_4, and indium zinc oxide (IZO with zinc content of 10 – 42%) are all amorphous. The multicomponent TCOs are suitable for applications requiring reduced indium content and some of these have important emerging applications in the PV field.

Chapters 4.3.1 to 4.3.3 give an overview of the preparation and properties of the TCOs most commonly used in PV applications: ZnO, Cd_2SnO_4, SnO_2, and In_2O_3. However, the high cost and the scarcity of the element indium is a drawback for the recent expanding

market of PV and optoelectronic devices in general [31]. Regarding the constructed hollow cathode sputtering system, there is going to be a detailed analysis particularly for ZnO, ZnO:Al, Cd_2SnO_4, and SnO_2. A table of the important properties of those TCOs is portrayed in appendix B.1.

4.3.1 Zinc Oxide

Zinc oxide occurs in nature as a mineral zincite. Its crystal structure is the hexagonal wurtzite (B 4-type) lattice. Hereby, the zinc atoms are nearly in the position of hexagonal close packing. The crystal structure has a polar symmetry which is a consequence of the position of the oxygen atoms. Every oxygen atom lies within a tetrahedral group of four zinc atoms [32]. The wurtzite lattice structure of zinc oxide is illustrated in Figure 4.2. The large yellow circles symbolize the oxygen atoms and the zinc atoms are shown as smaller grey circles. The lattice constants are a= 3.24 Å and c=5.19 Å.

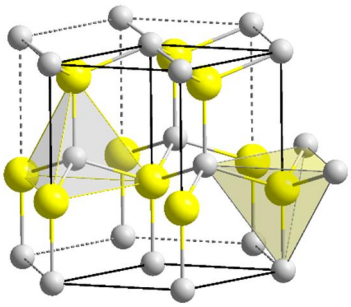

Figure 4.2 Wurtzite Crystal Structure of ZnO [33].

Zinc oxide is a II-VI n-type semiconductor with a direct and wide band gap. Its band gap at room temperature is E_g = 3.2 – 3.3 eV. It is available as a large bulk single crystal with a large excitation binding energy in the range of 60 meV [5, 11]. ZnO has been touted as a substrate for GaN epitaxial growth, because of an isomorphic structure and relatively close lattice match [36]. It attracts a lot of attention because of its large bandgap,

high conductivity, ease in doping, thermal stability when doped with group III elements, abundance in nature and non-toxicity [29]. In un-doped ZnO the n-type conductivity is due to deviations from stoichiometry. The free charge carriers are a result of shallow donor levels associated with oxygen vacancies, interstitial zinc, and hydrogen interstitials [37a, 40]. Even though interstitial oxygen and zinc deficiencies may also be present and produce acceptor states. Considering the long term electric properties, un-doped ZnO shows instability regardless of the deposition method. This is related to the change in surface conductance of ZnO films under oxygen chemisorption and desorption. In general, the electric properties of both un-doped and doped ZnO strongly depend on the deposition method, thermal treatment and oxygen chemisorption. It was found that increased film thickness and target conditioning were found to be the key factors in improving ZnO quality while oxygen is added [38].

A calculated band structure is shown if Figure 4.3.

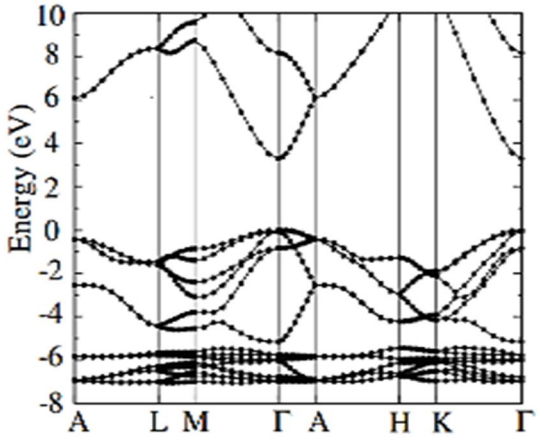

Figure 4.3 Calculated Band Structure of ZnO [34].

Band-gap adjustments, also referred to as band-gap engineering, can be achieved by alloying with magnesium oxide (MgO) or cadmium oxide (CdO). Adding Mg to ZnO causes the band gap to increase, whereas CdO decreases the band gap [34].

Controlling the conductivity of ZnO reflects a challenge. Even relatively small concentrations of native point defects and impurities (down to 10^{-14} cm^{-3} or 0.01 ppm) can significantly affect the electrical and optical properties [34]. Consequently, understanding the role of native point defects (i.e. vacancies, interstitials, and antisites) and the incorporation of impurities is key towards controlling the conductivity in ZnO [34].

The electric resistivity decreases with the increase of film thickness. A value of $8x10^{-4}$ Ωcm for a 1.5 μm thick film has been reported in [31].

Another crucial impact on the electrical properties of transparent conducting ZnO films is the oxygen partial pressure, a sputtering parameter. Depending on the two aforementioned parameters and substrate temperature, ZnO films can be categorized into three groups which reflect the general mechanism of film growth [39]:

(i) Opaque and conductive: mixture of metallic zinc and zinc oxide

(ii) Transparent and non-conductive: composition close to the stoichiometry to ZnO

(iii) Transparent and conductive: composition can be expressed as $Zn_{1+x}O$

An example graph is given in Figure 4.4.

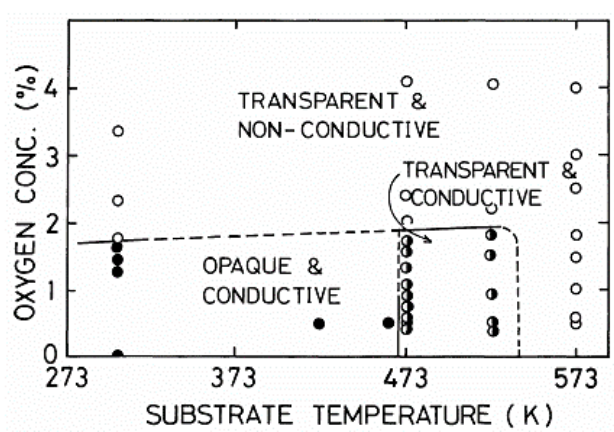

Figure 4.4 Effect of Oxygen Concentration and Substrate Temperature on Conductivity and Transparency of ZnO Films [39].

An additional substantial effect on the electrical properties is revealed by doping. Most often ZnO is doped with Al, but also gallium and indium doping is applied. On the whole, doping of ZnO films improves not only their electrical properties but likewise their stability. It was often shown that aluminum-doped ZnO films (short: AZO) have a high carrier concentration and a low mobility in comparison with those of undoped ZnO films. The higher carrier concentration in Al-doped ZnO is attributed to the contribution from Al^{3+} ions on substitutional sites of Zn^{2+} ions, and from interstitial aluminum in the ZnO lattice. The mobility of the charge carriers is strongly affected by scattering at the disorder locations. These disorder locations are created in the crystal structure due to doping [40]. Thus, well crystalline doped ZnO particles, pure in phase, are very important for obtaining good electrical conducting properties [40].

When preparing highly conductive and transparent impurity doped ZnO films, controlling the oxidation of Zn is much more difficult than with other binary compounds such as SnO_2 and In_2O_3. The reason for that is the higher chemical activity of zinc in an oxidizing atmosphere compared to Sn or In [30]. Because of the binding energy of Zn and O, the activity and amount of oxygen must be precisely controlled during the deposition process [30].

Non-stoichiometric ZnO films can be prepared by sputtering either by [6]:

(i) A metallic zinc target in the presence of an oxygen-argon atmosphere, or

(ii) An oxide target, usually in a gas mixture of hydrogen and argon.

Typical sputter conditions for growth of ZnO films using a zinc target are revealed in Table 4.3.

Table 4.3 Sputtering Parameters Utilizing a Zinc Target [6]

Sputtering parameter	Value
Sputtering power	100 W
Total pressure	$5x10^{-5}$ Torr
Oxygen concentration	0 – 29.4 %
Substrate temperature	300 – 600 K

The growth rate of reactively sputtered ZnO thin films depend significantly on oxygen concentration and deposition temperature. Figure 4.5 portrays the dependence of growth rate on oxygen concentration for different deposition temperatures. The figure reveals that the growth rate increases initially with the oxygen concentration. It reaches a plateau at 90 Å/min between 2 and 4 % oxygen concentration depending on the deposition temperature. This plateau could be the result of an oxygen flux on the substrate which is sufficient to oxidize all the arriving metallic atoms. The growth rate decreases drastically for higher oxygen concentrations. The reason for that is due to much higher oxidization of the metallic target compared to the sputter rate. In addition the figure shows that the growth rate decreases with the increase of substrate temperature. This is expected because the vapor pressure, which is quite high and also increases rapidly with increase of temperature, results in re-evaporation of zinc atoms from the substrate before being oxidized [6].

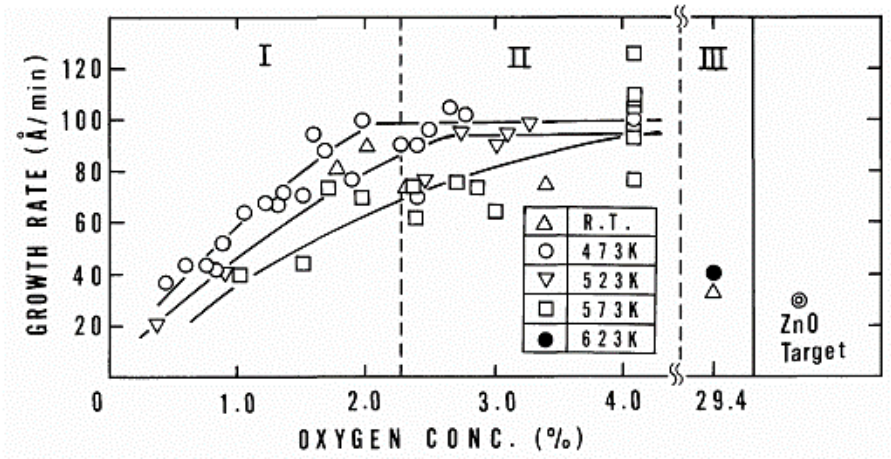

Figure 4.5 Growth Rate ZnO Depending of Substrate Temperature and Oxygen Concentration [39].

Table 4.4 assesses different sputter methods for the deposition of ZnO:Al. It can be observed that the hollow cathode process offers high film quality, a relatively high deposition rate, and a low resistivity [41]. Furthermore, the hollow cathode sputtering technique offers low target costs because metal is used instead of expensive ceramic targets.

Table 4.4 Comparison of Sputter Techniques for Deposition of ZnO:Al Thin Films [41]

Method	Sputtering Power [W]	Target	Substrate temp. [°C]	Deposition rate [Å s^{-1}]	Resistivity 10^{-4} Ωcm
RF Magnetron	600	Ceramic	Unheated	5.8	4.5
Pulsed Magnetron	2100	Ceramic	150	42.0	12.5
Hollow Cathode	900	Metal	90	67.0	5.7

In addition to table 4.4, table 4.5 reveals an example of boron-doped ZnO sputtered by reactive HCS. As a comparison, magnetron sputtered ZnO:Al is listed. It can be observed that the performance characteristics of the HC sputtered TCOs reach the good level of RF magnetron sputtered films.

Table 4.5 Doped ZnO Samples Deposited by HCS and by RF Magnetron Sputtering [42]

Sample	O_2 flow [sccm]	Thickness [μm]	Resistivity. [10^{-4} Ωcm]	Mobility [cm^2/Vs]	Carrier concentration 10^{-4} Ωcm
HCS (1, ZnO:B)	114	0.44	6.5	37.8	2.1
HCS (2, ZnO:B)	214	0.80	341	1.7	1.08
RF Magnetron	---	0.50	4.01	25.7	6.05

4.3.2 Tin Oxide

Tin oxide belongs to the group of so called soft oxides. There are several oxidation states. Most frequently used oxides are stannous oxide SnO and stannic oxide SnO_2. For TCOs only stannic oxides is considered [43].

SnO_2 has a tetragonal rutile structure. The unit cell contains six atoms: two tin atoms and four oxygen atoms [6]. Each tin atom (cation) is at the center of six oxygen atoms (anoins) placed approximately at the corners of a regular octahedron. The crystal structure is shown in Figure 4.6. Thereby, the larger red balls denote oxygen and the smaller blue balls indicate tin.

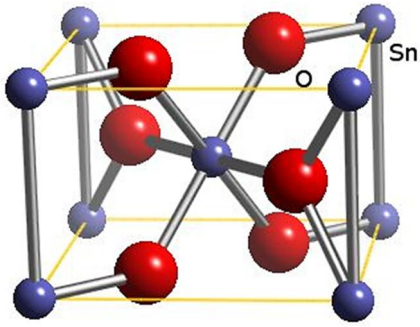

Figure 4.6 Crystal Structure of Tin Oxide [44].

In practical material tin oxide is never stoichiometric and is invariably anion deficient. The reason for that lays in the formation of oxygen vacancies in the otherwise perfect crystal. These vacancies make electrons available for the conduction process [44].

The electrical conduction in SnO_2 results from the existence of defects in the crystal structure, which may perform as donors or acceptors. The defects are either produced by the aforementioned oxygen vacancies, interstitial tin atoms, or other intentionally added impurities. The commonly applied method to make tin oxide a good conductor is doping.

The band structure of tin oxide is exposed in Figure 4.6. In addition, the band structure of antimony doped tin oxide (SnO_2:Sb) is illustrated. Antimony is next to fluorine to most excessively used dopant for tin oxide. Antimony doped tin oxide is often abbreviated with ATO.

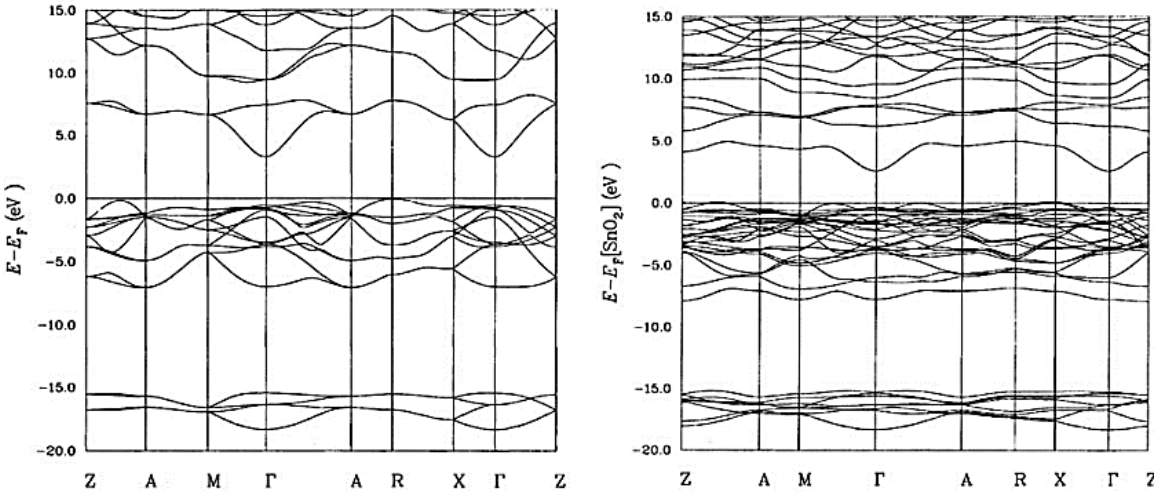

Figure 4.7 Band Structure Calculation for SnO_2 (left), and Sb Doped SnO_2 (right) [45].

The modification of the band structure due to impurity dopants was addressed for Sb doped SnO_2 [45]. In this case the impurity atom has one valence electron more than the cations of the host lattices. Thus, a donation of the extra electron into the conduction band

upon substitutional replacement of a cation by the impurity dopant may be expected. The direct band gap of SnO_2 has a value of 3.6 eV [45].

Antimony doped tin oxide can be deposited using either a Sn-Sb target or a SnO_2-Sb_2O_3 target. The quality of the thin films can be improved by post-deposition annealing of as-sputtered films [6]. Typical process parameters for the sputter deposition of Sb:SnO_2 and SnO_2 are shown in Table 4.6 and Table 4.7.

Table 4.6 Process Parameters for Depositing Sb:SnO_2 [6]

Sputtering parameter	Value
Applied DC-Voltage	3.6 kV
Discharge Current	0.4 – 0.5 mA/cm^2
Total pressure	40 – 80 mTorr
Oxygen concentration in the gas mixture	60 %
Substrate temperature	300 °C

Considering sputtering of undoped tin oxide there are two ways of achieving it [6]:

(i) Sputtering of a tin target

(ii) Sputtering of a tin oxide target.

Reactive sputtering of tin has been extensively used to grow good quality tin oxide films. Typically tin is sputtered in the presence of an oxygen-argon atmosphere. The oxidation level is strongly influenced by the sputtering rate and the ratio of oxygen to the total gas mixture. Films grown at lower substrate temperature (< 200 °C) are generally amorphous in nature and require post-deposition annealing, either in air or vacuum [6]. Typical process parameters for the sputtering of tin targets are shown in Table 4.7.

Table 4.7 Process Parameters for Sputtering of Tin Targets [6]

Sputtering parameter	Value
Applied DC-Voltage	1 – 2 kV
Discharge Current	10 – 40 mA
Distance between target and substrate	3 – 5 cm
Gas pressure	10-2 Torr
Oxygen concentration in the gas mixture	20 – 50 %

The argon-oxygen gas mixture ratio plays an important role in the formation on SnO_2 phase. Figure 4.8 illustrates the phase contents of tin oxide. The circle line denotes SnO_2, the X denotes SnO, and the triangle reflects Sn. For oxygen concentrations below 10 % both the α-SnO and β-Sn phases are also present in addition to the SnO_2 phase. The SnO_2 phase becomes more prominent when the oxygen concentration exceeds 10 %.

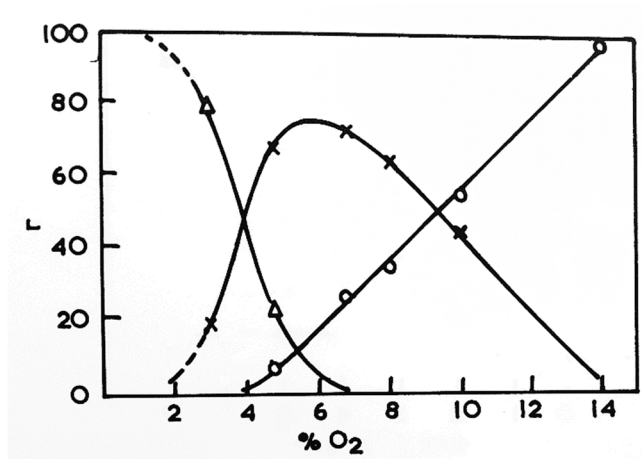

Figure 4.8 Phase Content of SnO_x Films Versus Oxygen Concentration [6].

In addition, the oxygen concentration has a great influence on the resistivity, the carrier mobility, and the carrier concentration. This aspect is revealed in the following diagram.

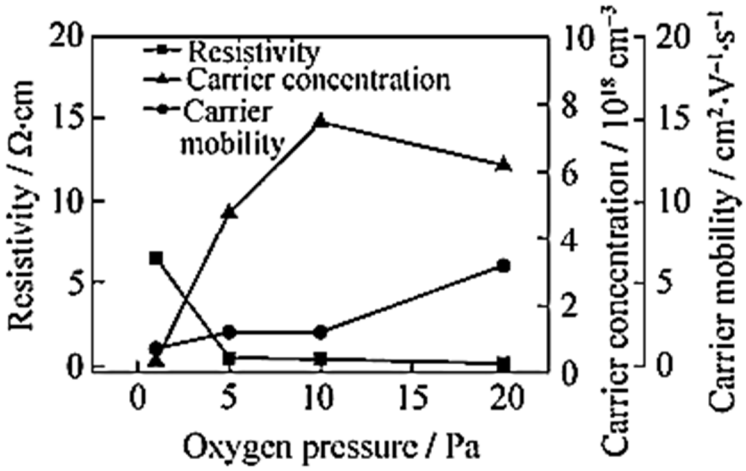

Figure 4.9 Resistivity, Carrier Concentration, and Carrier Mobility of SnO2 Thin Films as a Function of Oxygen Pressure [46].

It can be observed that with an increasing oxygen pressure the resistivity declines and carrier mobility as well as carrier concentration increase.

In a reactive sputtering process the voltage-current diagram is characterized by a transition from the so called oxide sputter mode to the metallic layers sputtering mode. The transition from oxide layers to metallic layers is indicated by a change in the discharge voltage which is shown in Figure 4.10.

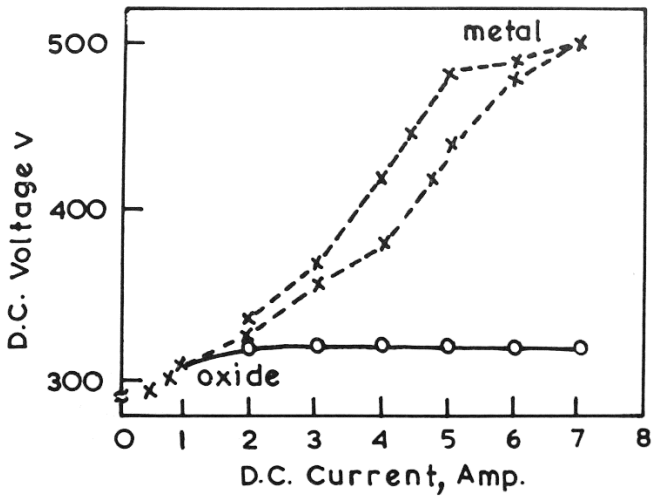

Figure 4.10 V-I Characteristic for Sputtering of SnO_2 [6].

SnO_2 films have also been deposited by sputtering a tin oxide target. However, the presence of oxygen is essential in order to have predominantly SnO_2 phase instead of SnO in these films [6].

4.3.3 Cadmium Stannate

Cadmium Stannate (Cd_2SnO_4) or Cadmium Tin Oxide (CTO) is an n- type semiconductor as most of the TCOs. There are two known phases of cadmium stannate, namely Cd_2SnO_4 and $CdSnO_3$. It is a ternary oxide consisting of Sn and Cd. The crystal structure of Cd_2SnO_4 is generally othomorhombic. However, $CdSnO_3$ can exist both in rhombohedral and orthorhombic structures. Since $CdSnO_3$ is not a transparent conductor only Cd_2SnO_4 is used as a TCO. It is the type of Sr_2PbO_4 (Pbam) with the unit cell dimensions a = 5.568 Å, b = 9.887 Å, and c = 3.192 Å [6]. Thermodynamically, Cd_2SnO_4 acquires a lower energy state when it crystallizes in the orthorhombic structure. Conversely, it was observed that sputtered cadmium stannate shows the inverse spinel structures [47]. "This phenomena makes this material a unique compound and not a mere mixture of cadmium oxide (CdO) and tin oxide (SnO_2)." [47] Thus, the ratio of Cd and Sn cations is very important for obtaining a homogeneous film without secondary phases such as CdO, SnO_2, or $CdSnO_3$ [47].

Figure 4.11 illustrates the cubic spinal structure of cadmium stannate. Each cubic face of either part is joined to the other part type, i.e. each part A is joined to six part B's at its cube's faces.

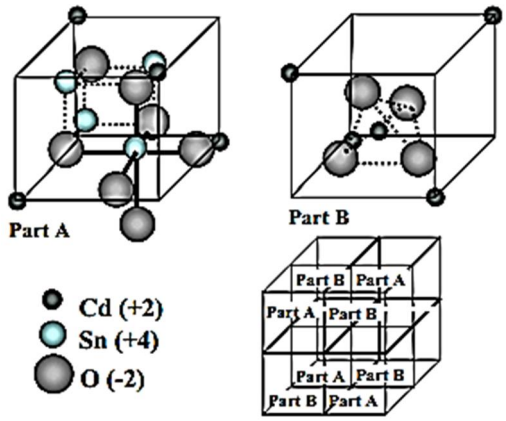

Figure 4.11 Cubic Spinel Structure of Cd_2SnO_4 [47].

Cadmium stannate in the spinel structure, as seen in Figure 4.11, has a large band gap of 2.64 eV [48]. Stoichiometric Cd_2SnO_4 can be achieved by As-crystal-growth process. These As-grown crystals, however, have a high resistivity. To obtain a conducting phase of Cd_2SnO_4 oxygen vacancies have to be implemented in the material. In case of sputtered Cd_2SnO_4 thin films, the oxygen partial pressure can be regulated to control the number of oxygen vacancies [6].

If grown at room temperature, cadmium stannate films are amorphous. Is the substrate temperature increased, the films are polycrystalline in nature. The minimum temperature at which the cadmium stannate film is polycrystalline depends not only on the substrate material but also on the composition of the sputtering gas. Films grown in a pure oxygen atmosphere crystallize at lower temperatures than films grown in an oxygen/argon mixture [18,.19].

Cd_2SnO_4 thin films can be deposited by using:

(i) Metallic alloy targets, or

(ii) Mixed oxide targets.

Cd_2SnO_4 can be prepared with a variety of deposition technologies, e.g. spray pyrolysis, co-precipitation method, dip coating, RF sputtering from metallic alloy targets (Sn and Cd), sputtering from ternary oxide targets, and co-sputtering from CdO and SnO_2 [27]. Among all the aforementioned deposition methods, sputtering is easily scalable to industrial production, with low cost and high reproducibility [27].

A problem which often occurs, when cadmium stannate is sputtered, are the phases of CdO and $CdSnO_3$. Single phase Cd_2SnO_4 films can be prepared only at high temperatures (400 °C) and by using 10% SnO_2-CdO target [6]. Furthermore, the sputtering time, bias and post-deposition annealing effect the composition and structure of Cd_2SnO_4 sputtered thin films. Using a DC reactive sputtering technique with Cd-Sn alloys has revealed several promising results [6]. Targets of various composition ranging from 50 % to 75% Cd-Sn have been used to deposit cadmium stannate. The texture and composition of CTO films strongly depend on the thickness, the deposition rate, and the target material.

Cadmium stannate has a high mobility of around 60 cm^2 which enable a low resistivity in the range of $2x10^{-4}$ Ω cm [49].

A general observation can be made in regards to the impact of the process gas argon. If the sputtering ambient composition is increased, the sputter rate increases and the resistivity decreases. This correlation is depicted in Figure 4.12.

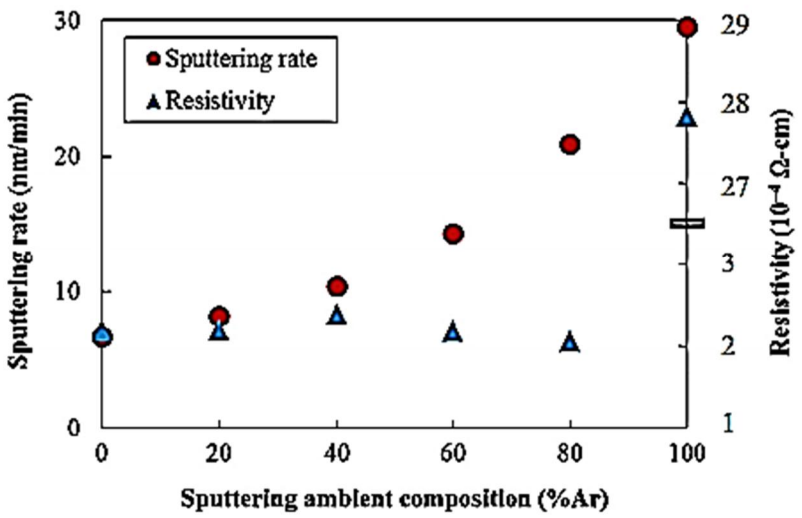

Figure 4.12. Sputtering Rate and Resistivity as a Function of the Ar O_2 Mixture [49].

In general, the structural, electrical, and optical properties reveal a particular sensitivity on the substrate temperature. The sputtering rate is strongly dependent on the substrate temperature as well. Figure 4.13 shows a comparison between CTO and ITO thin films.

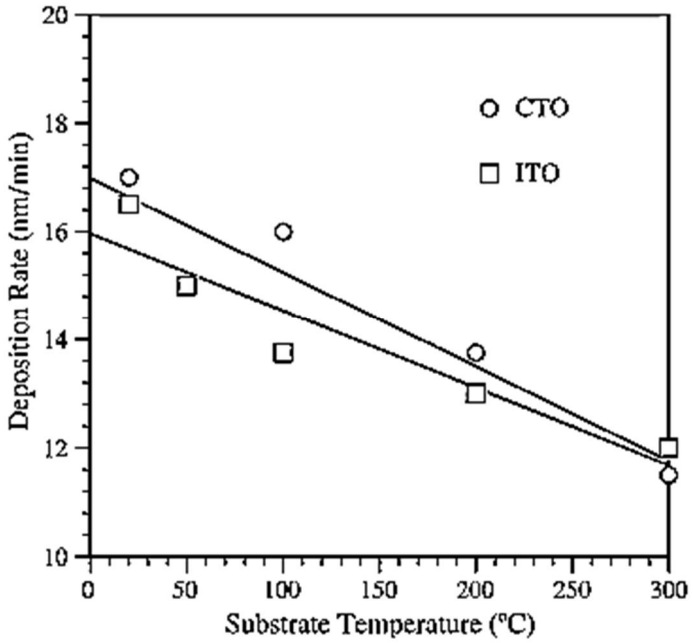

Figure 4.13 The Deposition Rate of CTO and ITO as a Function of Substrate Temperature [50].

Cd_2SnO_4 is one of the promising candidates for CdTe solar cell application, especially as a replacement for the cost intensive ITO. This is due to the following reasons:

(i) Lower surface roughness compared to SnO_2 thin films and more compatible with CdS to yield a smooth interface.

(ii) Better adhesion than SnO2 thin films and improved device performance at lower CdCl2 concentration treatment.

(iii) Reduced thickness of the Cd2SnO4 films in solar cell devices reduces the number of interconnections and hence, reduces manufacturing costs.

CHAPTER 5

HOLLOW CATHODE SPUTTERING SYSTEM

5.1 System Overview

A complete piping diagram of the hollow cathode sputtering system, which is viewed from the back, is illustrated in Figure 5.1. An explanation of all the components and their function is given in Table 5.2. The colored lines stand for the following connections:

- Black: vacuum line/connection
- Green: gas line (venting, purging, exhaust, compressed air)
- Blue: chilled water line
- Orange: control line (connection to controller)
- Red: Power connections, thermocouples

The vacuum chamber consists of three main openings which can be opened and closed via a gate valve (see Table 5.1).

Table 5.1 Gate Valves Used in the HCSS

Gate valve	Actuation	Vacuum line
Control Gate Valve (CGV)	Electric, operated by a controller (CGVC)	Main pump system (GXS line)
Vacuum Gate Valve (TPGV)	Pneumatic, operated by a panel	Turbomolcular pump (nEXT line)
Standard Gate Valve (LLGV)	Manual	Load lock, linear rack and pinion transporter (LL line)

The control gate valve (CGV) is electronically regulated by the CGV controller (CGVC). The controller for the CGV receives a pressure signal form the capacitance manometer (CM) which is mounted on the top of the chamber. The CGV is the gate valve

for the main pump line (GXS line). The main vacuum pump is a dry pump system from Edwards. The Vacuum Gate Valve (TPGV) is the gate valve for the turbomolecular pump (nEXT). This path is denoted with nEXT line. The TPGV is pneumatically operated and controlled by the TPGV control panel (TPGVC). The Standard Gate Valve (LLGV) is the gate valve for the load lock (LL). It is manually operated.

In Chapters 5.2 to 5.9 a meticulous description and analysis of every component of the HCSS is provided.

Table 5.2 HCSS Components and their Function

Abbreviation	Component	Function
CGV	Control Gate Valve	Gate valve for the main pump system
CM	Capacitance Manometer	Pressure measurement for CGVC
CGVC	Controller for CGV	Operation of the CGV with input from CM
GXS	Main pump system	Pump down the chamber
PDT	Pump Display Terminal	Readout for GXS status
ECV	Exhaust Check Valve	Check valve for the GXS exhaust line
SI	Silencer	Silencer for the GXS exhaust line
GFM	Gas Flow Meter	Flowmeter for nitrogen purge gas for GXS
WPG	Water Pressure Gauge	Pressure measurement of the water supply
WTM	Water Thermometer	Temperature measurement of the water supply
BV	Ball Valve	Valve for chilled water supply
WFM	Water Flow Meter	Measurement of water flow
BO	Blank-Off	Vent port and pressure gauge may be added later
PSSH	Power Supply Substrate Heater	Power supply for the substrate heater
LLGV	Load Lock Gate Valve	Gate valve for the load lock (substrate)
WRG	Wide Range Gauge	Pressure measurement in a wide range
LRP	Linear Rack and Pinion	Motion transporter for substrate

Abbreviation	Component	Function
LRP PS	Linear Rack and Pinion Power Supply	Power Supply for LRP stepper motor
PC	Personal Computer	Computer for the control of the LRP motor
TPGV	Turbo Pump Gate Valve	Gate valve for the turbo pump
SV	Solenoid Valve	Valve for compressed air
TPGV CP	Turbo Pump Gate Valve Control Panel	Control panel (switch and position indicators) for TPGV
nEXT	Turbo Pump	Pump down chamber and load lock
TVV	Turbo Vent Valve	Vent valve for turbo pump
AF	Air Filter	Filtering of the inlet air for the TVV
TIC	Turbo Instrument Controller	Controller for turbo pump and WRGs
AV	Angle Valve	Valve for roughing line (AV1) and for connection between TP and LL (AV2)
CG	Convection Gauge	Pressure measurement of the fore-vacuum
XDS	Backing Pump	Pump for the fore-vacuum of the TP
TMI	Temperature Measurement Interface	Control panel for temperature measurements
RPDG	Reactive Pulsed DC Generator	Power supply for the cathode
GR	Gas Regulator	Regulation of the outlet gas pressure of the gas cylinders
VV	Vent Valves	Valve for venting the chamber and LL
PV	Purge Valve	Valve for purging the GXS
V	Valve	Swagelok valve on the gas flow monitor panel
FC	Flow Controller	Gas flow controller for reactive and process gases
FCPS	Flow Controller Power Supply	Power supply and controller for FC

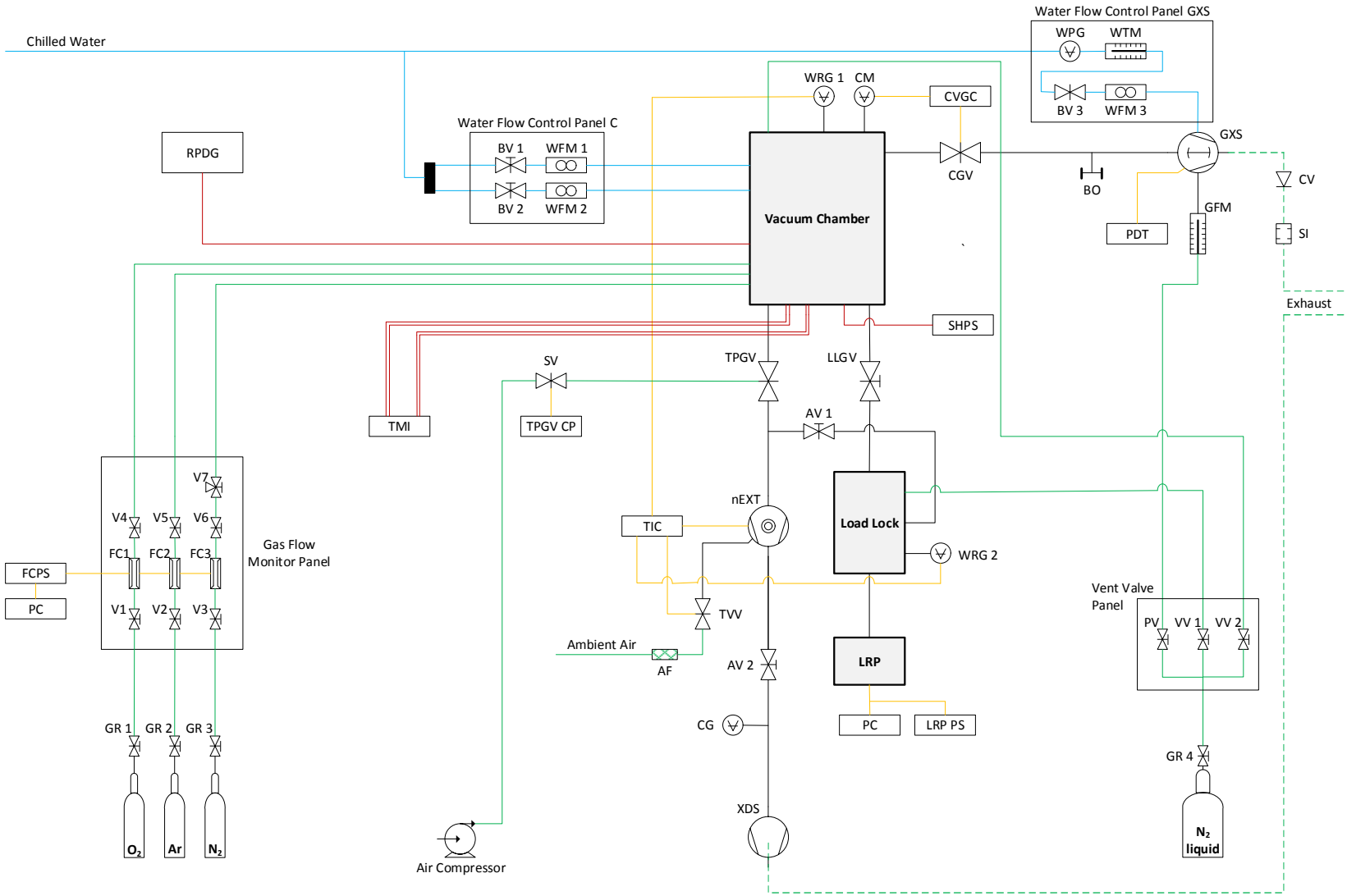

Figure 5.1 Piping Diagram of the HCSS (Back View).

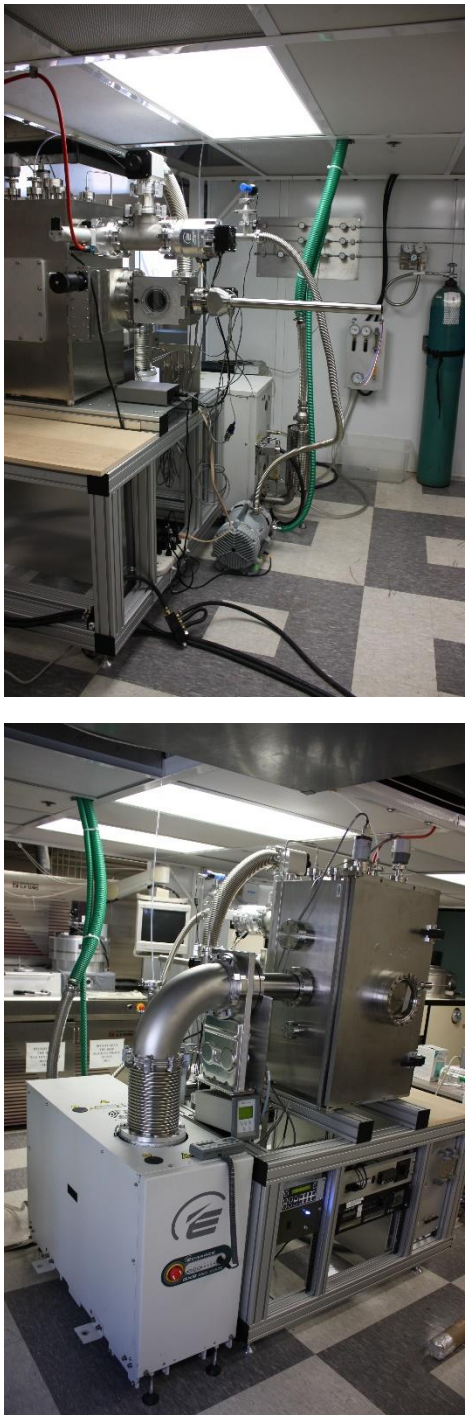

Figure 5.2 Photographs of the HCSS (Top: Back View, Bottom: Front View).

5.2 The Vacuum Chamber

5.2.1 Outer Connections

The vacuum chamber is a custom-built stainless steel vacuum vessel manufactured by Kurt L. Lesker. It is mounted onto a mobile frame. Aside from the gate valve openings, the chamber has numerous other orifices for different kind of feedthroughs, pressure gauges and other adapters. At the chamber itself are invariably ConFlat (CF) flanges used. Except the flange connection to the turbo pump is made with ISO system. All the other flange seals of the system also utilizes ISO or QF connections. The different types of vacuum flange connections, used for the HCSS, are shown in Figure 5.3.

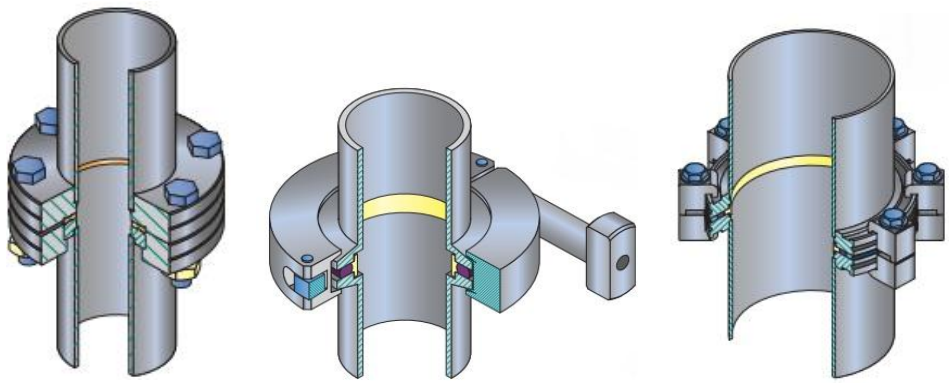

Figure 5.3 Vacuum Flange Systems Used in the HCSS [51].

The ISO standard quick release flange is known by the names Quick Flange (QF), Klein Flange (KF) or NW, sometimes also as DN. The sealant for this connection is a trapped o-ring. Connections are tightened by a clamp ring. Similar to the QF is the ISO flange. The design principles of QF and ISO seals are identical. For the ISO flanges usually C-clamps are used for attaining a tight connection. The CF seal works differently. The seal mechanism is a knife-edge that is machined below the flange's flat surface. As the bolts of

the flange-pair are tightened, the knife-edges make angular grooves on each side of a soft metal gasket, which are primarily made of copper. Thus, in contradiction to the o-rings of the ISO and QF connections, these gaskets are not reusable. The difference of the vacuum flange system is their field of application in regards to the pressure. The CF is suitable for an ultra-high vacuum up to 10^{-10} mTorr. ISO and QF flange systems are limited to about 10^{-5} mTorr.

All chamber orifices and their purpose are listed in Table 5.3.

Table 5.3 Orifices on the Vacuum Chamber and their Use

CF diameter [inches]	Amount	Connection to	Blank-offs planned for
1-1/4	2	Blank-off	Process measurements
2-3/4	11	Feedthroughs (thermocouple, power, chilled water) Pressure gauges Venting adapters Blank-off	Process measurements (temperature, pressure) Substrate motion
4-1/2	2	Blank off	Process measurements
6	1	CGV	
8	1	View port	
10	1	LLGV	

In addition to the flange seals, the chamber has a large opening for the cathode on the left right side. This is covered by a backing plate. Its dimensions are 10” x 6”. The backing plate is the basis for the cathode which will be mounted onto it.

5.2.2 Inner Setup

The inner setup of the chamber is depicted in Figure 5.4. This is a two dimensional front view. On the right side is the cathode located. The cathode is surrounded by a heat-shield. This heat-shield has a water supply and return hose fitted onto it. Attached to the cathode is a thermocouple. The substrate is mounted on the motion transporter of the LRP through a substrate holder. To monitor the substrate temperature, a thermocouple is anchored on to it. The substrate heater is mounted onto the holder behind the substrate (in the figure left). A copper line goes to it for the purpose of supplying power.

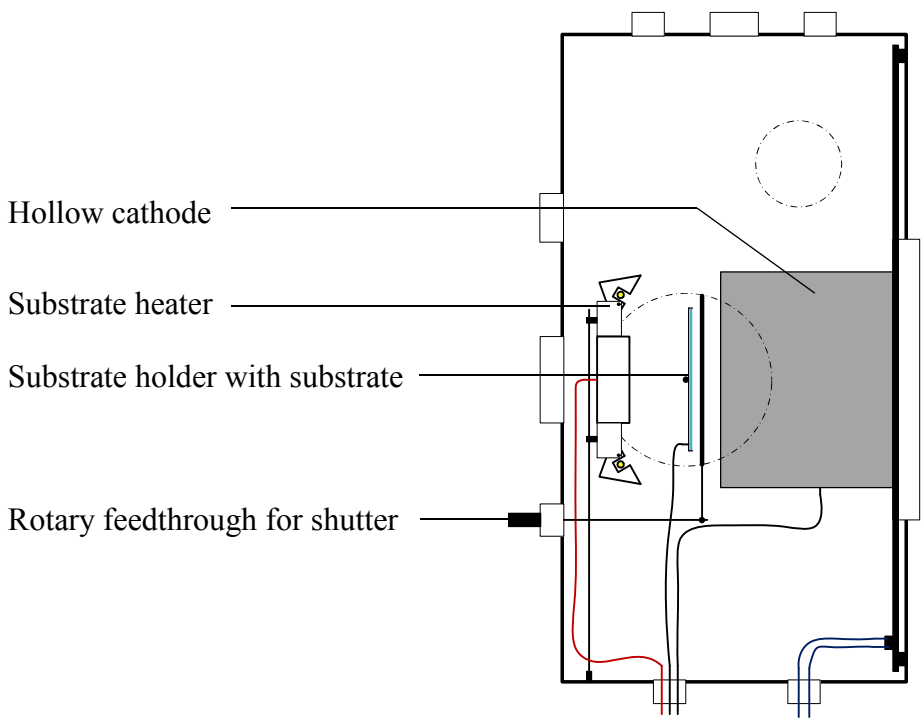

Figure 5.4 Schematic Front View of the Interior Components.

The dashed circles indicate the two orifices at the back, the one for the load lock behind where the substrate comes from, and the one for the turbo pump. The largest opening on the left side of the chamber is the flange for the connection of the GXS line. Thermocouple (black), power (red), and water (dark blue) feedthroughs are positioned at

the bottom of the chamber. The CM and a WRG are mounted on the two smaller flanges (2.75” CF) at the top of the chamber.

To monitor and control the water flow to the cathode and the heat-shield, a water flow control panel was design and installed on the right half-rack of the frame (see Figure 5.5). A thin aluminum sheet was installed on the frame to keep water separated from the electric applications.

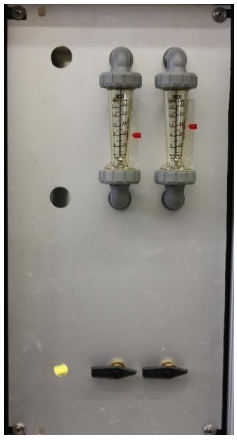

Figure 5.5 Water Flow Control Panel for Cathode and Heat Shield.

The substrate heater is a quartz lamp heater consisting of 4 single lamp assemblies (also called quadrate quartz lamp array). Each halogen lamp uses 500 W and produces 9,500 lumen. The lamps are mounted in an electropolished stainless steel V-reflector. They can reach a temperature of approximately 200°C with an average life of 2,000 hours. The heater array produces infrared radiation and ultraviolet light. Thus, they clean nearly all molecules adhering to the substrate’s surface through electron excitation and molecular vibration. The heater array is mounted on an L-shaped aluminum plate. This plate has a hole in the middle to maintain an undisturbed gas flow during the process.

Figure 5.6 enables a closer look at the cathode and substrate arrangement inside the chamber. The substrate is mounted on the substrate holder which is anchored on the rack

of the LRP. By controlling the LRP, it is possible to move the substrate totally out of the gas flow, and hence out of the deposition, area in both directions (left and right of the cathode orifice). The cathode shows the usual design of a hollow cathode which was already pointed out in Chapter 3.3. Argon flows through the orifice of the cathode towards the substrate. The GXS line flange is located directly behind the substrate and the substrate heater. Hence, after hitting the substrate, the process gas flows around the substrate to the GXS vacuum line.

The actual cathode design is different from the cathode depicted in Figure 5.6. It is a new and innovative cathode design developed by Professor Delahoy That is why it is not revealed in this thesis. As it can be observed in Figure 5.6, a deposition uniformity in the vertical direction cannot be guaranteed by using a static assembly. Consequently, the substrate moves back and forth during the deposition process. With a vertical substrate motion, a uniform deposition can be ensured on the whole substrate area which will be approximately 5” x 6”.

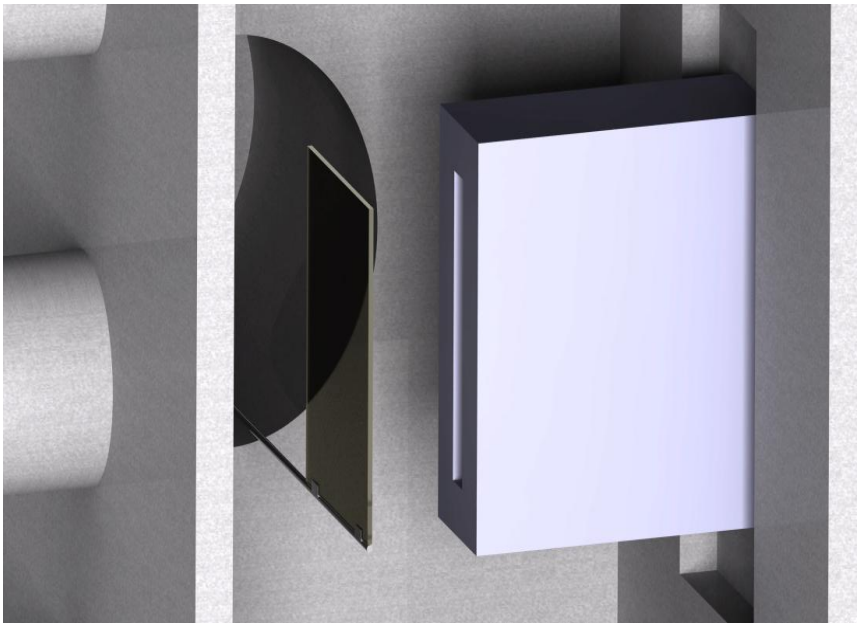

Figure 5.6 3D Sketch of the Cathode and Substrate Arrangement.

5.3 The GXS Vacuum Line

The GXS vacuum line consists of the GXS dry pump system, a flexible bellow hose, an elbow and a control gate valve (see Figure 5.7). It is used for the main evacuation of the chamber. Furthermore, the GXS line is necessary to achieve a high gas flow rate during the sputtering process.

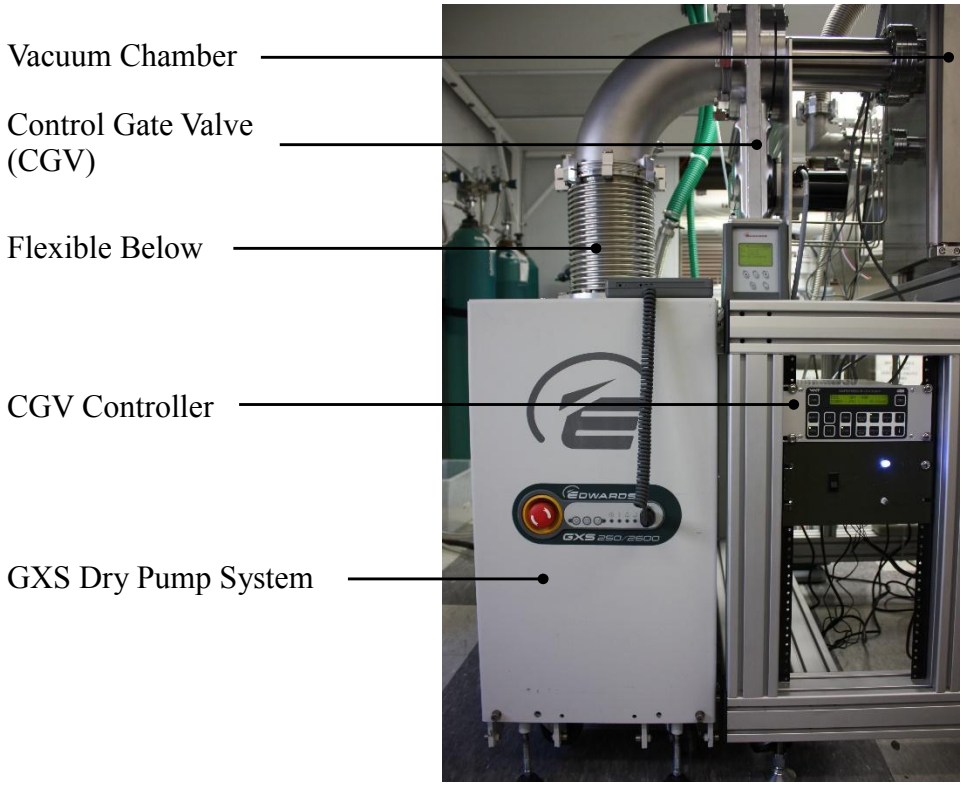

Figure 5.7 Photograph of the GXS Line.

5.3.1 The Main Pump System

The main pump system of the HCSS is the GXS 250/2600 dry pump system from Edwards. It is a light duty pump based on a screw-rotor design with an integrated booster. The performance characteristics are listed in Table 5.4 and a performance curve is depicted in Figure 5.8.

Table 5.4 Performance Characteristics of the GXS Dry Pump System [52]

Characteristic		Value
Peak pumping speed		1900 m^3h^{-1}
Ultimate pressure (with purge)		7.5 x 10^{-4} Torr
Power connection:		
	Voltage	460 V, 3ϕ
	Current	20 A
Full load power:		
	at ultimate pressure	5.3 kW
	at peak pumping load	9.7 kW
Cooling water:		
	Flowrate	min. 7 slm
	Supply pressure	max. 100 psig
	Differential pressure	min. 14.7 psig
	Temperature	5 – 40 °C
Purge gas (nitrogen):		
	Flowrate	12 slm
	Pressure	36 – 100 psig

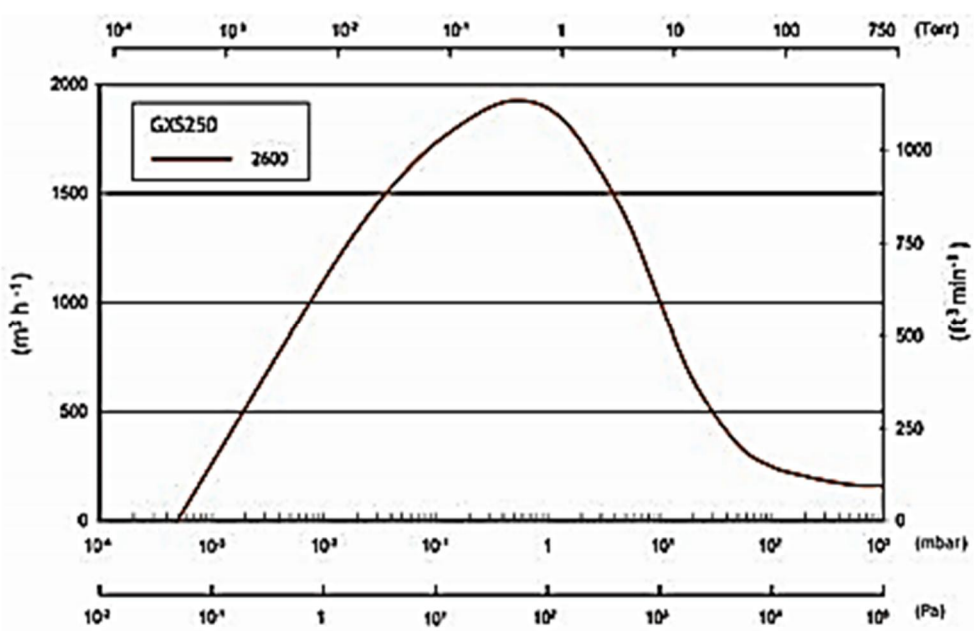

Figure 5.8 Performance Curve of the GXS [53].

The power supply connection is realized by a special Harting Han ® K 4/4 connector. The power cable is connected to a safe disconnect switch next to the pump. The pump is connected to the vacuum chamber via a control gate valve which is examined in Chapter 5.3.2 and visible in Figure 5.7. A custom-built water flow control panel is attached at the wall next to the GXS. It monitors the flow-rate, the inlet and outlet water pressure, as well as the water temperature (see Figure 5.9). Rubber hoses with an internal diameter of 1/2" are conducted from the water flow control panel to the GXS. Brass barbed hose fittings – with an outer hose diameter of 1/2" and a 3/8" NPTF female – are used for the inlet and outlet water hose connection on the back of the chamber.

Figure 5.9 GXS Water Flow Control Panel.

The purge gas is boiled-off liquid nitrogen which is also used a the venting gas (see Chapter 5.7). The purge connections are 1/4" Swagelok fittings. A stainless steel tube is leaded from the purge and venting panel to the purge inlet of the GXS. The dongle, observable in Figure 5.10, needs to be plugged in order to operate the pump. Inside this dongle is a jumper wire installed. The jumper wire can be connected to a remote emergency

stop button. In addition, the whole exhaust line can be examined in Figure 5.10. The exhaust line of the GXS consists of a check valve, an elbow, a silencer, a braided flexible stainless steel hose, and a PVC hose which is connected to the main exhaust line of the laboratory. The iXH check valve from Edwards prevents rapid suck back of exhaust duct vapors after the pump is shut down. Moreover, it provides additional attenuation of the exhaust gas pulsation.

Figure 5.10 GXS Back View.

The GXS dry pump system is equipped with a Pump Terminal Display (PTD). The PDT connect to the front of the GXS, and it serves as a remote monitor and control unit (see Figure 5.11).

The following status reporting functions are possible with the PDT [52]:

(i) Started and stop of the GXS

(ii) Monitoring of process temperatures of cooling water, dry pump (DP), motor booster (MB), inverters of DP and MB in °C

(iii) Monitoring of the consumed power of DP and MP in W

(iv) Monitoring of the drawn current of DP and MP in A

(v) Monitoring speed of DP and MP in Hz (and %)

(vi) Monitoring the exhaust pressure (in psi) and temperature (in °C)

(vii) Monitoring of the cooling water flowrate (in l/min)

(viii) Recording of the operating hours

(ix) Number of pump starts

Moreover, the PDT indicates warnings and alarms.

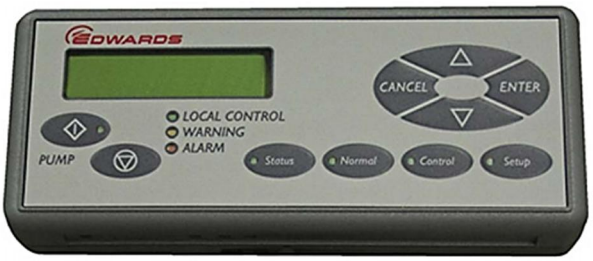

Figure 5.11 Pump Terminal Display (PDT) [52].

If the PDT is connected to the GXS and has control over the GXS, the green LOCAL CONTROL LED is illuminated. In that case the status of the pump shows that PDT is in control. To release control from the PDT, the CONTROL button needs to be pressed. The GXS can also be operated by using the front panel of the GXS (shown in Figure 5.12). In order to take, as well as release control over the GXS through the front panel, the LOCAL CONTROL button needs to be pressed.

Item	Control/connector identification
1	EMS button
2	Running LED (green)
3	Start button
4	Stop button
5	Local control button
6	Local control LED (green)
7	Power LED (green)
8	Warning LED (yellow)
9	Alarm LED (red)
10	Green Mode LED (green)
11	PDT (Pump Display Terminal) connection

Figure 5.12 GXS Front Panel Controls [52].

The PUMP LED at the PDT illuminates with pressing the pump start button and it indicates that the GXS is running. This LED is continuously on when the pump is on-process and it flashes when the pump is warming up, stopping, or when it is in Green Mode/Standby Mode. If a pump warning occurs, the WARNING LED illuminates yellow. It flashes when a new warning happens until it is acknowledged by pressing ENTER. Then it goes continuous until the warning is cleared. The WARNING LED also flashes when a new event is present. Once the event has been acknowledged the warning LED will return to its previous state. The ALARM lights up to indicate that a pump alarm is present. It flashes when a new alarm occurs until it is acknowledged by pressing ENTER. Then is goes continuous until the alarm is cleared.

For the exactly adjusted operation the PTD offers a wide range of setting options. The comprehensive menu structure and the corresponding functions are enumerated in Table 5.5. A flow chart of the complete PTD menu structure is illustrated in appendix A.3. The access code to enter the command menu is 202.

Table 5.5 Menu Structure of the PID [52]

Menu	Function
Command	Open/Shut, ON/OFF: inlet isolation and gas valves, MB pump, PID, PID Autotune, Green or Test Mode, DP Clean
Gas Valves	Set N_2 seal, gas ballast, or inlet
Set Sequence	Options for warm-up, booster start, Micro TIM, DP clean, Ramp speed up on-process, PID pressure control setup, smart shutdown, speed control Reset Micro TIM Restore factory default settings

The operation sequence of the GXS vacuum line is explained in Chapter 5.3.3.

5.3.2 Control Gate Valve

The Control Gate Valve (CGV) is, as mentioned in Chapter 5.3.1, the gate valve of the GXS vacuum line. The sealing technology is based on the VATLOCK system. The gate is actuated by a stepper motor from Nanotech Munich. It takes five seconds to fully open or fully close the CGV.

To operate the CGV, an adaptive pressure controller (CGVC) is connected to it. This controller is a PM5 from VAT. The CGVC offers a local mode (operation directly at the controller panel) and a remote mode (serial connection to a computer). The local mode is used for the HCSS. The CGV can be operated by using the OPEN and CLOSE button at the CGVC. Furthermore, it can be operated by using the pressure mode control. The pressure mode is applied when a certain pressure has to be held constant in the chamber. In that case, the CGVC adjusts the position automatically. The CGVC gets its pressure input signal from a capacitance manometer (CM) which is mounted on top of the chamber. This pressure gauge is a MKS Baratron ® Type 626B. It has a full scale range of the order

of 1 Torr which leads to a pressure range of 1 – $5x10^{-4}$ Torr. The pressures for reading and control are elucidated in Table 5.6.

Table 5.6 Reading and Control Pressure for the CM

Lowest Suggested Pressure	
For Reading [Torr]	For Control [Torr]
5×10^{-4}	5×10^{-3}

The CGVC displays the actual chamber pressure, if it is in the range of the CM, at every time. The full configuration sequence of the CGVC is shown in appendix A.2.

Figure 5.13 CGV Controller.

The CGVC can work either in POSITION MODE or PRESSURE MODE. In the POSITION MODE four setpoints can be selected. The default settings are shown in Table 5.7. The position number indicates where that the valve is between OPEN (=1000) and CLOSED (=000).

Table 5.7 CVGC Setpoints and Corresponding Valve Position

Setpoint	Valve Postion
1	200
2	400
3	600
4	800

In the PRESSURE MODE the CGVC adjusts the position of the valve so that a certain pressure is maintained. This mode is predominantly used for the operation of the HCSS.

5.3.3 Operation Sequence of the GXS Vacuum Line

The start sequence for the GXS for pumping down the chamber is a elaborated in the following section.

1. Switch on the external electric power supply and check the power LED.
2. Switch on the cooling-water and purge gas supplies.
3. Ensure that all openings to atmospheric pressure in the fore-line vacuum system are closed.
    a. Close LLGV.
    b. Close TPGV.
4. Turn on the CGV controller and put it to position 1 (or fully open it).
5. Press and hold the local control button and check that the green local control LED comes on and then remains continuously illuminated.
6. Turn on the TIC to read out the pressure of WRG 1.
7. Press the Start button.

8. If the system starts and continues to operate, go to the next step. If a warning or alarm condition is indicated (LED signal): Shut down the pump.
9. Look at the pressure gauges in the chamber:
    a. WRG 1 (connected to TIC).
    b. CM (connected to CGV controller).
10. If pressure increases, immediately shut down the system.
11. Visually check the purge gas flowmeter on the rear of the pump to ensure purge gas is being delivered to the pump.
12. Visually check the flow rate and temperature of the cooling water.
13. Open the CGV fully by pressing the *OPEN* button on the CGV controller.

There are two stop sequences recommended by Edwards: Auto Shut-down and Smart Stop. In Auto Shut-down mode, a purge gas cycle is introduced and the pump shuts down gradually over a time period of 15 minutes. This is the default mode on the GXS. Smart Stop allows the user to define the time period for the gradual shut down and to configure a setpoint temperature. If Smart Stop is enabled, the pump will perform a Smart Stop when the Auto Shut-down mode is selected. The Fast Shut-down mode is an additional option for a quick stop of the pump without purging. It is not recommended to use this stop sequence [52]. The stop sequence for the GXS is:

1. Close CGV by pressing the CLOSE button on CVG controller.
2. Press the STOP button on the PDT. Confirm with ENTER the AUTO STOP or FAST STOP mode.

5.4 The nEXT Vacuum Line

The nEXT vacuum line consists of the vacuum gate valve (TPGV) and the turbomolucular pump from Edwards (illustrated in Figure 5.14). Moreover, there is a vacuum line to the load lock which can be opened by the angle valve (AV 1). This section provides a comprehensive description of the operation of the turbo pump and its secondary equipment.

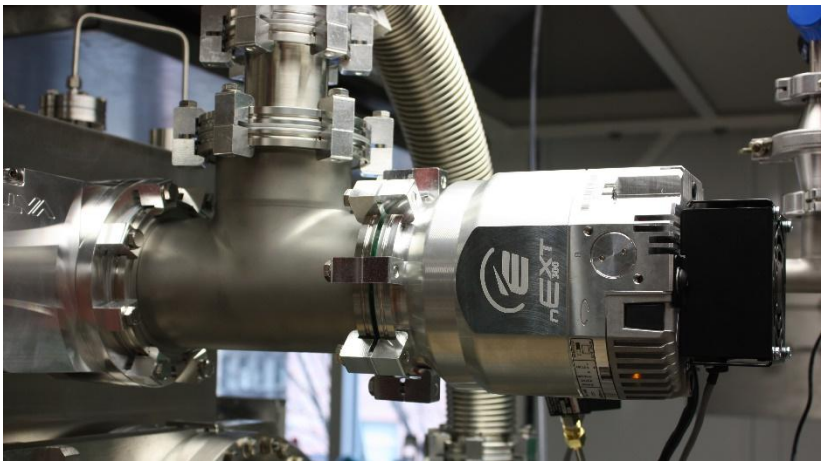

Figure 5.14 nEXT Vacuum Line.

5.4.1 Turbomolecular Pump

The turbomolecular pump, short turbo pump, is a nEXT 300 D from Edwards. It is equipped with an axial cooling fan and a TAV5 vent valve. The nEXT, the fan, and the vent valve are connected to the Turbo Instrument Controller (TIC). The connection of the logic interface adapter (seen in Figure 5.18), which is a 24 d-sub connector, is from eminent importance. This adapter has, similar to the dongle of the GXS, a jumper wire inside. Without the adapter plugged in the TIC, the TIC does not transmit any commands and hence, the nEXT will not turn on.

The performance characteristics of the nEXT are shown below and the performance curve is depicted in Figure 5.15. This curve illustrates the pumping speed depending on the inlet pressure for four different gases.

The nEXT is provided with controller status information on the bottom. As seen in Figure 5.16, it includes a standby speed increase button (1), a RS484/RS232 switch (2), a controller connector socket (3), a standby speed reduce button (4), an alarm LED (5), a status LED (6), and a normal running LED (7). The serial connection switch is turned to the right side for RS232 enabling. The nEXT is connected to the TIC through a RS232 cable.

Table 5.8 Performance Parameter of the nEXT 300D [54]

Parameter		Value
Power limits		
	Standard default setting	160 W
	Max. value setting	200 W
	Min. value setting	50 W
Inlet pumping speed		300 l/s
Interstage pumping speed		13 l/s
Ultimate pressure		4.5 x 10^{-5} mTorr

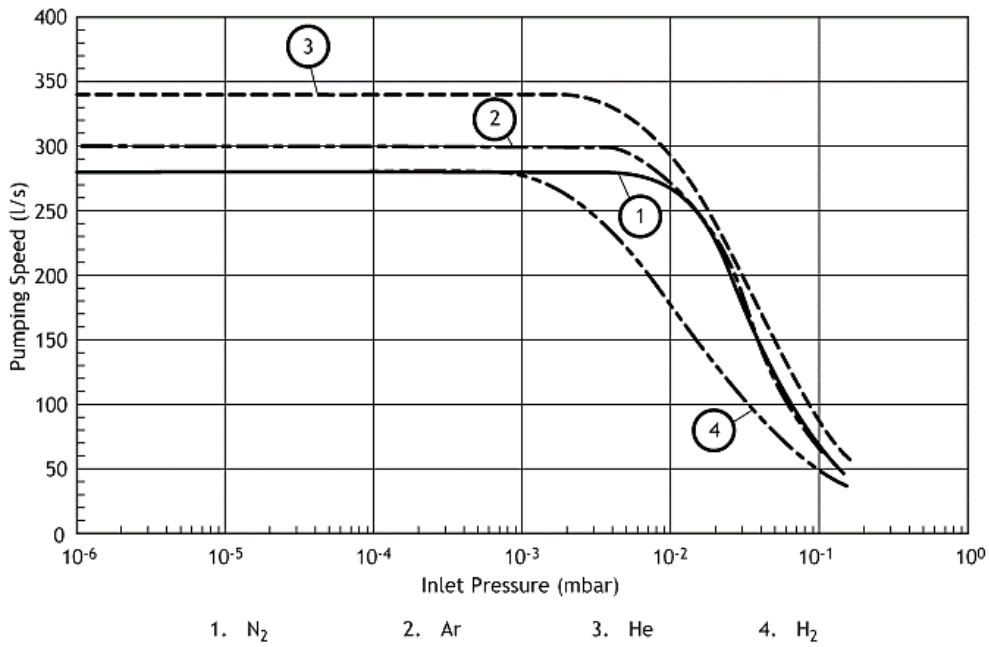

Figure 5.15 nEXT Performance Curve [54].

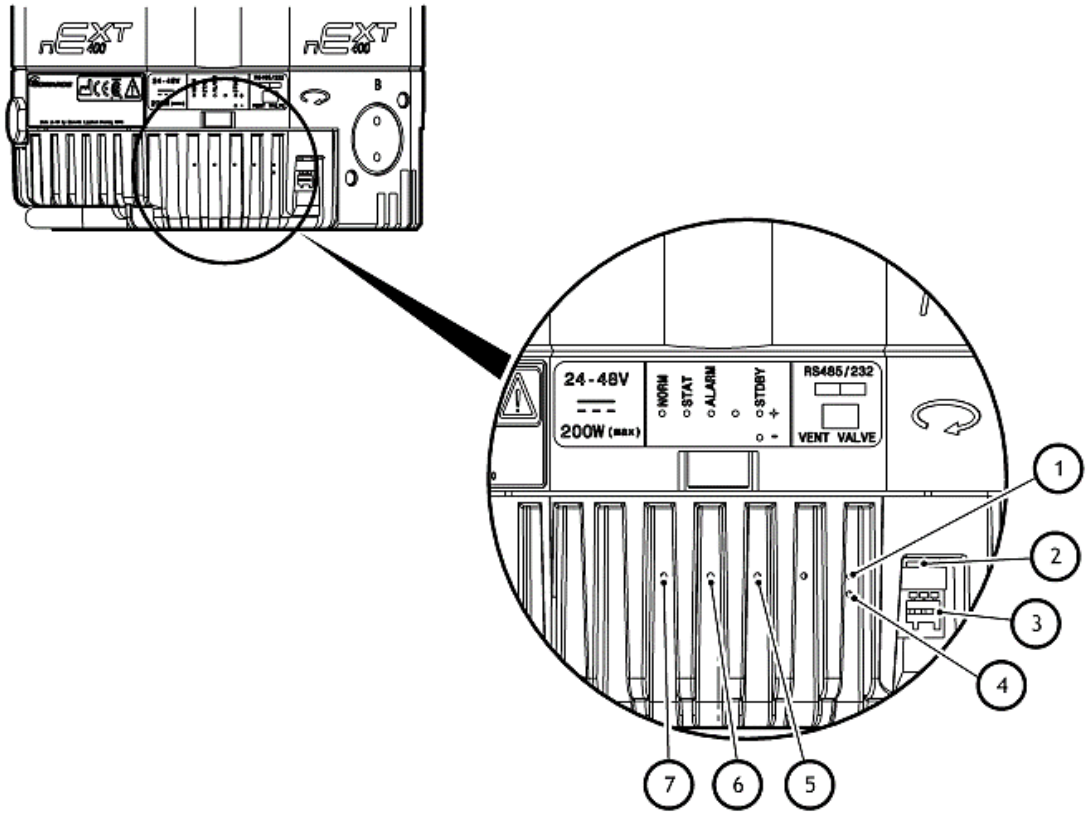

Figure 5.16 Controller Status Information [54].

The TIC (see Figure 5.17) monitors and controls the nEXT operation. In addition, it also supplies the voltage (24 V) to the turbo pump. The nEXT is configured using the TIC. It is possible to set the following parameters of the nEXT:

(i) Power limit

(ii) Controlled venting

(iii) Standby speed setting

(iv) Normal speed setting

(v) Timer setting

(vi) Electronic braking options

(vii) Factory default settings.

The setup options are enumerated in the Table 5.9.

Figure 5.17 TIC Front View.

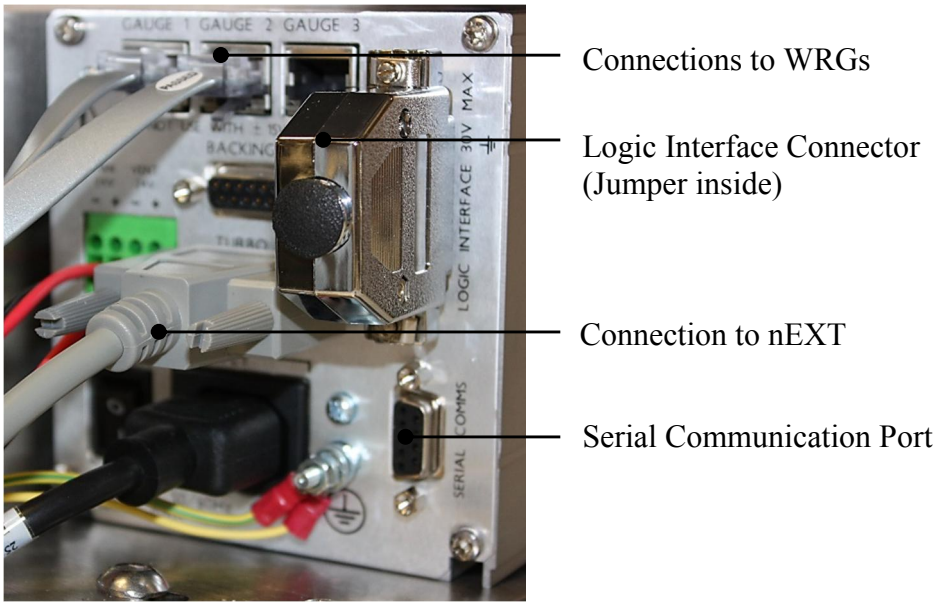

Figure 5.18 TIC Back View.

Table 5.9 TIC Setup Options

Menu option	Description
Ramp up timer	Set the ramp up timer from 1 to 8 minutes. This timer generates an alarm if the pump speed does not rise above 50 % speed after the set time.
Droop timer	Set the droop time from 1 to 8 minutes. This timer generates an alarm if the pump speed drops below 50 % speed for longer than the specified time.
Heater time	Set the time that the heater band bakes out the nEXT from 0 to 35 hours. The heater will come on for the set time, once the pump reaches normal speed. If the pump drops below normal speed, the heater band will switch off and the timer will be reset.
Start delay	Delay of the start of the nEXT from 0 to 99 minutes
System ON	Determination of the components of the system that are to be turned on, when the system is cycled on
System OFF	Determination of the components of the system that are to be turned off, when the system is cycled off
Air cooler	Setting when air cooler should operate. The air cooler can be set ON (on permanently) or TURBO (on when nEXT is running)
Vent options	The TAV5 can be operated in two ways: ON STOP to open the vent valve 2 seconds after the stop command, or “50 %” to open the vent valve when the pump slows to 50% speed.
Backing pump options	NONE: The backing pump is not sequenced to the nEXT. 50 %: The backing pump will turn off after 2 seconds, once the nEXT speed has dropped to 50 % of its full speed. The delay allows detritus to be removed from the system on stop. ON STOP: The backing pump will turn off 4 seconds after the nEXT off command has been sent. The 4 second delay allows shutting off a valve and then removal of detritus form the system.

The TAV5 solenoid vent valve is operated by the TIC. It opens when the rotational speed of the nEXT falls under 50 % of the full rotational speed. When a turbopump is switched off, the rotor comes to a stillstand and contamination on the fore-vacuum side - in other words condensation - seeps back into the vacuum vessel and contaminates walls

and objects. This contamination in the vacuum chamber is practically excluded by admitting dry gas into the turbopump due to the slower rate of diffusion. There is a two second delay between either a stop command being received, or a fault condition being detected, and the vent valve opening. This delay allows time for gauges, valves, and other equipment to be switched off before venting occurs.

The STATUS menu is a powerful tool to monitor and control the operation of the nEXT. It displays the current status of the nEXT and provides information about:

- Whether the pump is ON/OFF
- The state of the pump (RUN/STB)
- The power that the pump is using.
- The speed of the pump in percentage of the full speed.
- The temperature of the power supply, the turbo drive, and the turbo pump.
- Whether the vent valve is ON/OFF

In addition to the nEXT control, the TIC serves as a readout for the two wide range gauges (WRG) used in the HCSS. WRG 1 is mounted on the top of the chamber and the other one on the load lock (denoted with CHAM and LL in the TIC). The WRG is a combined inverted magnetron and pirani gauge in a single compact unit. Its pressure range is 75 – 10^{-10} Torr. In the range above 75 Torr to about 750 Torr the WGR measures with a reduced accuracy. It was adjusted to atmosphere by going through the subsequent steps:

(i) Use the ATM switch on the back of the WRG to set the reading at atmosphere.

(ii) Switch on the power supply to the WRG and allow it to operate at atmospheric pressure for at least 10 minutes.

(iii) With the vacuum system at atmospheric pressure, press the "ATM" switch with an appropriate tool. The output of the gauge will be automatically adjusted to read atmosphere.

The WRG will perform the pirani sensor vacuum setting automatically every time the WRG is pumped down to a pressure lower than 7.5 – 3 Torr. Therefore, a manual setting of vacuum is not compulsory unless the pirani tube is replaced. If the gauge fails to indicate pressure of < 7.5 Torr, then a manual vacuum setting is required. To perform this operation, follow the procedure below:

(i) Reduce the system pressure to 10-5 mbar or below.

(ii) Wait for 1 minute.

(iii) Press and release the "ATM" switch.

(iv) Wait for approximately 30 seconds until the adjustment is completed.

Manual adjustment of the vacuum reading is recommended when replacing the pirani tube or after a long period of storage.

5.4.2 Backing line

In order to achieve the necessary exhaust pressure for the nEXT, a backing pump is installed. The backing pump is used to create the necessary fore-vacuum for the nEXT. The backing line comprises a manual angle valve (AV 2) from VAT, a convection gauge from Kurt J. Lesker, and a dry pump from Edwards. The backing pump is a XDS 10 (XDS) from Edwards (Figure 5.19).

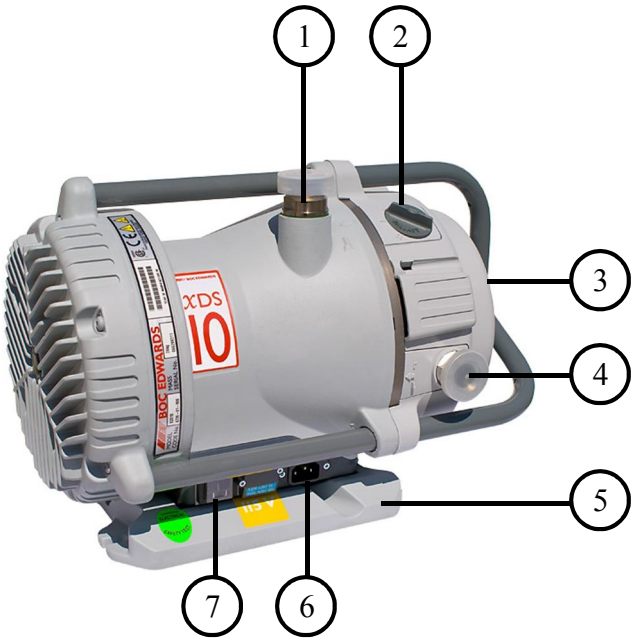

1. NW25 inlet port
2. Gas-ballast control
3. Cooling fan
4. NW25 exhaust port
5. Baseplate
6. Voltage indicator
7. On/Off switch

Figure 5.19 XDS 10 Dry Pump [55].

The XDS is a dry vacuum scroll pump. The pump mechanism is driven by a single-phase electric motor. The body of the pump includes a fixed scroll and an orbiting scroll which is driven by the electric motor through an eccentric cam on the motor drive shaft. The movement of the orbiting scroll, meshed with the fixed scroll, forms successive crescent shaped volumes in the pump. Gas which enters the pump through the inlet is compressed by the movement of the orbiting scroll and swept towards the center of the fixed scroll. The compressed gas enters the exhaust port near the center of the stationary scroll and is exhausted from the pump through the outlet. At the exhaust outlet port of the XDS a PVC hose is connected which leads the exhaust gas to the main exhaust line of the laboratory. The pump is air cooled through an integrated fan.

To pump high vapor loads, gas ballast is delivered to prevent condensation of the pumped gas. Air can be introduced to the low vacuum stages through the gas-ballast valve. The three positions of the gas-ballast control valve are shown in Table 5.10. The gas ballast control valve lets air into the roughing (backing) line.

Table 5.10 Positions of the Gas-Ballast Control Valve [55]

Position	Name	Description
0	Closed	To achieve ultimate vacuum To pump dry gases
1	Low flow	To pump condensable vapors To dilute process gases if required
2	High flow	To pump high concentrations of condensable vapors To dilute process gases if required To clear excess vapors after processing.

Position 1 is the normal operating position for the HCSS. The XDS can achieve an ultimate pressure of 45 mTorr. The performance characteristic of the XDS 10 is illustrated in Figure 5.20.

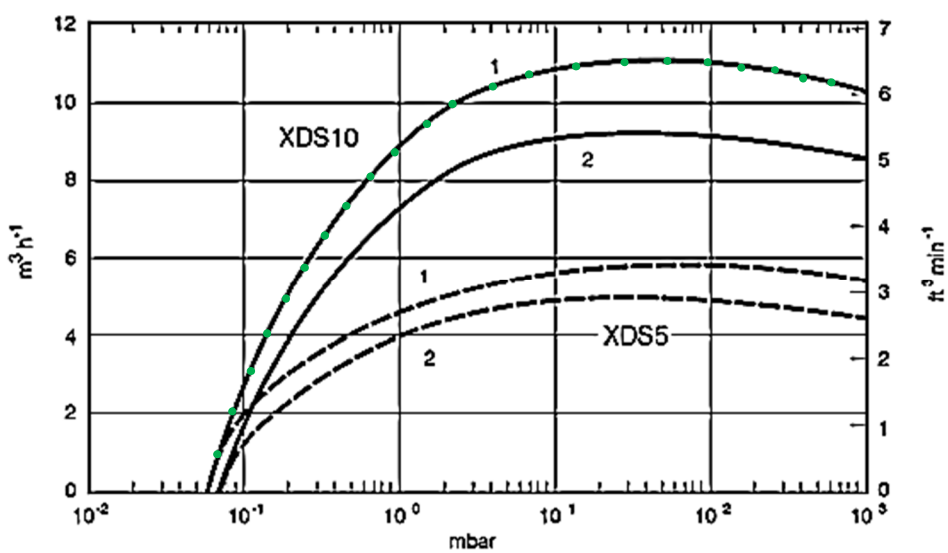

Figure 5.20 Performance Characteristic of the XDS 10 [55].

The convection gauge (CG) is a 275i convection gauge module from Kurt J. Lesker (see Figure 5.21). The CG is a convection-enhanced Pirani gauge which is why it has a relatively wide pressure range of 0.4 mTorr to 1000 Torr. It has a 9-pin d-sub adapter which is connected to a 24 V power supply. Appendix A.6 provides a guideline for the setup of the correct pressure reading.

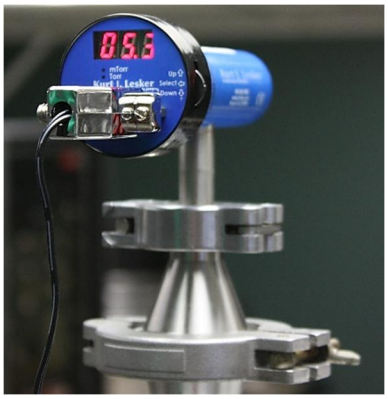

Figure 5.21 Convection Gauge.

5.4.3 Vacuum Gate Valve

The gate valve for the nEXT line (TPGV) is a vacuum gate valve from VAT. It is pneumatically actuated and operated via a customized control panel TPGV CP (see Figure 5.22). The sealing technology is based on the VATLOCK system.

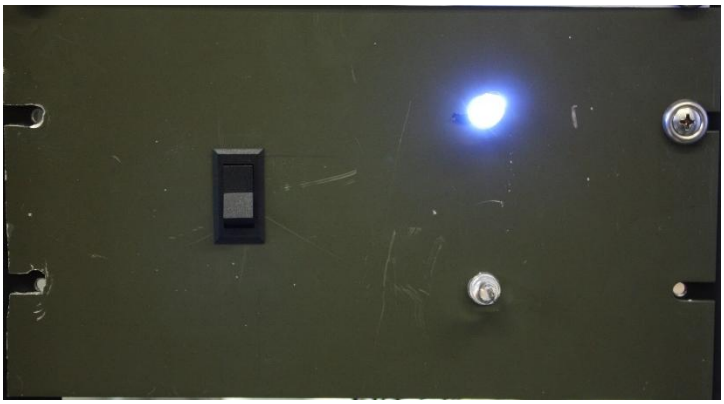

Figure 5.22 TPGV Control Panel.

The switch on the control panel opens and closes the solenoid valve (SV) which is directly connected at the air inlet port of the TPGV. The SV has a 24 V power supply connected to it. Two LED indicate the OPEN or CLOSED position of the TPGV.

The compressed air is supplied by an air compressor. This air compressor is located behind the wall of the clean room area. It needs to be turned on in order to operate the TPGV. Once the air compressor is switched on, it automatically provides the necessary air pressure.

5.4.4 Operation Sequence of the nEXT line

When starting the nEXT, the actions listed below need to be taken.

1. Turn on the air compressor.
2. Close TPGV by turning the switch on the TPGV control panel to the OFF position (CLOSE LED should illuminate blue).
3. Close AV 1 (manually).
4. Open AV 2 (fore-line of the nEXT).
5. Turn on the TIC. While turning it on, check that the 3 LEDs on the nEXT controller (bottom of the nEXT) light up for approximately 0.5 s and then extinguish. The air fan of the nEXT should start running now.
6. Start the backing pump XDS.
7. Look constantly at the pressure gauge (CV).
8. When the pressure (CV) is less than 20 Pa (below 100 mTorr), below 4 Torr (according to Al Kosses from Edwards), open the TPGV by turning the switch on the TPGV control panel to the ON position (OPEN LED should illuminate in white).
9. Start the nEXT via the TIC by pressing the CYCLE button ( ).The green LED on the nEXT controller illuminates when the pump reaches normal speed (80 % of full speed as a default value, different setting

possible). This depends on the preset ramp time. When the nEXT is running the TIC displays that the Turbo is ON and RUN if the nEXT is operating above 50 % of the normal speed.

10. Constantly look at the pressure on the chamber (WRG 1). This is displayed on the TIC (pressure gauge CHAM).

The TAV5 solenoid vent valve will automatically close when the pump is started.

The nEXT can be shut down by following the subsequent steps:

1. Turn on the air compressor.
2. Close the TPGV by turning the switch on the TPGV control panel to the OFF position (CLOSE LED should illuminate blue).
3. Stop the nEXT via the TIC by pressing the CYCLE button.
4. At 60 % of the rotational speed close AV 2 and turn the XDS off.
5. The TAV5 is automatically turned on by the TIC when the rotational speed of the nEXT drops below 50 %.

5.5 The Load Lock Vacuum Line

The load lock vacuum line, short LL line, is the path for the substrate to get into the main chamber. It consists of the manually operated standard gate valve (LLGV), the load lock chamber, and the linear rack and pinion transporter (LRP). The LL line is portrayed in Figure 5.23.

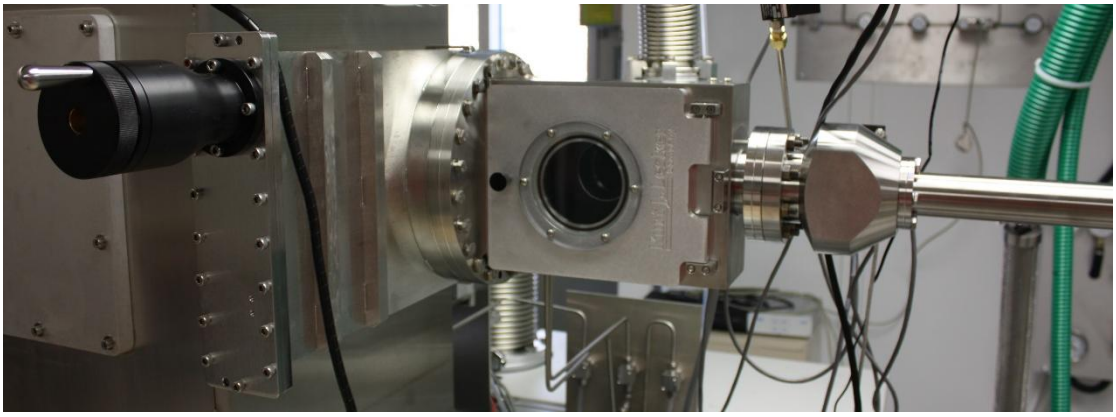

Figure 5.23 Load Lock Vacuum Line.

5.5.1 Load Lock

The load lock (LL) is the opening portal for the substrate into the chamber. It is a small stainless steel vacuum chamber which is depicted in figure XX. Besides the connections to the LLGV and the LRP, it has three additional orifices. There is a connection to the nEXT via a flexible hose. In case of the evacuation of the LL this line is opened through the angle valve AV 1. Moreover there is a vent port attached to the LL, as well as a wide range gauge (WRG 2). This WRG is connected to the TIC.

The rectangular opening is the orifice for the substrate motion into the chamber. Its dimension are 2.74” x 7.74”. This limits the maximum height of the substrate to 7”.

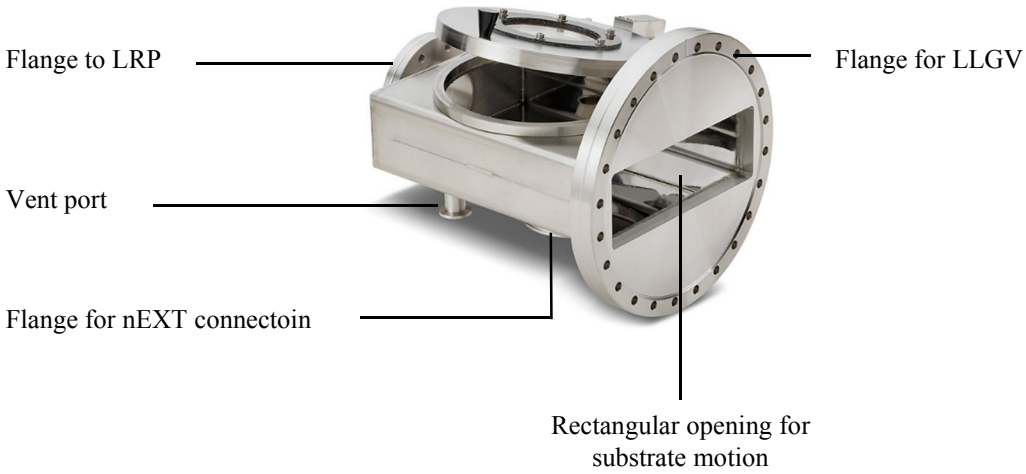

Figure 5.24 Load Lock Used for the HCSS [51].

5.5.2 Linear Rack and Pinion Transporter

The linear rack and pinion transporter (LRP) serves as the linear motion transporter for the substrate. It has a total transport length of 24". The LRP's 1" diameter extruded aluminum transfer arm with a ½ " diameter end effecter has a hardened stainless steel rack insert for strength and durability. It is driven by an aluminum bonze pinion gear. It has two diametrically opposed hardened stainless steel bearing-guide shafts that ride on a precision chamfered eight-bearing support carriage. This ensures special construction ensures rigidity for heavier load transfer. The operating load capacity of the LRP is 1.5 lb (680 g). It has a deflection of 0.033" under a load of 1 lb.

The LRP is actuated through a SmartMotor Series 4 (SM2315D) from Animatics. The SmartMotor (SM) unit has an integrated controller and connects via a RS232 interface to a computer. Moreover, it is connected to a 24 V power supply. The entire LRP setup is depicted in Figure 5.25. Figure 5.26 illustrates the correct cable assembly.

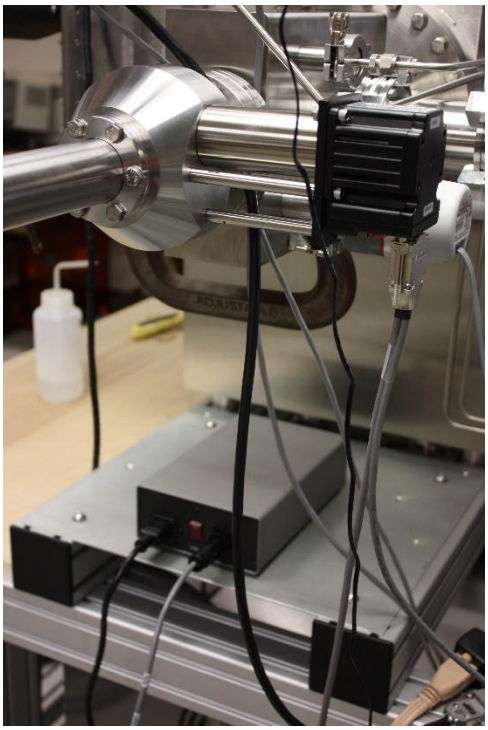

Figure 5.25 LRP Setup (With Connections to Power Supply and PC).

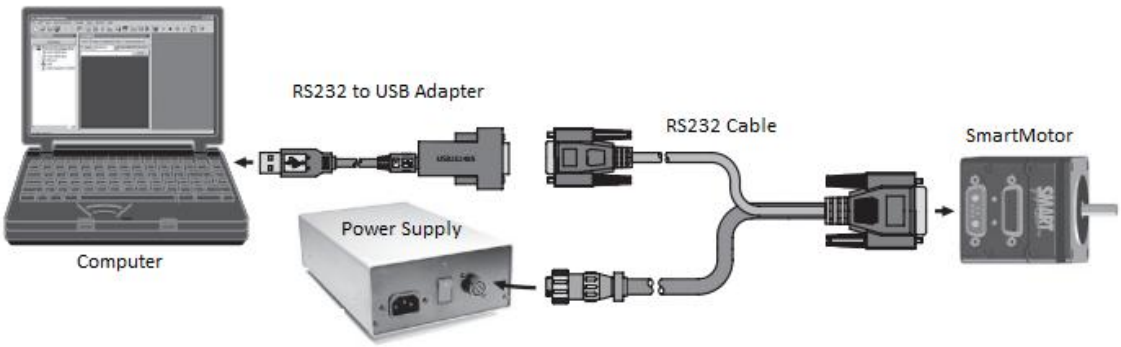

Figure 5.26 SmartMotor Cable Assembly [56].

The SM is an entire servo control system built inside of a servo motor. It includes a controller, an amplifier and an encoder. All that is required for it to operate is power and either an internal program or serial commands from outside (or both). To make the SM move, the program or serial host must set a mode of operation, state a target position with/or a maximum velocity at which to travel to that target, and a maximum acceleration. After these three parameters are set, and the two limit inputs are properly grounded or

deactivated, a GO command starts the motion profile. The core functional areas of the SM are:

(i) Motion control functions

(ii) System control functions

(iii) Communication functions

(iv) I/O functions

The SM has two status LEDs which are explained in Table 5.11.

Table 5.11 SmartMotor Status LEDs and their Meaning [56]

LED	Status	Meaning
LED 0 (-): Drive status indicator		
	Off	No power
	Solid green	Drive is on
	Flashing green	Drive is off
	Flashing red	Watchdog fault
	Solid red	Major fault
	Alternating red/green	In boot load, needs firmware
LED 1 (+): Trajectory status indicator		
	Off	Not busy
	Solid green	Drive on, trajectory in progress

In order to program, control and monitor the SM the *Smart Motor Interface* (SMI) software has to be used. The SM was initialized using the COM12 port on the computer (Lenovo Think Pad). It is labeled with Motor1-COM12 in the SMI software. The SMI software window is shown in Figure 5.27. The blue field is for giving instant commands to the SM. The window on the right side of Figure 5.27, reflects the *Motor View* of the SMI software.

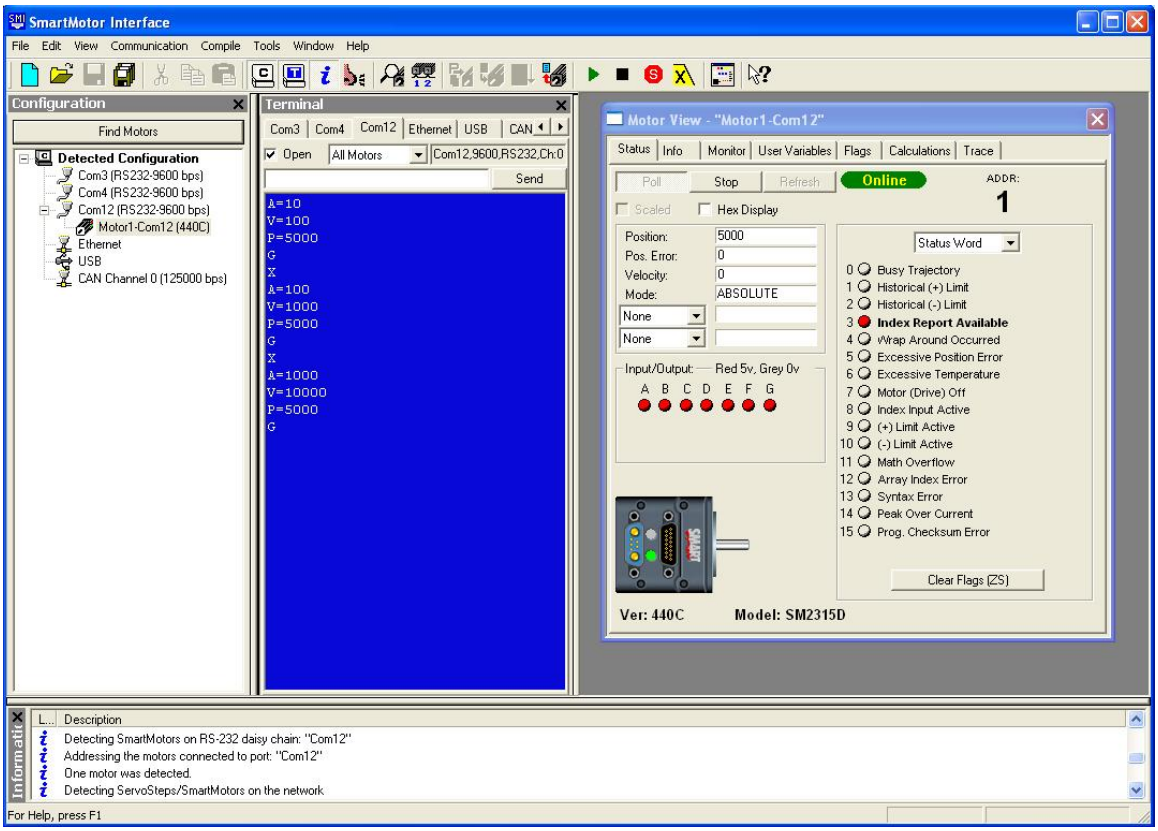

Figure 5.27 LRP Software SMI.

The *Motor View* provides all the status information of the SM, e.g. position, velocity, and torque. The *SmartMotor Playground* is a part of the SMI software which makes it possible to give instant commands to the motor while a motor program is running. With the *Playground*, the SM can be stopped at any time by pressing the "S" button. A program can be downloaded to the SM in order to determine an automated movement. This will be implemented for the substrate movement inside the chamber at a later point of the HCSS project.

The overall steps the SM is able to make are 30,000. Consequently, the resolution is 1,250 steps/inch. Thus, the LRP can be controlled with a high precision. The SM uses its own scaled counts. In order to program the SM correctly the conversions given in Table 5.12 have to be considered.

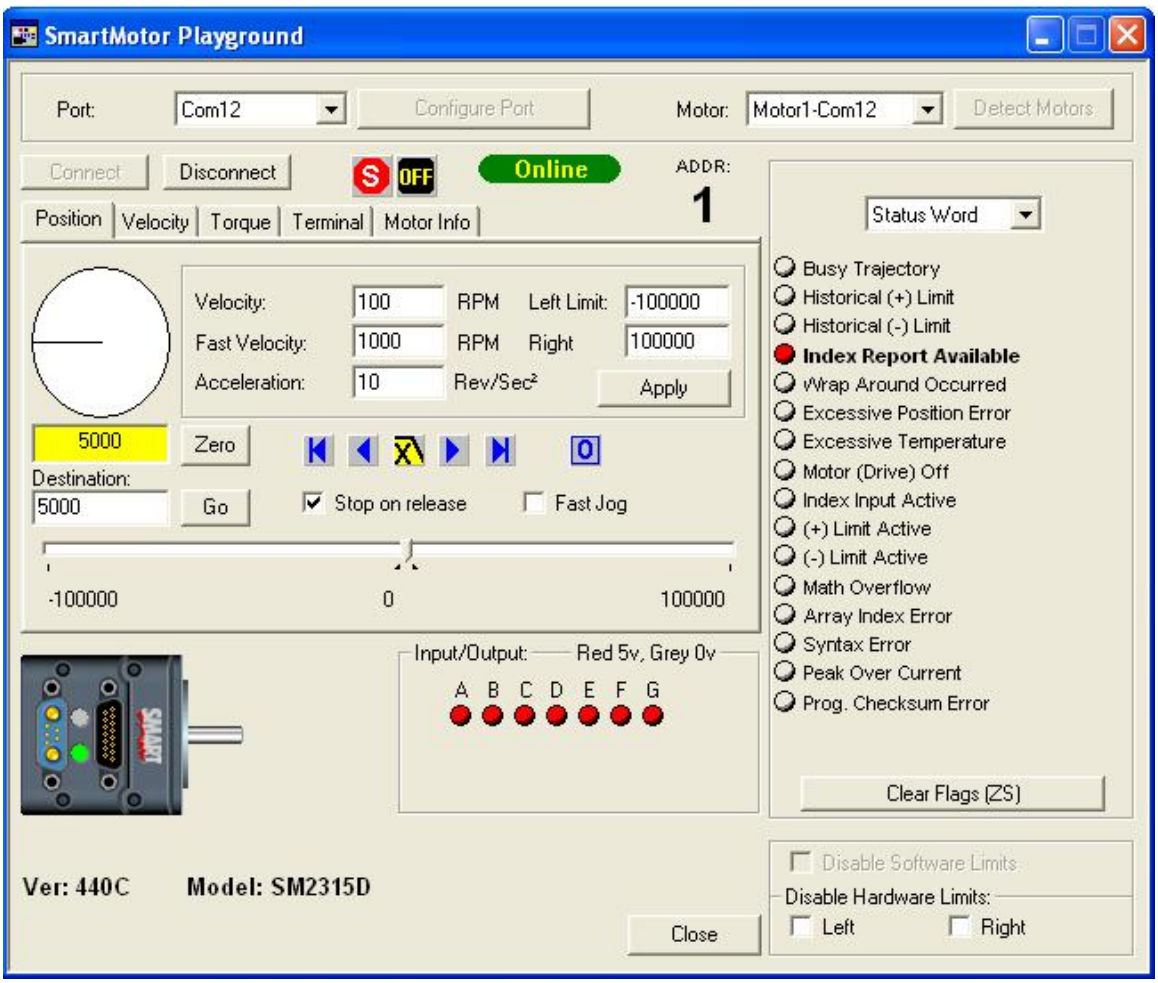

Figure 5.28 SMI SmartMotor Playground.

Table 5.12 SmartMotor Parameters, their Ranges and Conversions

Parameter	Symbol	Range	Conversion
Position	P	0 to 30,000	P = rev x 2000
Velocity	V	0 to 2,147,483,648	V = rev/sec x 32212
Acceleration	A	0 to 2,147,483,648	A = rev/sec² x 7.91

5.5.3 Operation Sequence of the Load Lock Line

The nEXT is used for pumping down the load lock. The pump down sequence is similar to the nEXT sequence for evacuating the chamber.

1. Turn on the air compressor.
2. Close TPGV by turning the switch on the TPGV control panel to the *OFF* position (*CLOSE LED* should illuminate blue).
3. Open AV 1 (manually).
4. Open AV 2 (fore-line of the nEXT).
5. Turn on the TIC. While turning it on, check that the 3 LEDs on the nEXT controller (bottom of the nEXT) light up for approximately 0.5 s and then extinguish. The air fan of the nEXT should start running now.
6. Start the backing pump XDS.
7. Look constantly at the pressure gauge (CV).
8. When the pressure (CV) is less than 20 Pa (below 100 mTorr), below 4 Torr (according to Al Kosses from Edwards), open the TPGV by turning the switch on the TPGV control panel to the ON position (OPEN LED should illuminate in white).
9. Start the nEXT via the TIC by pressing the CYCLE button ( ).T green LED on the nEXT controller illuminates when the pump reaches normal speed (80 % of full speed as a default value, different setting possible). This depends on the preset ramp time. When the nEXT is running the TIC displays that the Turbo is ON and RUN if the nEXT is operating above 50 % of the normal speed.
10. Constantly look at the pressure in the load lock (WRG 2). This is displayed on the TIC (pressure gauge LL).

To stop the nEXT after evacuating the load lock, the steps enumerated below need to be taken.

1. Close AV 1.
2. Stop the nEXT via the TIC by pressing the CYCLE button.
3. The TAV5 is automatically turned on by the TIC when the rotational speed of the nEXT drops below 50 %.

At 60 % of the rotational speed close AV 2 and turn the XDS off.

5.6 The Sputtering Power Supply

The sputtering power supply is a programmable pulsed DC plasma generator which is a RPDG-50 from MKS. In the following, as well as in HCSS piping diagram, it is denoted with RPDG.

The RPDG is mounted at the full rack of the main frame. It is connected to a 3 phase 208 V supply voltage which can be shut off by a disconnect switch. The RPDG provides a 5 kW output. It draws a maximum current of 25 A per phase and the nominal current is 15 A. A coaxial cable is used for the output connection for the purpose of minimizing stray inductance and capacitance because reactive processes are especially sensitive to arc energy. A typical setup of the PRDG in a sputtering system is portrayed in Figure 5.29 and the detailed cable assembly is illustrated in Figure 5.30. The output cable has UHF male connections.

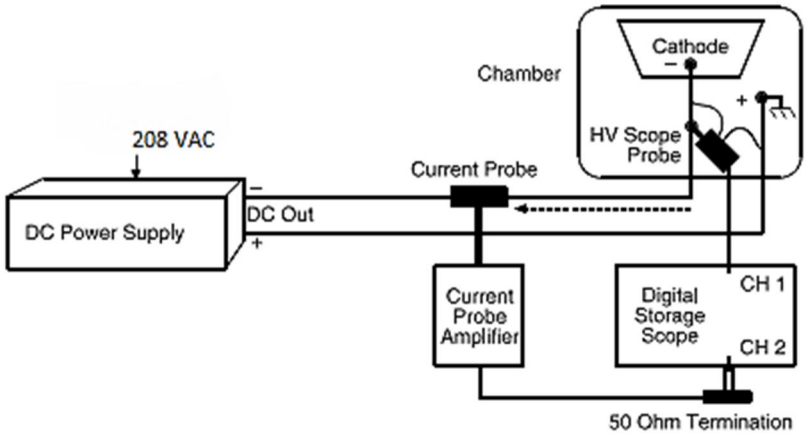

Figure 5.29 RPDG Connection Diagram [57].

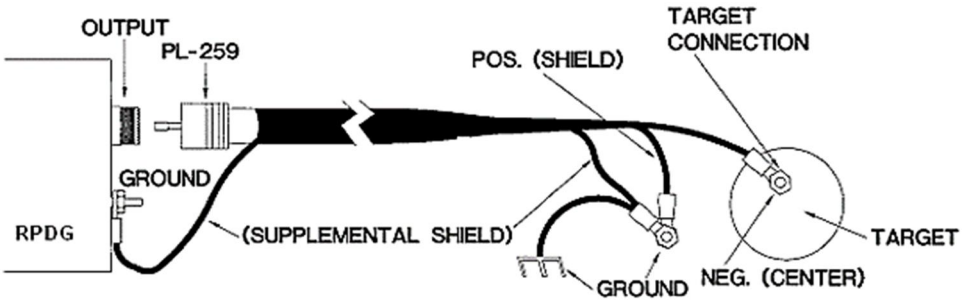

Figure 5.30 Detailed Cable Assembly for the DC Output of the RPDG [57].

The RPDG is equipped with an RS232-RS422 serial control interface. A standard 9-pin female D-type connector is used for the connection between the RPDG and the computer. During the initial operation of the HCSS the RPDG is operated locally through the front panel. However, the remote operation mode through a digital user interface (PC) might be added at a later point. The local mode is selected by pressing the LOCAL/REMOTE button on the front panel (see Figure 5.31). In this case the LED will turn off.

Figure 5.31 RPDG Front View (Control Panel).

The display of the RPDG comprises of two lines (see Figure 5.32). The top line displays the measured output of the generator in volts (V), amps (A), and watts (W). The bottom line displays the set point, pulse frequency in kHz, and pulse width in ns, when the pulse mode is on.

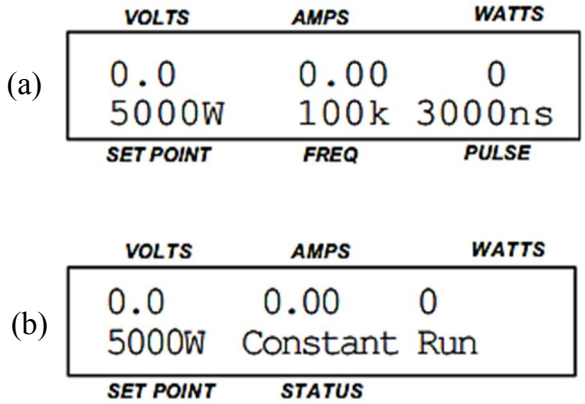

Figure 5.32 Display of the RPDG: (a) Pulse Mode On, (b) Pulse Mode Off [57].

Besides the display, the front panel of the RPDG contains six LEDs. Four of the LEDs are inside the FAULT/RESET, PULSE, REMOTE ENABLE, and LOCK buttons. The other two LEDs indicate the presence of AC (top) and the enabling of the DC output (bottom). Table 5.13 presents the buttons for normal operation and their function.

Table 5.13 RPDG Front Panel Buttons and their Function [57]

Button	Function
DC output ON/OFF	Output control of the RPDG LED ON: RPDG begins regulating according to the selected regulation mode with timing as prescribed by the presently selected run mode. LED OFF: timers for any of the run modes pause
Fault reset	Clearance of fault indication (listed in display) when the fault has been removed and return to normal operation. Stop the current run (timers are set to zero and will start from the beginning when the DC is turned back on)
Reg Mode	Selection of one of the three regulations modes: volts (V), amps (A), watts (W)
Run Mode	Selection of one of the four run modes: constant run, sequence, joules, run-time
Remote	Enabling/Disabling remote operation
Front panel lock	Lock/Unlock the digitizer knob and all front panel controls
Pulse	Enabling/Disabling the pulse mode

The CONSTANT run mode causes the RPDG to deliver the predetermined output until the run is stopped by pressing the Fault Reset button. The ramp for running up to the set output power can be set in the Setup/Misc menu. The complete menu structure of the RPDG is presented in appendix A.5. The RUN-TIME mode allows the DC output to be set to a specific output level and held for a specific period of time. In the JOULES mode an output level can be selected and that level then held until the desired power (number of joules) have been delivered to the cathode. Thereby a current value can be set in the regulation mode. Using SEQUENCE mode, the output of the RPDG can be varied over time. A waveform (steps of the set DC voltage) can be automatically applied to the cathode. The SEQUENCE mode can be configured to work as an amount of joules to deliver per

sequence step versus a direct time value. This is selected by choosing the sequence leveling type of W(J), V(J), or A(J).

The RPDG is featured with the capability of elimination of the arc, caused by target poisoning, by regularly pulsing a positive bias into its output to the target for short periods. This positive bias allows a charge to be built up on the dielectric material. During negative bias periods, greater numbers of sputtering ions are pulled to this extra charge preferentially sputtering the poisoning material off. The RPDG contains special circuitry for detection and rapid extinguishing of arcs. Several features and parameters can be controlled via the serial interface and front panel.

5.7 Venting System

The venting system consists of a liquid nitrogen tank, a gas regulator, and a vent panel. The liquid nitrogen tank is used because it comprises a much larger gas volume of a comparable gas tank. The boiled-off nitrogen gas is used for three applications (see also Figure 5.33):

(i) Venting of the chamber (right valve)

(ii) Venting of the load lock (middle valve)

(iii) Venting of the nEXT

(iv) Purging of the GXS (left valve)

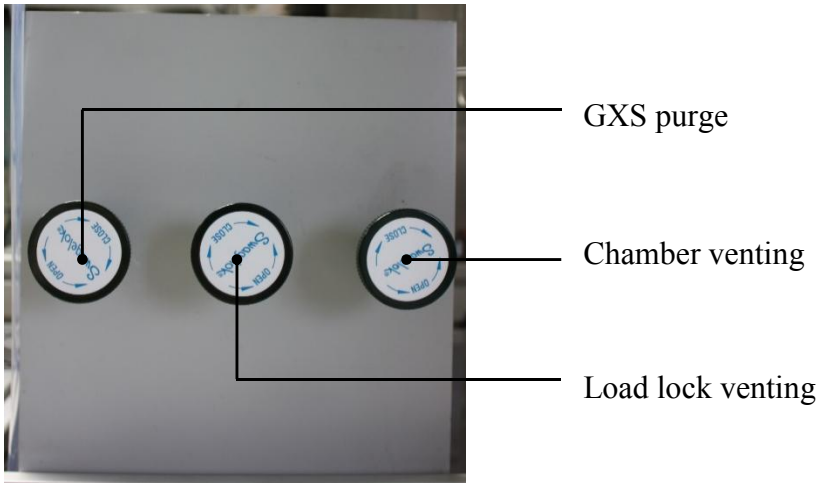

Figure 5.33 Venting Control Panel.

As mentioned before, the nEXT has a solenoid valve which is controlled by the TIC. Venting a vacuum system is the controlled way to bring the vacuum chamber up to ambient pressure, typically in order to open it such that something can be adjusted. In addition, venting of the load lock is necessary when the substrate is changed.

The liquid nitrogen tank from Dura-Cyl contains about 5000 ft^3 gaseous nitrogen and it can supply a maximum flow rate of gaseous nitrogen of approximately 400 scfh (=188779 sccm).

The connections of the tubing are made with Swagelok fittings. Swagelok tube fittings create a leak-tight seal for vacuum applications.

5.8 Gas Flow Control Panel

5.8.1 Control Panel

The gas flow control panel is used to monitor and control the gas flow of the process gas argon and the reactive gases nitrogen and oxygen, which are used for the reactive sputtering mode. The gas flow control panel is illustrated in Figure 5.34. It consists of three gas lines, one for each gas. It also provides the option for an additional line (the holes for the assembly of a fourth line are already there). Each gas line has an upstream shut-off valve (Swagelok valves V1-V3) and a downstream shut-off valve (Swagelok valve V4-V6). In between these two valves is the mass flow controller (MFC) from Brooks Instrument positioned. Furthermore, there is an option for a combined argon-nitrogen supply (V7). If this valve is open nitrogen flows only in the nitrogen gas line, whereas nitrogen flows in the argon gas line when V7 is closed.

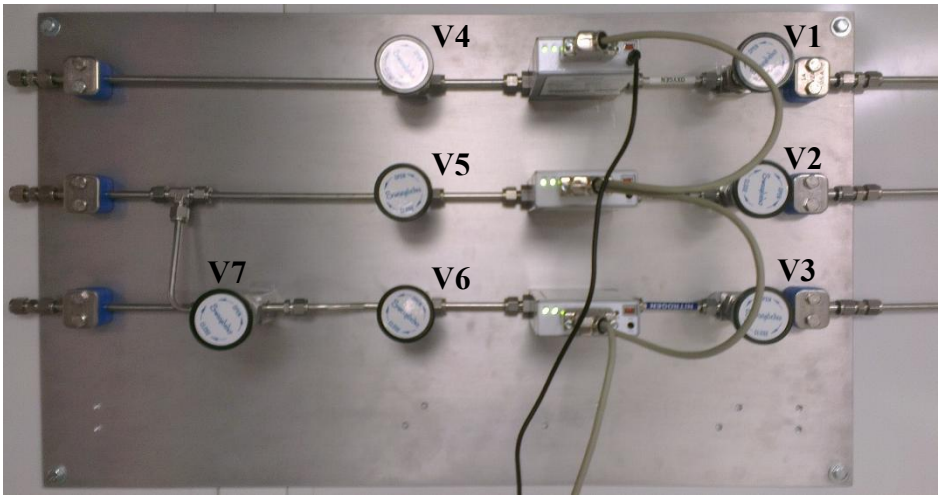

Figure 5.34 Gas Flow Control Panel.

The multi flow controller connects via a RS485 connection to the Brooks Instrument Controller (grey cable in figure 3-1). The black cable is the connection to the PC via USB.

5.8.2 Gas Supply

All the gases are provided by Airgas. They have a minimum purity of 99.9999 % and come in a high pressure cylinder of the size of 300, which means they have an internal volume of 49.8 l at a nominal pressure of 2,640 psig (at 70 °F). Each gas cylinder attaches to a gas regulator, also from Airgas, through a flexible metal hose (see Figure 5.35).

Figure 5.35 Gas Regulator and Flexible Hose (Attached to the Gas Cylinder).

The gas regulator is equipped with two pressure gauges. The pressure gauge on the right site indicates the internal cylinder pressure. The other pressure gauge shows the outlet pressure in the gas line. This outlet pressure is adjustable and should be in a range of 25 to 40 psig.

5.8.3 Operation

The multi flow controllers are thermal mass flow devices which consist of two main components:

- The restrictor, or bypass, and
- The flow sensor.

The operating principle is illustrated in the following chart.

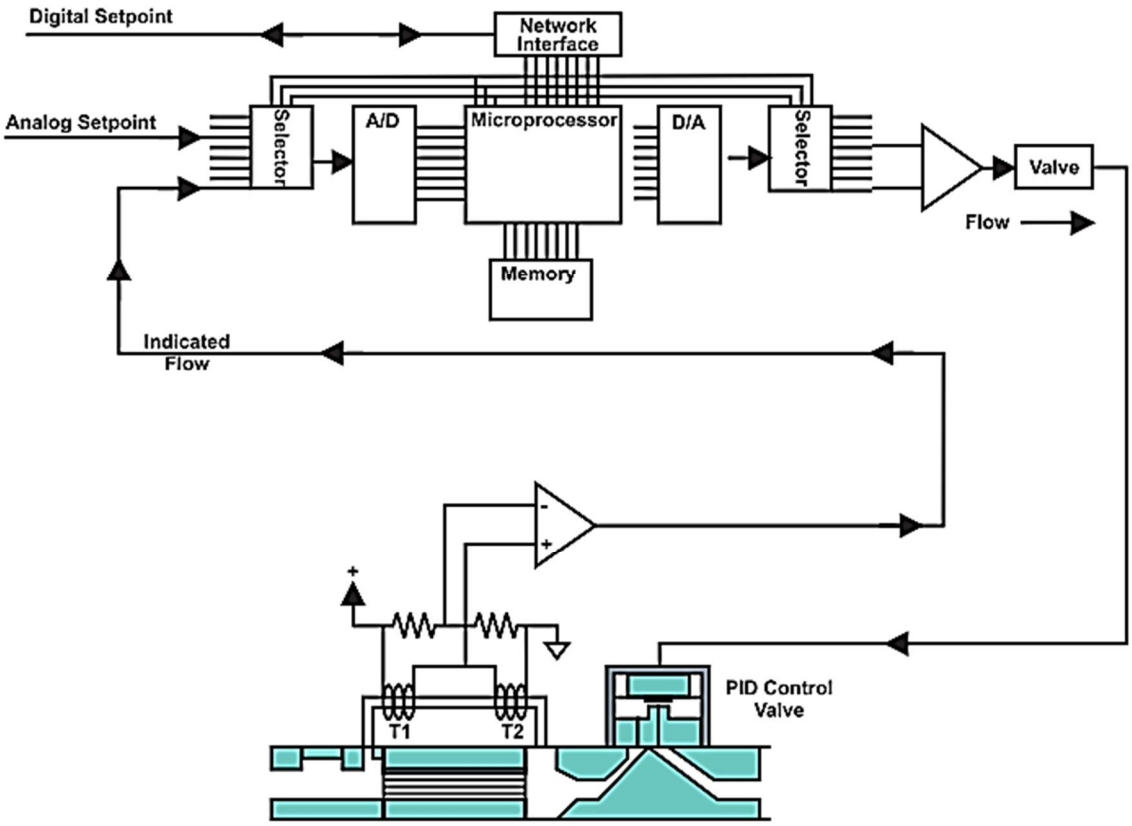

Figure 5.36 Operating Principle of the MFC GF40 [58].

The gas flow entering the device is separated into two paths: one straight through the restrictor and the other through the flow sensor. The flow sensor is a very narrow, thin-walled Hastelloy tube. Onto this tube are built upstream and downstream temperature sensing and heating elements. During no-flow conditions, the amount of heat reaching each

temperature sensor is equal. Hence, temperature T1 and T2 (see Figure 5.36) are the same. Gas flowing through the tube carries heat away from the upstream temperature sensor toward the downstream sensor. The temperature difference, $\Delta T = T2 - T1$, is directly proportional to the gas mas flow. The three MFCs are configured as indicated in Table 5.14.

Table 5.14 Full Scale Flow Rates of the MFCs

MFC (gas type)	Full scale flow rate [sccm]
Nitrogen	1000
Argon	5000
Oxygen	200

In order to operate the MFCs they need to be connected to the controller and the computer, on which the software is running. The whole setting is shown in Figure 5.37.

The Brooks MFC instrument controller provides both the power to the MFCs and a connection to the PC via USB. The software package *Brooks Smart Interface* is used to monitor and control the actual gas flow through the multi flow controllers (MFC) GF40 by Brooks Instrument. A view at the software interface is shown in Figure 5.38. Within that the set point are at 1/5 of the full scale range. It can be observed that the actual flow rate is within the, from Brooks Instrument indicated, accuracy of 0.35 %. VOR stands for valve overwrite. The function of this is explained in Table 5.15 .

Table 5.15 Commands of VOR

VOR command	Explanation
OFF	The MFC is in the normal operational control mode and reaches the set value.
OPEN	The MFC is fully open (no controlled flow rat; the set point is never reached).
CLOSE	The MFC is fully closed.

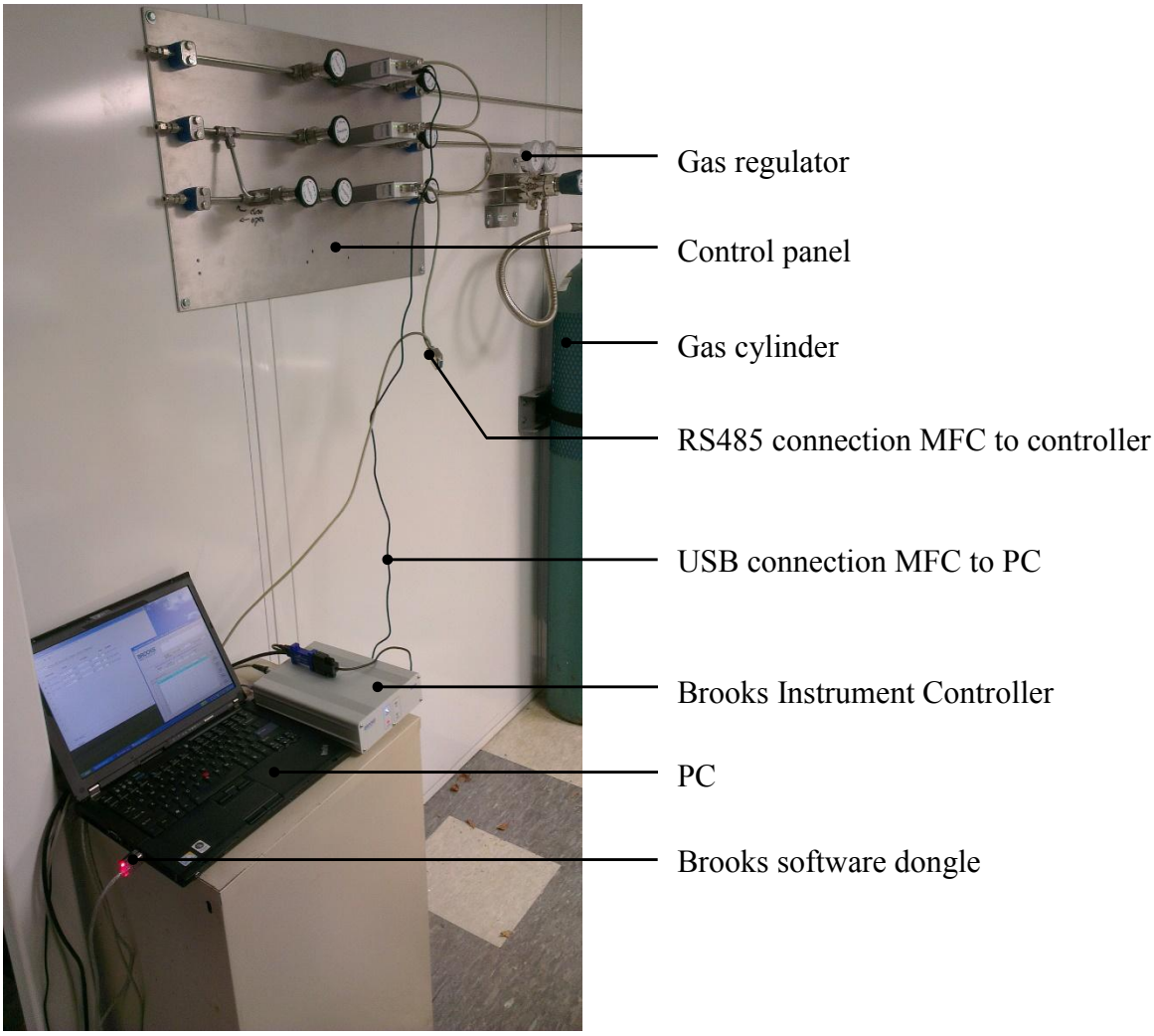

Figure 5.37 Gas Flow Control Operating System.

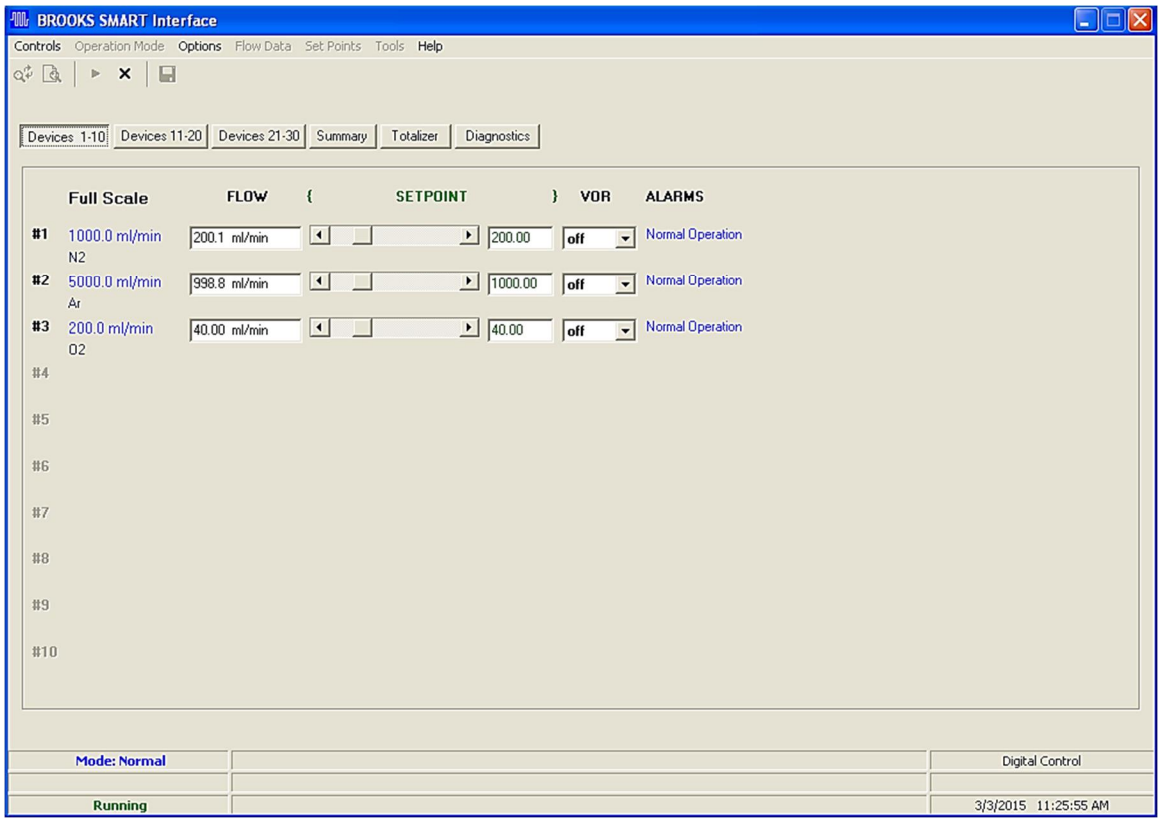

Figure 5.38 View at the Software Brooks SMART Interface.

For configuration purposes of the multi flow controllers there is an additional software, called *Brooks MultiFlo Configurator*. This software configures the MFC regarding gas type, flow rate and pressure settings. All three MFCs came preset in the desired values (see Table 5.14). To reconfigure one of the existing MFCs (or to configure a fourth MFC), the MFC has to be connected to the PC (see figure xx). The interface of the Brooks MultiFlo Configurator software is depicted in Figure 5.39.

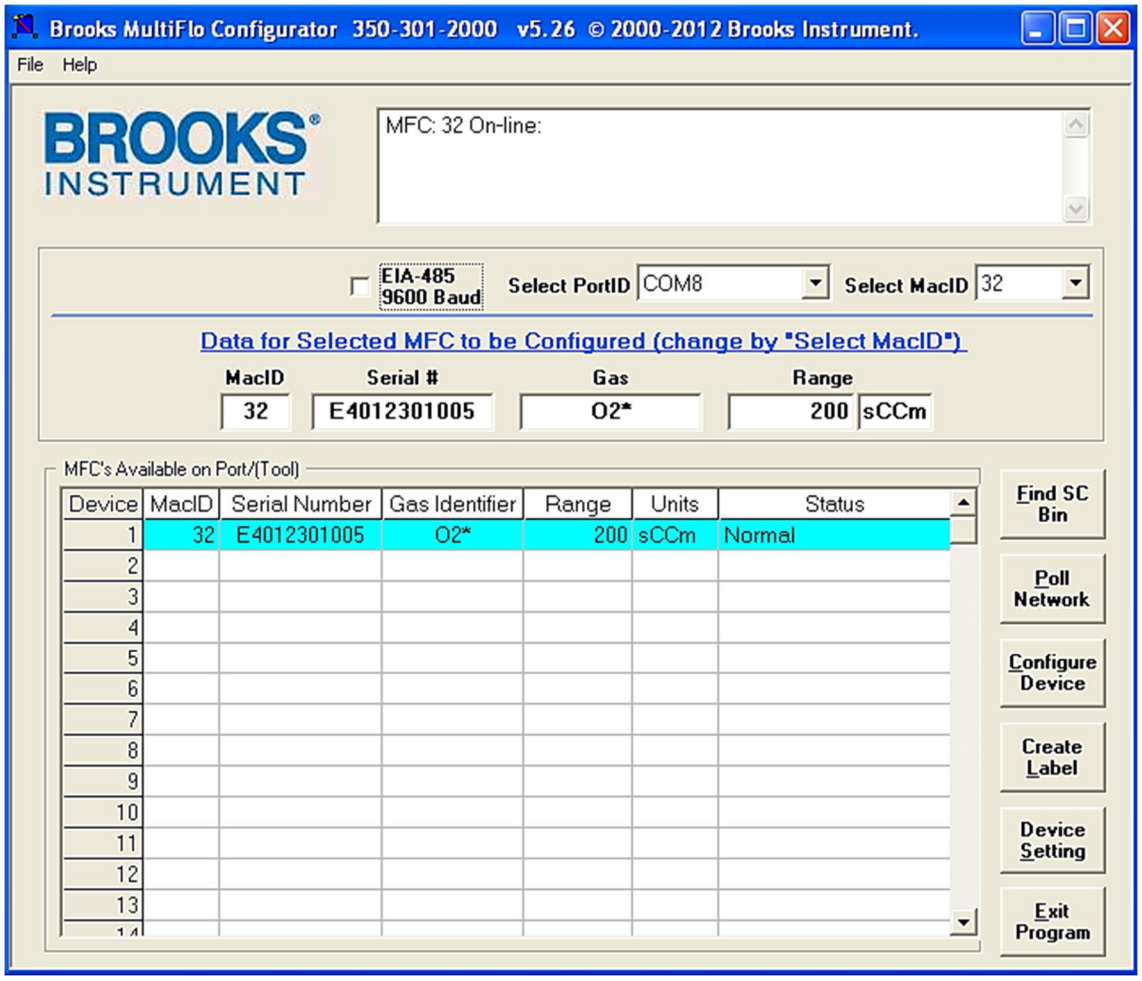

Figure 5.39 Interface of the Brooks MultiFlo Configurator Software.

In order to run both, the Brooks MultiFlo Configurator software as well as the Brooks SMART Interface software, the software dongle has be plugged into the PC.

5.9 Temperature Monitor Interface

The Temperature Monitor Interface (TMI) is a control panel for the process temperatures within the HCSS. The full rack panel is provided by OMEGA. It consists of 10 temperature channels, a channel selection switch and a temperature & process monitor DPi8. The temperatures are shown in °C. A power switch and a fuse were added to ensure a safe 110 Vac power supply. The TMI is shown below.

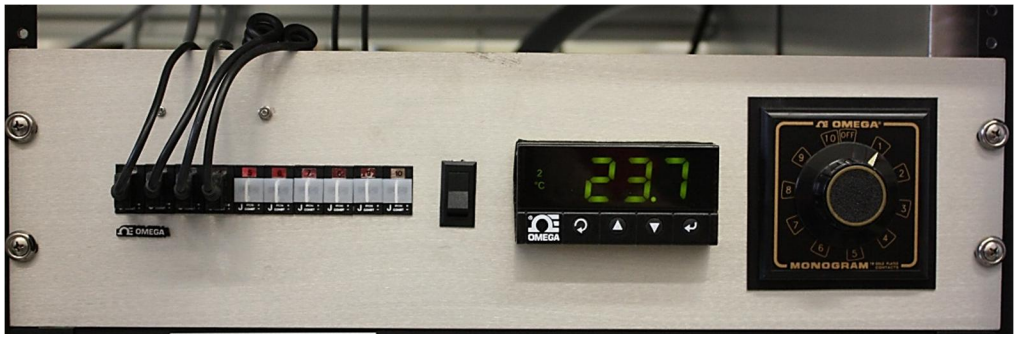

Figure 5.40 Temperature Monitor Interface.

Initially, only 3 channels are in use. These are applied to measure the temperature of:

(i) The substrate,

(ii) The target, and

(iii) The ambient chamber.

The temperatures are measured through a thermocouple. In this case thermocouple of the type J are used. Type J thermocouple use iron as the positive pole and constantan as the negative pole. Inside the chamber the wires of the thermocouple is insulated with fish spine insulators.

The Temperature & Process Monitor DPi8 from OMEGA offers the option of setting alarm points. These can be implemented as an alarm for a too high temperature, too low temperature, or even for a temperature band.

A configuration flow chart for the DPi8 is revealed in appendix A.1.

CHAPTER 6

EXPERIMENTAL DATA

6.1 Initial Start of the Pump Systems

For the initial start of the pump systems, the GXS and the nEXT were connected to the main chamber in order to analyze the evacuation characteristics. The more often this evacuation process was conducted, the better ultimate pressures was attained. This is due to the fact that the whole vacuum system outgases. Outgassing is a typical source of contamination in a vacuum system which refers to the diffusion of gas to the surface where it desorbs [22]. The XDS performance was determined by evacuating only the backing line (AV 2 was closed during that process). Table 6.1 elucidates the ultimate pressures achieved for all three pumps and the time it took to evacuate the chamber.

Table 6.1 Ultimate Pressures and Evacuation Times for the Vacuum Pumps

Pump	Ultimate pressure [mTorr]	Evacuation time [min]
GXS	0.25	90
XDS	3.3	10
nEXT	7.8×10^{-4}	120

The evacuation characteristic of the GXS and nEXT are illustrated in Figure 6.1. The GXS reaches its full speed very fast and after 90 minutes of operation an ultimate pressure of 0.25 mTorr was attained. In contradiction to the GXS, the nEXT ramps up to its full rotational speed. Thus, Figure 6.1 (green crosses) shows that there is a significant pressure drop between 2 and 3 minutes of operation. In between that period of time the nEXT reached 80 % of full rotational speed. At minute 4, the nEXT was running at its full

rotational speed. The ultimate pressure, achieved after 120 minutes of operation, was 7.8 x 10^{-4} mTorr.

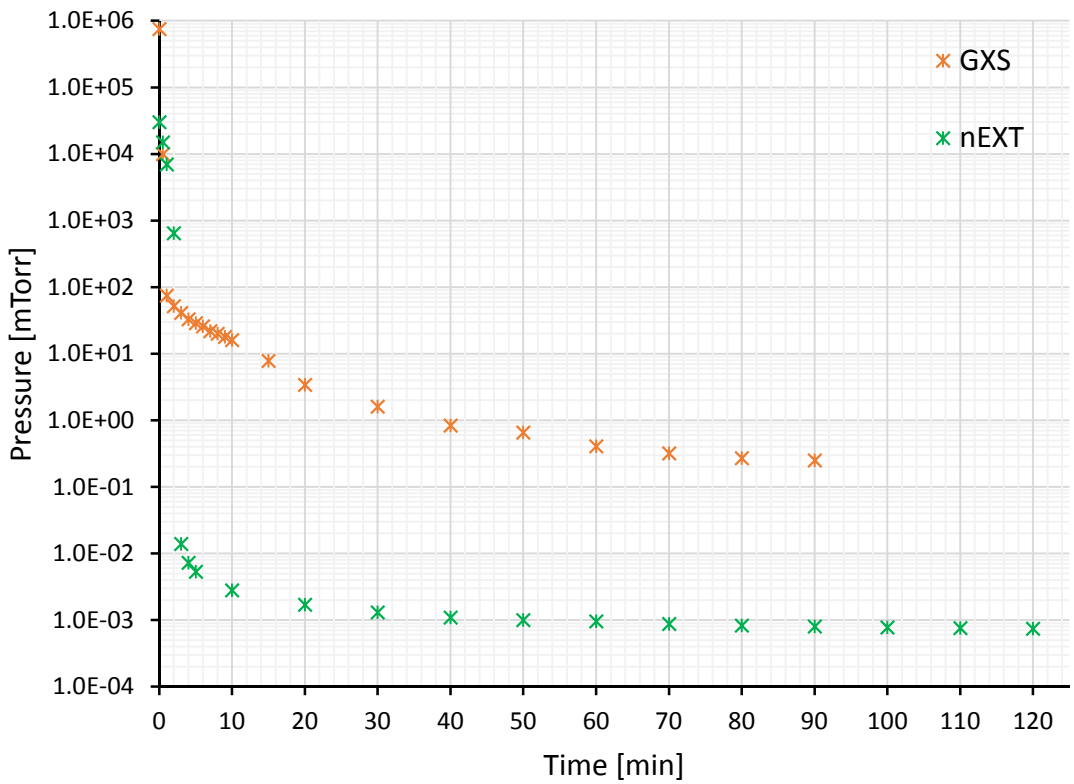

Figure 6.1 Evacuation Curve of the GXS and nEXT.

6.2 Leak Characteristics

After several evacuation cycles of the chamber and the load lock, the leak characteristics were determined. This is necessary in order to assess whether the vacuum system is leak tight. There are several reasons for a constant, but small, leak rate. The most common one is outgassing. If the increase of pressure in caused by outgassing the pressure reaches an eventual maximum in which either the supply of gas that is trapped is exhausted, resulting in uniform pressure throughout or, in the case of evaporating vapor, gaseous and surface phases come into equilibrium. This behavior represents a virtual leak [63].

Both the chamber and the load lock were evacuated with the nEXT. The ultimate pressure reached for the chamber was 7.7 x 10^{-4} mTorr and for the load lock 1.4 x 10^{-2} mTorr. After achieving these pressures the TPGV and AV 1 were closed and the pressure increase was determined. The results are illustrated in Figure 6.2.

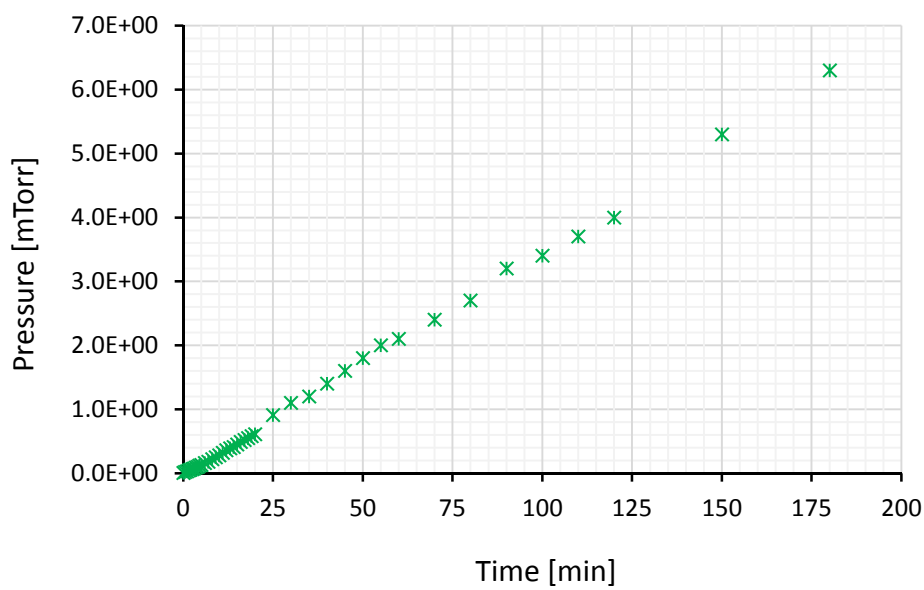

Figure 6.2 Chamber Leak Characteristic.

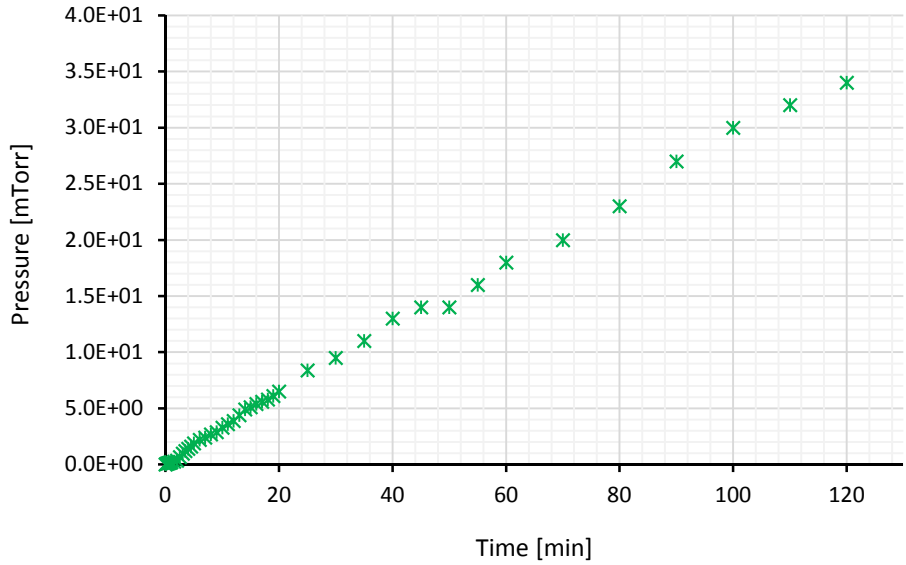

Figure 6.3 Load Lock Leak Characteristic.

The leak rate Q_L can be calculated applying equation (6.1).

$$Q_L = \frac{\Delta p\, V}{t} \tag{6.1}$$

Hence, the chamber exhibits a leak rate of 8.2 x 10^{-2} mTorr l/s (assuming a volume of 140 l) and the load lock 9.4 x 10^{2} mTorr l/s (assuming a volume of 20 l). Consequently, both vacuum vessels have real leaks. Particularly, the load lock possesses a large leak. According to [64] vacuum systems with a leak rate smaller than 7.5 x 10^{-3} mTorr l/s are leak tight (see Table 6.2). Appendix C shows conversion tables for different pressure units.

Table 6.2 Quantitative Characterization of a High Vacuum [64]

Characterization of high vacuum	Leak rate Q_L [mTorr l/s]
Very tight	< 7.5 x 10^{-4}
Tight	< 7.5 x 10^{-3}
Leaky	> 7.5 x 10^{-2}

To identify the real leaks, a systematic leak detection needs to be conducted. Thus far the door of the load lock was detected as a possible leak. Other connections of the load lock could potentially leak additionally. To proceed with the identification of the real leaks, blank-offs need to be ordered.

In Addition to the leak test, a pressure increase experiment was conducted. Hereby, the chamber was evacuated with the nEXT until a pressure of 5 x 10^{-6} Torr was reached. After that nitrogen was inserted in the chamber with a constant flow rate of 18.4 sccm (TPGV was closed). This is the flow rate at which the chamber pressure should increase to 1000 mTorr within 10 min assuming a total chamber volume of 140 l. Figure 6.4 underlines that the chamber volume was correctly determined. As expected the pressure increased linearly until it reached 1 mTorr after 9:50 min.

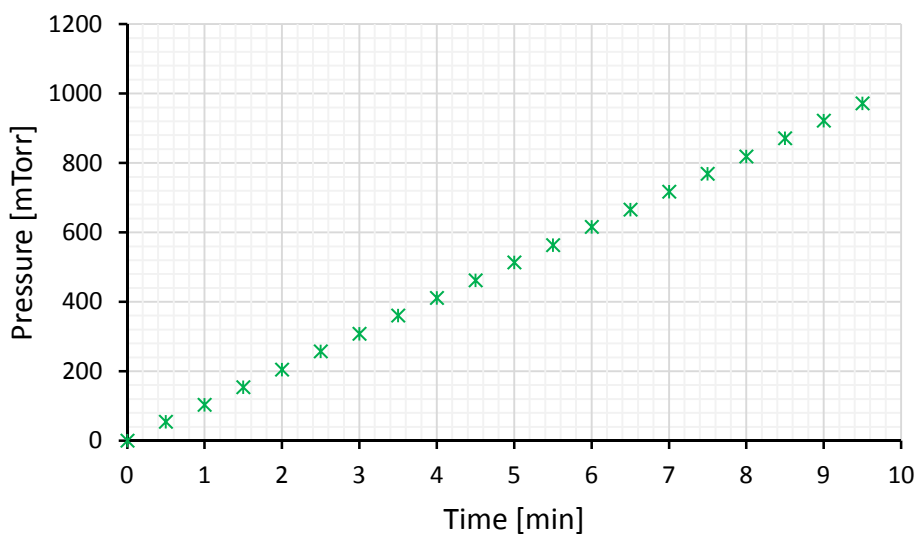

Figure 6.4 Chamber Pressure Increase when Inserting Nitrogen.

6.3 Gas Flow Experiments

In order to determine the argon gas flow characteristics, two experiments were conducted:

(a) Pressure curve depending on the Ar gas flow

(b) Control limits of the CGVC in regards of the Ar flow.

For part (a) the chamber was evacuated with the GXS to a pressure of 1.4 mTorr. After that, Ar was inserted into the chamber with the CGV still open which reflects the general process setting. The Ar flow rate was augmented in 500 sccm increments until the maximum flow rate of 5000 sccm was reached. The ensuing curve is expounded in Figure 6.5 The figure compares the pressure rises for the CM and the WRG 1. It can be observed that the pressure increases linearly with the rise of flow rate. The significant pressure difference between the CM and WRG 1 is due to the fact that both pressure gauges are calibrated for nitrogen and air, respectively. In order to calibrate them for argon, special pressure tables from manufacturers have to be used. In addition, these pressure curves were measured for four different positions of CGV. The result is illustrated in Figure 6.6 for the CM. This figure reveals that the pressure drastically increases when the CGV is only 50 % or less open (curve 400 and 200). It is the consequence of the decreasing pumping orifice and hence, the decreasing pumping speed. At approximately 60 % opening of the CGV, the open area is equivalent to the chamber orifice where the GXS vacuum line is mounted on. If the CGV is 60 % or more open, the GXS can almost maintain the pumping speed and therefore, the pressure follows virtually the same curve when increasing the Ar flow rate. The 200 curve has its last data point at 2500 sccm. The reason for that lies in the full scale range of 1 Torr which is why the CM cannot display pressures above 1 Torr.

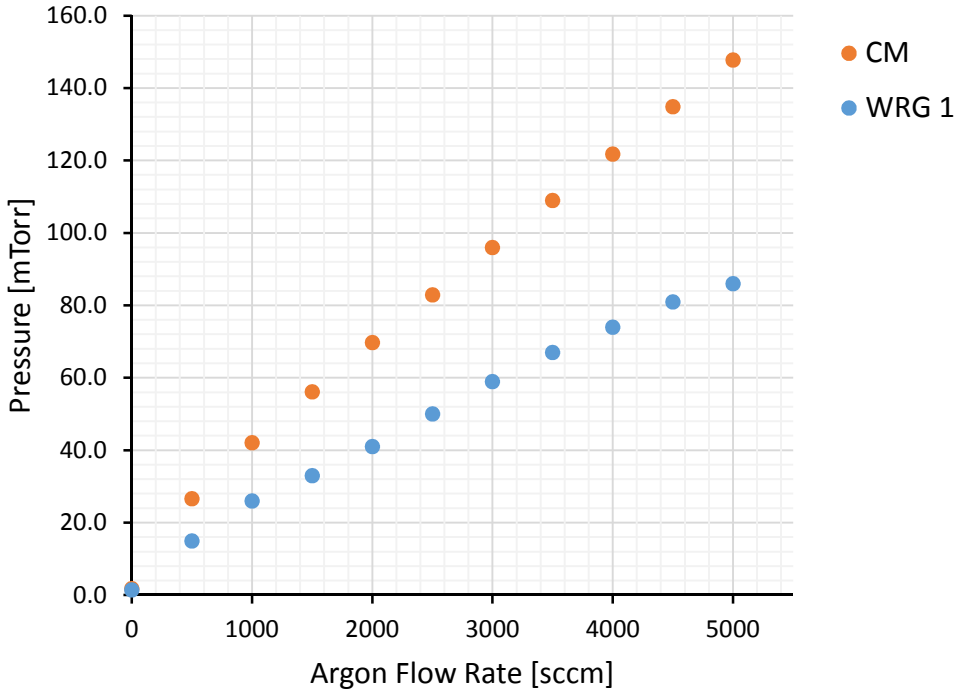

Figure 6.5 Chamber Pressure Depending on the Ar Flow Rate With CGV Fully Open.

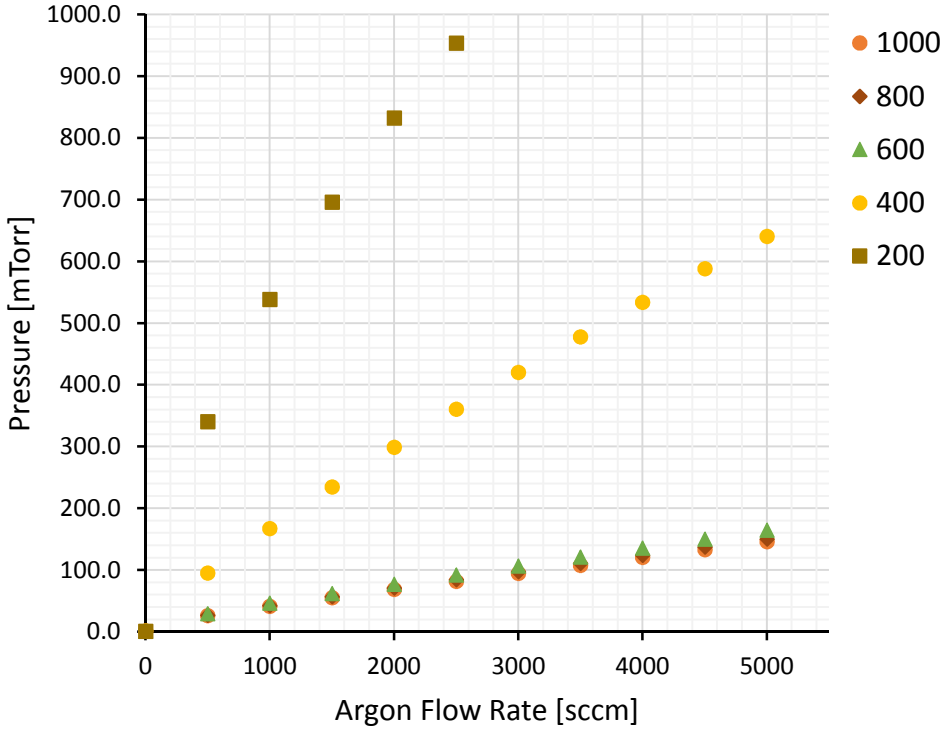

Figure 6.6 Chamber Pressure (CM) Depending on the Ar Flow Rate for Different CGV Positions.

Part (b) inspected the capability of the CGV to hold a certain pressure while varying the Ar flow rate. In this experiment, the ability of the CGV in regards of holding a certain pressure constant while changing the argon flow rate was examined. First, the chamber was evacuated to 0.8 mTorr with the GXS. After that an Ar gas flow of 4000 sccm was adjusted with the *Brooks Smart Interface.* The pressure mode was selected on the CGVC and the pressure was initially set to 200 mTorr. It was determined that the lower pressure limit, which is the pressure the CGVC can hold when the CGV is fully open, is 128 mTorr. In addition, the lower and upper pressure limits for an Ar flow rate of 2000 and 3000 sccm were established (see Table 6.3). The upper pressure limits for an Ar flow of 3000 and 4000 sccm could not be reached because 980 mTorr is the controllable limit of the CGV. At that pressure set point was able to hold the valve door stable at one point (almost closed at position 80).

Table 6.3 Lower and Upper Pressure Limits for Different Ar Flow Rates

Ar flow rate [sccm]	Lower pressure limit [mTorr]	Upper pressure limit [mTorr]
2000	67	849
3000	94	980
4000	128	980

An additional test within part (b) was run to identify the Ar flow rate limits at which the CGVC can hold a certain pressure. For all three set pressures, the lower flow rate limit was 30 sccm. The reason for this lies in fact that CGV control limit was reached. 30 sccm is the lowest flow rate where the CGV could hold the valve door at a stable point (almost closed). The general upper flow rate limit, given by the argon flow controller, is 5000 sccm (see Chapter 5.8). This flow limit was attained for the set pressures of 200 and 400 mTorr

while the CGV was not fully open. At the pressure of 100 mTorr the CGV completely opened when a gas flow rate of 3150 sccm was rechead.

Table 6.4 Lower and Upper Flow Rate Limits for Different Pressures

Pressure [mTorr]	Lower flow rate limit [sccm]	Upper flow rate limit [sccm]
100	30	3150
200	30	5000
400	30	5000

CHAPTER 7

CONCLUSION

The fundamental aims of this thesis were to assemble and prepare all the equipment and components required for depositing transparent conducting oxides by hollow cathode sputtering. The final goal was to deposit first TCOs and to characterize them.

The accomplishments of this work do not reach that far. The thesis presented, includes the whole assembly of the vacuum system part of the HCSS. Due to challenges during the design phase of the hollow cathode, unexpected complications during the installation of some components, and a long delay of the funding, the HCSS could not be fully completed in the given time frame of this thesis.

Nonetheless, essential basics of TCOs and the DC sputtering process were thoroughly discussed. Moreover, the three main TCOs – ZnO, SnO_2, and Cd_2SnO_4 – which will mainly be deposited with the HCSS, were characterized in regards of their material properties and their sputter deposition behavior. This creates the central background for the experiments (deposition of advanced TCOs) as soon as the hollow cathode is implemented in the system.

In the second half of this work a presentation and evaluation of all the installed components were illustrated. Particularly, the pump systems were analyzed and performance characteristics were recorded.

In addition, first basic experiments were conducted in the vacuum system. This included a vacuum test and the determination of Ar-flow-pressure curves.

The built HCSS vacuum system is the platform for future deposition processes of TCOs and HRTs. Next steps contain the implementation and operation of the hollow cathode system, the assembly of the interior components of the chamber, and an overall evaluation of the system's performance. Moreover, the detection and elimination of the major leaks at the chamber and the load lock is a major task before starting the HCS process.

APPENDIX A

ADDITIONAL OPERATION INFORMATION

Figure A.1 shows the configuration flow chart for the DPi8 Temperature & Process Monitor from OMEGA.

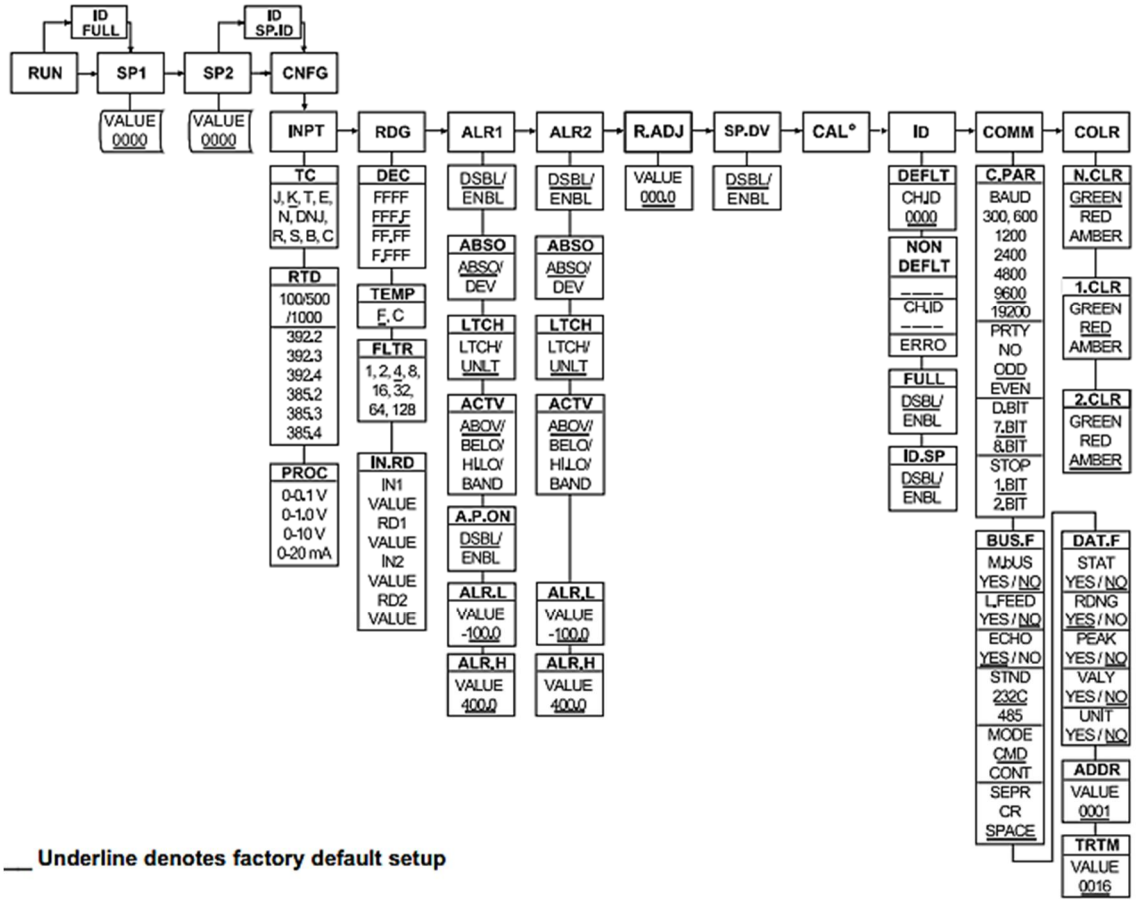

Figure A.1 DPi8 Configuration Flow Chart [60].

Figure A.2 illustrates the setup options for the CVG controller.

STEP		**LOCAL MODE** (PM-4 in combination with Service Box only)	**REMOTE MODE** (PM-5 if interface installed only)
1	**POWER ON**	1. PM controller: Turn on power switch at the rear panel of the PM controller. ***Note:*** Valve will close, if not in closed position 2. On PM-5 or Service Box start-up display (Software version, type of interface, etc.) appears, until valve is in closed position 3. CLOSE(D) is displayed, otherwise please refer to chapter '6 Trouble Shooting'.	
2	**SELECT MODE**	Select LOCAL operation by pressing «LOCAL» key for 2 seconds.	Select REMOTE operation by pressing «REMOTE» key on front panel or Service Box for 2 seconds **or** select remote operation through RS232 (see ‚9.3.1 Control commands') or logic interface (see ‚9.1.3.1 Logic interface')
3	**AUTOMATIC SIZE ADJUSTMENT**	Press simultaneously «OPEN» and «CLOSE» keys for 2 seconds. The controller will perform an automatic size adjustment procedure to determine open and closed position and the range between the two positions.	Send RS232 command: **J:<CR><LF>** (see ‚9.3.1 Control commands') or use Logic command (see ‚9.1.3.1 Logic interface')
4	**SENSOR SETUP**[1)]	Press simultaneously «LEARN» and «ZERO» key for 2 seconds (notation used hereafter: «&», e.g. «LEARN» & «ZERO»). Then, use «↑» and «↓» key to change parameters (VOLTAGE RANGE; DISPLAY RANGE; DISPLAY UNIT; GAIN FACTOR; SENSOR TYPE; ZERO ADJUST) for each sensor. Toggle with «F1» key to the next setup parameter. Press «F2» , when finished.	See ‚9.3.3 Sensor setup command' Example: Sensor 1, Voltage Range: 0-10V; Display Range: 0-10; Display Unit: Torr; Gain Factor: 1; Sensor Type: Torr; Zero Adjust: enabled; **s:1332010<CR><LF>** Mind: Not possible to do by a logic interface.
5	**ZERO ADJUST** (Offset compensation of sensor output)	Evacuate process chamber to high vacuum. When the base pressure is reached, press «ZERO» key for 2 seconds to reset the offset of the pressure sensor. Disable ZERO function in SENSOR SETUP, if the base pressure of your system is higher than 1‰ of sensor full scale.	Evacuate process chamber to high vacuum. When the base pressure is reached send RS232 command: **Z:<CR><LF>** (see ‚9.3.1 Control commands') or use Logic command (see ‚9.1.3.1 Logic interface'). Disable ZERO function in SENSOR SETUP, if the base pressure of your system is higher than 1‰ of sensor full scale.
6	**LEARN** [2)] (Determination of control characteristics of your process chamber)	Process chamber at high vacuum, control valve is open: Open gas inlet and set gas flow (see recommendation below). Press «LEARN» key for 3 seconds to perform the autolearning routine of the PM controller. The autolearning routine may take several minutes and can be aborted by pressing the «F1» key. A single full run of the autolearning routine is required to ensure fast and accurate pressure control. ***Note:*** It is not necessary to repeat **LEARN**, if the sensor setup is changed, or if the second sensor is selected for pressure control. The controller covers 5% to 5000% of the gasflow which was used at **LEARN**.	Process chamber at high vacuum, control valve is open: Open gas inlet and set gas flow (see recommendation below). Then send RS232 LEARN command: **L:001000<CR><LF>** (‚9.3.1 Control commands') or Logic command (see ‚9.1.3.1 Logic interface'). The autolearning routine may take several minutes. A single full run of the autolearning routine is required to ensure fast and accurate pressure control. ***Note:*** It is not necessary to repeat **LEARN**, if the sensor setup is changed, or if the second sensor is selected for pressure control. The controller covers 5% to 5000% of the gasflow which was used at **LEARN**.

Legend:

1) The default **GAIN FACTOR** is 1.00. See chapter ‚9.3.3 Sensor setup command' if resetting is necessary.
- gain factor > 1 means: faster control but higher overshoot of pressure
- gain factor < 1 means: slower control but lower overshoot of pressure

Just 98% of sensor pressure range can be used during control.
If no sensor is used, select as display parameter 'POS'.

2) Ideal gasflow for autolearning

$$Q = 40 \bullet p_{SFS} \bullet L_{min}$$

Q.....gasflow for autolearning [sccm]
p_{SFS}.....sensor full scale pressure [Torr]
L_{min} .....min. controllable conductance [l/s]

Do not use a different gasflow than recommended for autolearning otherwise pressure control performance may be insufficient.

valve size	DN63	DN100	DN160	DN200	DN250	DN320	DN400
min. controllable conductance	0.6 l/s	1 l/s	1.6 l/s	2 l/s	2.5 l/s	3.2 l/s	4 l/s

Figure A.2 PM5 Configuration (Setup Sequence) [61].

In figure A.3 the menu structure of the PTD is depicted.

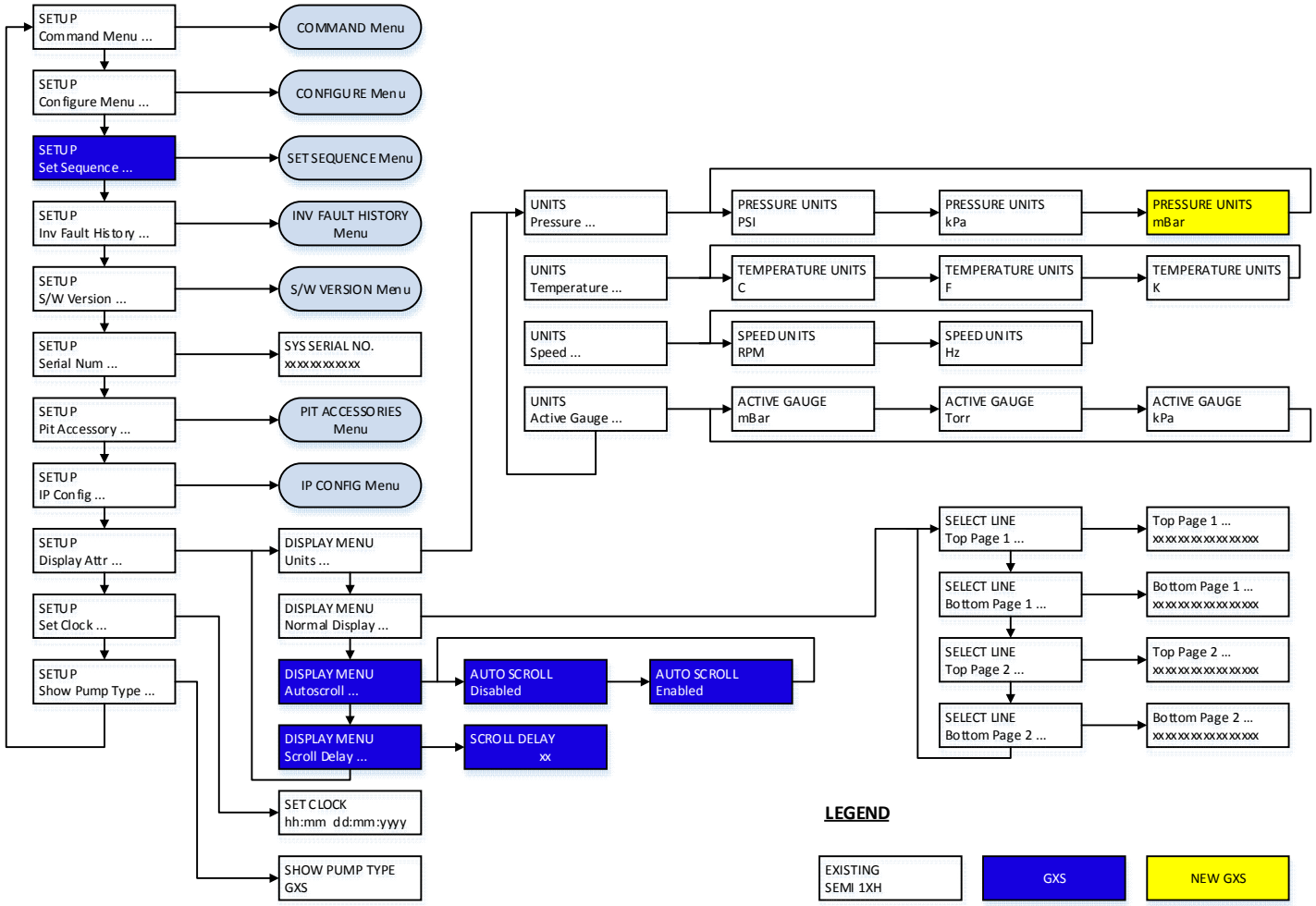

Figure A.3 PTD Menu Structure [52].

Figure A.4 shows the menu structure of the TIC.

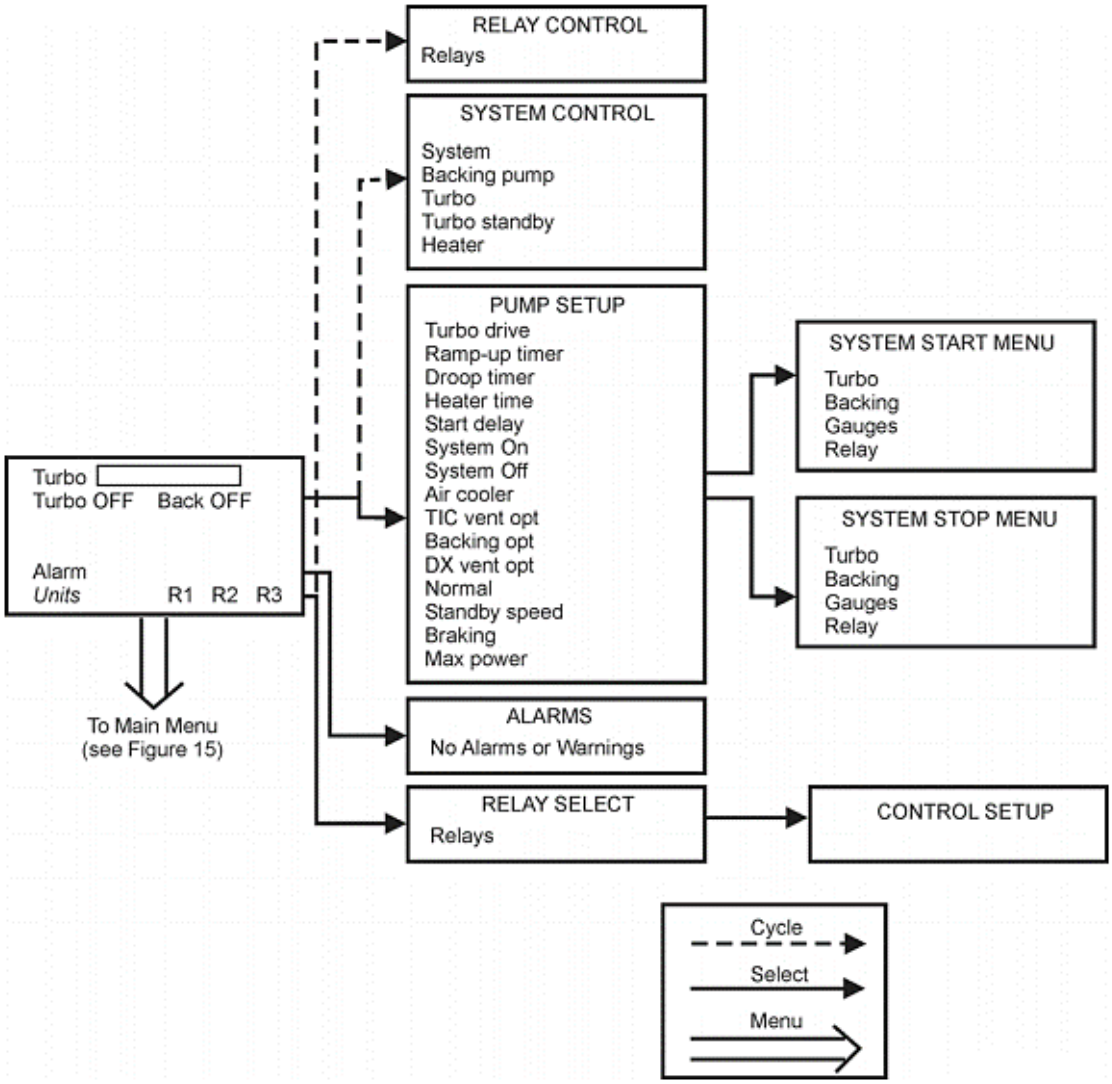

Figure A.4 Menu Structure of the TIC [54]

The figure below presents the main menus of the RPDG.

ARC DETECT	RPG MENU	SEQUENCE	TARGET LIFE	SETUP/MISC
Hard Arc Count *	Pulse Frequency	Sequence Number	On/Off	Tap Setting****
Mechanical Arc Count *****	Pulse Width	Level Type	Target Number	Arc USER Base Term
Max Hard Arcs	Mechanical Arc Detect ON/OFF	Number of Points	Target Life Remaining	Arc USER Proportional Term
Arc Type Max	Pulse Mode ON/OFF	Next Sequence		Ramp Time
Arc-Reset Delay	Synch Type	Set #0, Set point		On/Off Ctrl HOST/USER
		Set #0, Time/Joules		
Resistance Limit Setpoint	Pulse Mode Overrider	Set #1, Set point		Set point Ctrl HOST/USER
		Set #1, Time/Joules		
Resistance Limit Arcs ******	Mechanical Arc Handling Type	•		Reg Mode Ctrl HOST/USER
		•		
		•		Ramp Time Ctrl HOST/USER
		Set #9, Set point		
		Set #9, Time/Joules		Target No. Ctrl HOST/USER
				Pulse Mode Control HOST/USER
				RS-422 Address**
				Joules Resolution***
				Sputter Yield Voltage Low Limit
				Set Point Deviation Time
				Set Point Deviation Percentage
				Software Version***
				Software Checksum***
				DSP Software Version***
				DSP Software Checksum***

* *Reading only. Number of Hard Arcs that have occurred during present run.*

** *Reading only. If DIP switches 1 to 4 are OFF, the RS-422 address set through the serial port will be displayed.*

*** *Reading only.*

**** *Tap setting should never be changed from 500 V, for a normal RPDG Unit.*

***** *Reading only. Number of Mechanical Arcs that have occurred during the present run.*

****** *Reading only. Number of Resistance Limit Trip Arcs that have occurred during the present run.*

Figure A.5 Main Menus of the RPDG [57]

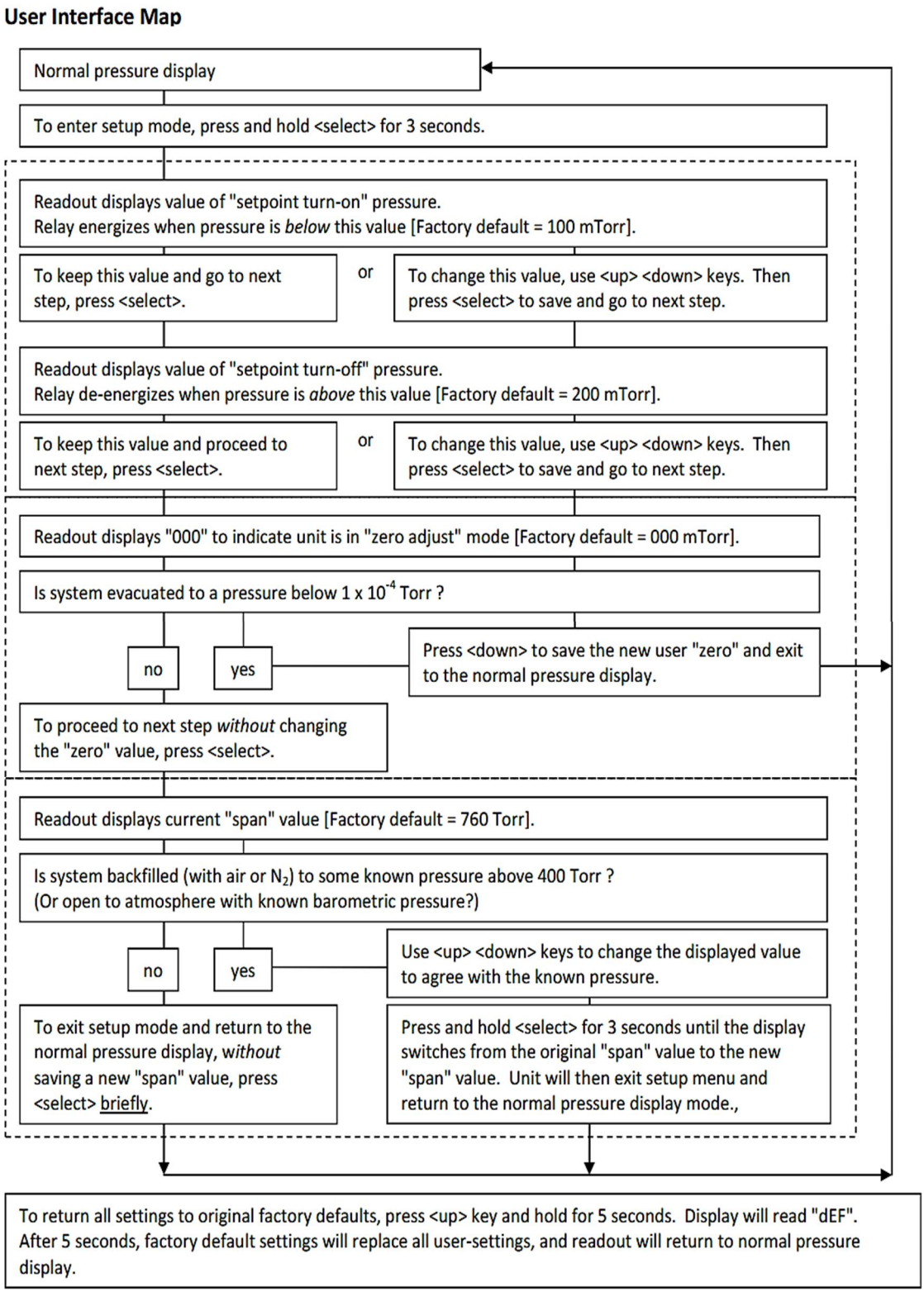

Figure A.6 CG User Interface Map [59]

APPENDIX B

PROPTERTIES OF TRANSPARENT CONDUCTING OXIDES

Table B.1 List of Important Properties of Typical TCOs [6]

Compound	Structure type	Cell dimensions			Resistivity	Band-gap	Dielectric constant	Refractive index
		a [Å]	b [Å]	c [Å]	[Ω cm]	[eV]		
SnO_2	Rutile	4.7371	---	3.1861	10^{-2}–10^{-4}	3.7 – 4.6	12 (E ‖ a) 9.4(E ‖ c)	1.8 – 2.2
In_2O_3	C-rare earth	10.117	---	---	10^{-2}–10^{-4}	3.5 – 3.75	8.9	2.0 – 2-1
ITO	C-rare	10.117-10.31	---	---	10^{-3}–10^{-4}	3.5 – 4.6	---	1.8 – 2.1
Cd_2SnO_4	Sr_2PbO_4	5.5684	9.8871	3.1933	10^{-3}–10^{-4}	2.7 – 3.0	---	2.05 – 2.1
ZnO	Wurtzite	3.2426	---	5.1948	10^{-1}–10^{-4}	3.1 – 3.6	---	1.85 – 1.9

APPENDIX C

PRESSURE CONVERSION TABLES

Table C.1 Pressure Conversion Table

Pressure Unit	atm	bar	Torr	Pa	psi
atm	1	1.01325	760	1.01325×10^{5}	14.69595
bar	0.98692	1	750.06	10^{5}	14.50377
Torr	1.359551×10^{-3}	1.333244×10^{-3}	1 (= 1 mm Hg)	133.3224	1.933678×10^{2}
Pa	9.8692×10^{-6}	10^{-5}	$7.5006\ 10^{-3}$	1	1.450377×10^{-4}
psi	6.8046×10^{-2}	6.8948×10^{3}	51.71493	6.8948×10^{3}	1

Table C.2 Leak Rate Conversion Table

Pressure Unit	mbar l/s	sccm	Torr l/s	Pa l/s
mbar l/s	1	59.234	0.75	100
sccm	1.69×10^{-2}	1	1.27×10^{-2}	1.69
Torr l/s	1.33	60	1	133
Pa l/s	10^{-2}	5.93×10^{-1}	7.5×10^{-3}	1

REFERENCES

[1] Fontaine, B., Orlandi, S. "Global Market Outlook for Photovoltaics 2014-2018". European Photovoltaic Industry Association. 2014. Web.

[2] "Research Cell Efficiency Records" *National Center for Photovoltaics at NREL.* (2014). Web. 31 Mar. 2015.

[3] Eckertová, L. *Physics of Thin Films*. New York: Plenum, 1986. Print.

[4] Delahoy, A.E. and S. Guo. "Transparent Conductive Oxides for Photovoltaics". Chapter 17 in *Handbook of Photovoltaic Science and Engineering*, 2nd Edition, Edited by Luque, A. and Hegedus, S. Wiley, Chichester (March 2011). 716-796. Print.

[5] Bunshah, R. F. *Handbook of Deposition Technologies for Films and Coatings: Science, Technology, and Applications*. Park Ridge, NJ: Noyes Publications, 1994. Print.

[6] Hartnagel, H. L., A. L. Dawar, A. K. Jain, and C. Jagadish. *Semiconducting Transparent Thin Films*. Bristol: Institute of Physics Pub., 1995. Print.

[7] "Chapter 3 - Experimental." *CVD Diamond Film Growth - Chapter 3: Experimental.* University of Bristol, School of Chemistry, 9 Feb. 2015. Web. 05 Mar. 2015.

[8] Chen, E. "Thin Film Deposition." *Applied Physics* 298r (2004): n. pag. Thin Film Deposition. Harvard University, 4 Dec. 2004. Web. 5 Mar. 2015.

[9] Kelly, P. J., and R. D. Arnell. "Magnetron Sputtering: A Review of Recent Developments and Applications." Vacuum 56.3 (2000): 159-72. Web.

[10] Liebermann, M. A. *Principles of Plasma Discharges and Materials Processing.* S.l.: Wiley VCH, 2005. Web.

[11] Maissel, L. I., and M. H. Francombe. *An Introduction to Thin Films.* New York: Gordon and Breach Science, 1973. Print.

[12] Chapman, B. N. *Glow Discharge Processes: Sputtering and Plasma Etching.* New York: Wiley, 1980. Print.

[13] "Thin Films." *Sciencenet* (n.d.): n. pag. Web. 14 Feb. 2015. <http://image.sciencenet.cn/olddata/kexue.com.cn/bbs/upload/8181Thin_Films1.pdf>.

[14] Koch, H., L. J. Friedrich, and V. Hinkel. "Hollow Cathode Discharge Sputtering Device for Uniform Large Area Thin Film Deposition." *Journal of Vacuum Science & Technology A: Vacuum, Surfaces, and Films* 9.4 (1991): 2374. Web.

[15] Leaver, K. D., and B. N. Chapman. *Thin Films*. London: Wykeham Publications, 1971. Print.

[16] Boltz, J. *Sputtered tin oxide and titanium oxide thin films as alternative transparent conductive oxides.* Dissertation. Aachen: RWTH Aachen University, 2011. Web.

[17] Srakinos, K. *Process-property relations in reactively sputtered transition metal compounds*. Dissertation. Aachen: RWTH Aachen University, 2007. Web.

[18] Delahoy, A. E., S. Y. Guo, C. Paduraru, and A. Belkind. "Reactive-environment, Hollow Cathode Sputtering: Basic Characteristics and Application to Al_2O_3, Doped ZnO, and In_2O_3:Mo." *Journal of Vacuum Science & Technology A: Vacuum, Surfaces, and Films* 22.4 (2004): 1697. Web.

[19] Miccoli, I., R. Spampinato, and F. Marzo. "DC-magnetron Sputtering of ZnO:Al Films on (00.1)Al2O3 Substrates from Slip-casting Sintered Ceramic Targets." *Applied Surface Science* 313 (2014): 418-23. Web.

[20] Garamoon, A. A., A. Samir, F. F. Elakshar, and E. F. Kotp. "Electrical Characteristics of a DC Glow Discharge." *Plasma Sources Science and Technology* 12.3 (2003): 417-20. Web.

[21] Behrisch, R., and K. Wittmaack. *Sputtering by Particle Bombardment III: Characteristics of Sputtered Particles, Technical Applications*. Berlin: Springer-Verlag, 1991. Print.

[22] Mattox, D. M. *Handbook of Physical Vapor Deposition (PVD) Processing*. Oxford, UK: William Andrew, 2010. Print.

[23] Rossnagel, S. M., J. J. Cuomo, and W. D. Westwood. *Handbook of Plasma Processing Technology: Fundamentals, Etching, Deposition, and Surface Interactions*. Park Ridge, NJ, U.S.A.: Noyes Publications, 1990. Print.

[24] Guo, S. Y., W. N. Shafarman, and A. E. Delahoy. "TiN and TiO2:Nb Thin Film Preparation Using Hollow Cathode Sputtering with Application to Solar Cells." *Journal of Vacuum Science & Technology A: Vacuum, Surfaces, and Films* 24.4 (2006): 1524. Web.

[25] Delahoy, A. E. "Reactive-Environment Hollow Cathode Sputtering: Compound Film Production, and Application to Thin Film Photovoltaics." *Photovoltaic Energy Conversion Conference Record of the 2006 IEEE 4th World Conference* (2006): 327-32. Web.

[26] Maissel, L. I., and Reinhard Glang. *Handbook of Thin Film Technology*. New York: McGraw-Hill, 1970. Print.

[27] Baratto, C., A. Ponzoni, M. Ferroni, L. Borgese, E. Bontempi, and G. Sberveglieri. "Sputtering Deposition of Amorphous Cadmium Stannate as Transparent Conducting Oxide." *Thin Solid Films* 520.7 (2012): 2739-744. Web.

[28] Coutts, T. J., Perkins, J.D., Ginley, D.S. “Transparent Conducting Oxides: Status and Opportunities in Basic Research” *National Renewable Energy Laboratory* (1999). Web.

[29] Alnajjar, A. A. "ZnO:Al Grown by Sputtering from Two Different Target Sources: A Comparison Study." *Advances in Condensed Matter Physics* 2012 (2012): 1-8. Web.

[30] Minami, T. "Transparent Conducting Oxide Semiconductors for Transparent Electrodes." *Semiconductor Science and Technology* 20.4 (2005): S35-44. Web.

[31] Rahmane, S., and M. S. Aida. "Effect of Thickness Variation on Properties of ZnO:Al Thin Films Grown by RF Magnetron Sputtiering Deposition." *Superlattices and Microstructures* 79 (2015): 148-55. Web.

[32] Morkoç, H., and Ü. Özgür. *Zinc Oxide: Fundamentals, Materials and Device Technology*. Weinheim: Wiley-VCH, 2009. Print.

[33] "Zinc Oxide." *Wikipedia*. Wikimedia Foundation, 06 Feb. 2015. Web. 08 Feb. 2015.

[34] Janotti, A., and C. G Van De Walle. "Fundamentals of Zinc Oxide as a Semiconductor." Reports on Progress in Physics 72.12 (2009): 126501. Web.

[35] Janotti, A., and C. G. Van De Walle. "New Insights into the Role of Native Point Defects in ZnO." *Journal of Crystal Growth* 287.1 (2006): 58-65. Web.

[36] Look, D. C., and D. C. Reynolds. "Electrical Properties of Bulk ZnO." *Solid State Communications* 105.6 (1998): 399-401. Web.

[37] Gsiea, A. M. "Native Point Defects in ZnO." *International Journal of Mathematical, Computational, Physical and Quantum Engineering* 8.1 (2014): 127-32. Web.

[38] Delahoy, A. E., and M. Cherny. "Deposition Schemes for Low Cost Transparent Conductors for Photovoltaics." *MRS Proceedings* 426 (1996): 467-77. Web.

[39] Tsuji, N., H. Komiyama, and K. Tanaka. "Growth Mechanism of ZnO Film by Reactive Sputtering Method –Significance of Thermodynamics in a Plasma System– ." *Japanese Journal of Applied Physics* 29.Part 1, No. 5 (1990): 835-41. Web.

[40] Alkahlout, A., N. Al Dahoudi, I. Grobelsek, M. Jilavi, and P. W. De Oliveira. "Synthesis and Characterization of Aluminum Doped Zinc Oxide Nanostructures via Hydrothermal Route." *Journal of Materials* (2014): 1-8. Web.

[41] Delahoy, A. E., L. Chen, M. Akhtar, B. Sang, and Sheyu Guo. "New Technologies for CIGS Photovoltaics." *Solar Energy* 77.6 (2004): 785-93. Web.

[42] Delahoy, A. E., and S. Y. Guo. "Transparent and Semitransparent Conducting Film Deposition by Reactive Environment, Hollow Cathode Sputtering." *Journal of Vacuum Science and Technology A* 23.4 (2005): 1215-220. Web.

[43] Garamoon, A. A., A. Samir, F. F. Elakshar, and E. F. Kotp. "Electrical Characteristics of a DC Glow Discharge." *Plasma Sources Science and Technology* 12.3 (2003): 417-20. Web.

[44] Winter, M. "Tin: Tin Dioxide" *Web Elements Periodic Table*. University of Sheffield and Web Elements Ldt, 2015. Web. 07 Mar. 2015.

[45] Batzill, M., and U. Diebold. "The Surface and Materials Science of Tin Oxide." *Progress in Surface Science* 79.2-4 (2005): 47-154. Web.

[46] Zhao, S., Y. Zhou, S. Wang, K. Zhao, and P. Han. "Effect of Ambient Oxygen Pressure on Structural, Optical and Electrical Properties of SnO2 Thin Films." *Rare Metals* 25.6 (2006): 693-96. Web.

[47] Mamazza, R., D. L. Morel, and C. S. Ferekides. "Transparent Conducting Oxide Thin Films of Cd_2SnO_4 Prepared by RF Magnetron Co-sputtering of the Constituent Binary Oxides." *Thin Solid Films* 484.1-2 (2005): 26-33. Web.

[48] Wang, W.l., K.j. Liao, C.z. Cai, G.b. Liu, and Y. Ma. "Influence of Annealing Treatment on the Optical Properties and Structure of Cd_2SnO_4 Thin Films." *Surface and Coatings Technology* 167.2-3 (2003): 284-87. Web.

[49] Meysing, D.m., J.m. Burst, W.l. Rance, M.o. Reese, T.m. Barnes, T.a. Gessert, and C.a. Wolden. "The Influence of Cadmium Sulfide and Contact Annealing Configuration on the Properties of High-performance Cadmium Stannate." *Solar Energy Materials and Solar Cells* 117 (2013): 300-05. Web.

[50] Wohlmuth, W., and I. Adesida. "Properties of R.F. Magnetron Sputtered Cadmium–tin–oxide and Indium–tin–oxide Thin Films." *Thin Solid Films* 479.1-2 (2005): 223-31. Web.

[51] "Global Vacuum Product Guide". *Kurt J. Lesker Company.* 9th Edition (2014). Print.

[52] "GXS Dry Pumping System - Instruction Manual". *Edwards Vacuum* M588-00-880 Issue D Original (2012). Print.

[53] "Large Pumps and Pumping Systems." *Edwards Vacuum*. Web. 26 Mar. 2015.

[54] "nEXT Turbomolecular Pumps: nEXT240, nEXT 300 and nEXT 400 – Instruction Manual". *Edwards Vacuum* B800-00-880 Issue D Original (2013). Print.

[55] "XDS Dry Pump – Instruction Manual". *Edwards Vacuum* A726-01-880 Issue M Original (2010). Print.

[56] "User's Guide Class 5 SmartMotor Technology with Combitronic". *Moog Animatics* Rev. A SC80100000-001 (2013). Web.

[57] "RPDG-50/RPDG-100/RPDG-200 Operation Manual". *MKS Instruments* 9311-002 (2012). Print.

[58] “Brooks® GF40/GF80 Series MultiFloTM Capable Digital Thermal Mass Flow Devices – Installation and Operation Manual”. *Brooks Instrument* 541B161AAG (2011). Print.

[59] “Vacuum Gauge with Integrated Controller and Display – 275i Series Convection Gauge Module”. *Kurt J. Lesker Company* p/n 000493-107 (2013). Print.

[60] “DPi8 Temperature & Process Monitor CNi8-AL, CNi8D-AL Temperature & Process Limit Alarm: Quick Start Guide”. *Omega* MQS3446/0307 (2001). Print.

[61] “Adaptive Pressure Controller PM-4 & 5 for Gate Valve Control System: Installation, Operating, and Maintenance Instructions”. *VAT Vakuumventile* 225590EE (2005). Print.

[62] Muhl, M., and A. Pérez. "The Use of Hollow Cathodes in Deposition Processes: A Critical Review." *Thin Solid Films* 579 (2015): 174-98. Web.

[63] Chambers, A. *Modern Vacuum Physics*. Boca Raton: Chapman & Hall/CRC, 2005. Print.

[64] “Fundamentals of Vacuum Technology”. *Aerlikon Leybold Vacuum* 00.200.02 (2007). Web.